Geochemical Modeling Study of Shale–Brine–CO_2 Interaction

by

Ozan Turkes

A thesis submitted to the Graduate Faculty of
Auburn University
in partial fulfillment of the
requirements for the Degree of
Master of Science

Auburn, Alabama
May 1, 2021

Keywords: carbon sequestration, water-rock-CO_2 interaction, trace element mobilization

Approved by

Dr. Ming-Kuo Lee, Chair, Professor, Department of Geosciences
Dr. Ashraf Uddin, Professor, Department of Geosciences
Dr. Lauren E. Beckingham, Assistant Professor, Department of Civil Engineering

Abstract

A promising large-scale mitigation option for reducing CO_2 footprint is Geological Carbon Sequestration (GCS) in depleted oil and gas reservoirs and deep saline aquifers. This study investigated the interaction between CO_2 and shale caprocks during the process of geologic CO_2 storage. CO_2 is less dense than formation waters and thus its buoyancy provides a driving force for it to react with overlying caprocks and potentially escape back to the surface via fractures or abandoned wells. The trace element-rich shale caprocks could potentially pose a threat to overlying groundwater aquifers. To understand the potential risk, geochemical models were built after analyzing the shale samples from the Black Warrior Basin (BWB) by using XRD, XRF, Electron Microprobe, and ICP-MS.

XRD, XRF, Electron Microprobe, and ICP-MS results showed that Conasauga Shale Shelby County sample is rich in carbonate minerals while Neal (Floyd) Shale Pickens County sample is rich in clay, silicate, and sulfide minerals. Conasauga Shale Claire County, Chattanooga Shale Greene County, and Devonian Shale Hale County samples contained various amounts of carbonate, silicate, clay, and sulfide minerals. Shales with significant silicate, clay, and sulfide minerals were relatively enriched in Al, Si, K, Na, V, Cu, Pb, Ni, Cr, Se, Zn, As, Be, and Co, whereas carbonate-bearing shales were enriched in Ca, Mg, and Sr.

Geochemist's Workbench was used to model potential mineral precipitation/dissolution and trace element mobilization via desorption and ion-exchange reactions during CO_2 injection. The models indicate that carbonate mineral such as calcite readily dissolve, whereas silicates and clay minerals are only of secondary importance in dissolution. Calcite dissolution is the dominant reaction at the beginning of CO_2 injection. The overall shale-brine-CO_2 interaction would result in an increase in shale porosity. A higher calcite content decreased the dissolution of albite, k-

feldspar, chlorite, illite, and the subsequent precipitation of dawsonite and kaolinite. A lower calcite content resulted in a lower pH at high CO_2 fugacity. Geochemical modeling also shows that the pH drop results in the desorption of trace elements (e.g., Zn^{2+}, Ni^{2+}, and Co^{2+}) from the surface of $Fe(OH)_3$. Most of the desorption process occurs at low CO_2 fugacity of 0-100 bar. Numerical models show that trace elements may be mobilized via ion-exchange reactions with clay minerals (illite) present in shales. The increasing calcite dissolution and Ca^{2+} concentration resulted in significantly more trace element mobilization due to ionic competition on exchanging sites. Geochemical models also revealed different trace element mobilization behaviors. Sr^{2+} and Co^{2+} were significantly influenced by ion-exchange reactions and increased ion concentration in the fluid, whereas Ni^{2+} and Zn^{2+} were mainly affected by the sorption processes and change in pH.

Acknowledgments

I have received a great deal of support and assistance throughout the writing of this thesis. First and foremost I would like to thank the chair of my committee, Dr. Ming-Kuo Lee, for his support throughout this research. Dr. Lee's insightful feedback and guidance pushed me to sharpen my thinking and brought my work to a higher level. I could not have done this without him. I would also like to thank my committee members Dr. Ashraf Uddin and Dr. Lauren Beckingham for their insights and contributions. Their support during this process was extremely beneficial.

I would like to thank Dr. Mehmet Zeki Billor for his support with XRD, XRF, and ICP-MS analyses. He is truly a master of his craft and his assistance gave me the assurance that I needed to confidently present my results. I would also like to thank Dr. Willis Hames for his support with electron microprobe analysis.

I deeply thank my parents, Mustafa and Cemile Turkes, for their unconditional trust, encouragement, and support. Thank you for pushing me academically from a young age. I would also like to thank my fellow graduate students and my friends back in Turkey for their continuous, invaluable support. I would never have gotten to where I am today without my family and friends. Thank you all so much.

Table of Content

List of Figures

List of Tables

Introduction

One of the greatest challenges humanity encounters in the 21st century is climate change. It is a well-established fact that greenhouse gas (GHG) emissions have increased significantly over the last 150 years (EPA et al., 2014), within which, 75 percent is CO_2. The significant increase in CO_2 concentration in the atmosphere (from 278.0 ± 0.1 to 405 ± 0.1 parts per million in the past 270 years) has caused global warming (Abernethy et al., 2018). Fossil fuel combustion, land-use changes, and cement production are significant sources of increased CO_2 (IPCC, 2005, 2014; Sharma, 2011; Boden et al., 2017; Abernethy et al., 2018). At the same time, fossil fuels like coal, petroleum, and natural gas are significant sources (over 85%) of energy in the world, and they will likely dominate energy consumption at least toward the middle of the 21st century (Koide et al., 1995; Jean-Baptiste and Ducroux, 2003; IPCC, 2005; Lemieux, 2011). Furthermore, countries in Asia, Africa, and the Middle East are expected to increase CO_2 emissions (Zhou et al., 2016; EIA, 2017). Given these facts, it is appropriate to assume that Earth's climate and the environment will be affected by the significant increase in GHG emissions.

Geological carbon sequestration (GCS) can play a key role in addressing the issue of climate change. CO_2 produced from point sources can be stored in depleted oil and gas reservoirs, deep saline aquifers, and unmineable coal beds (IPCC, 2005). Deep saline aquifers (depth >800 m) located near point sources provide large storage capacity (Table 1) and long-term isolation (~ 100 years) capacity for GCS (Yamasaki, 2003; IPCC, 2005; Michael et al., 2010; Lee et al., 2016; Bui et al., 2018; Sharifzadeh et al., 2019). Effective underground geological storage is characterized by thick, porous, and permeable geologic formations (reservoirs) sealed by caprocks with low porosity and permeability (Bachu, 2000; IPCC, 2005). One major issue in GCS research concerns the CO_2 leakage and induced geochemical reactions. There is a risk of potential CO_2 and

brine leakage through faults/fractures in caprocks, or poorly cemented, abandoned boreholes (Shukla et al., 2010; Song and Zhang, 2013; Yang et al., 2018). The migration of CO_2 and brine has the potential to promote transportation and mobilization of trace elements from either CO_2 reservoirs or leakage pathways (Armitage et al., 2011). It is essential to employ numerical modeling to better understand the mechanisms of CO_2-induced geochemical reactions and the potential risks for the potable groundwater aquifers. Quantifying shale-brine-CO_2 interactions requires a modeling capability that explicitly accounts for thermodynamically and kinetically controlled geochemical reactions among migrating CO_2 and minerals in hosting geologic formation.

This thesis investigates the potential shale-brine-CO_2 interactions and trace element mobilization mechanisms in shale caprocks with various mineral contents. XRD, XRF, EMP, and ICP-MS were used to analyze the mineralogic and elemental composition of shale samples from the Black Warrior Basin (BWB). Next, Geochemist's Workbench (GWB) was used to model thermodynamically and kinetically controlled geochemical reactions of mineral precipitation and dissolution, adsorption and desorption, and ion exchange.

Table 1 Storage Capacity for various geological storage options (IPCC, 2005).

Reservoir Type	**Storage Capacity (Lower – Upper Estimate $GtCO_2$)**
Oil and Gas Fields	675 – 900
Unminable Coal Seams	15 – 200
Deep Saline Aquifers	1,000 – 10,000

Background

Overview of Geological Carbon Sequestration

Anthropogenic CO_2 emissions from stationary point sources can be reduced by the widespread application of GCS (Bachu, 2000; Lackner, 2003; IPCC, 2005; Orr, 2009; Heuberger et al., 2016; Abanades et al., 2017). The main goal of GCS is to separate CO_2 from an anthropogenic point source (i.e., like a coal-fired power plant) by injecting it into a subsurface geologic storage where it will remain separated from the atmosphere for more than 1000 years (IPCC, 2005).

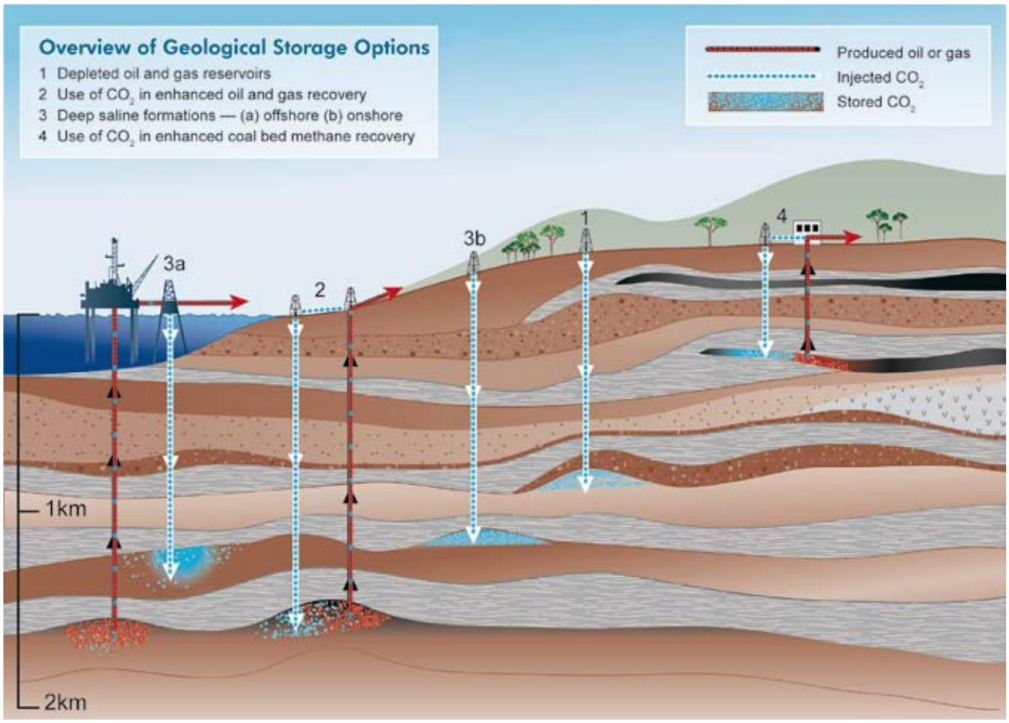

Figure 1 Overview of Geological Storage Options (IPCC, 2005)

Suitable storage formations should be porous and permeable formations covered by low permeability formations (seals or caprocks) such as shales or evaporites. Therefore, depleted oil and gas reservoirs, deep saline aquifers, and unmineable coal seams are considered appropriate

CO_2 storage formations (Figure 1) (Koide et al., 1993; Perkins et al., 1997; Bachu and Adams, 2003; IPCC, 2005; Benson and Cole, 2008).

The effectiveness of GCS operations depends on trapping mechanisms. A series of trapping mechanisms dominate at different time intervals (Figure 2). Structural and stratigraphic trapping is dominant at the beginning and holds the CO_2 that moves towards the earth's surface by its buoyancy. It is followed by residual and solubility trapping, where capillary forces within the individual pores of a permeable aquifer trap CO_2 and dissolve it in brine (Niu et al., 2014). Brine chemistry changes as the dissolving CO_2 increases the acidity. Finally, the safest trapping mechanism, mineral trapping, dominates and converts CO_2 into minerals. Mineral trapping is the most permanent form of geological storage (IPCC, 2005). Moreover, substantial geochemical reactions may be induced by the dissolution of CO_2 into the formation water, lowering the fluid pH:

$$CO_{2(g)} + H_2O \rightarrow H_2CO_3 \rightarrow HCO_3^- + H^+ \rightarrow CO_3^{2-} + 2H^+ \quad (1),$$

which in turn affects mineral solubility and mobilization of trace elements (Lee and Saunders, 2003).

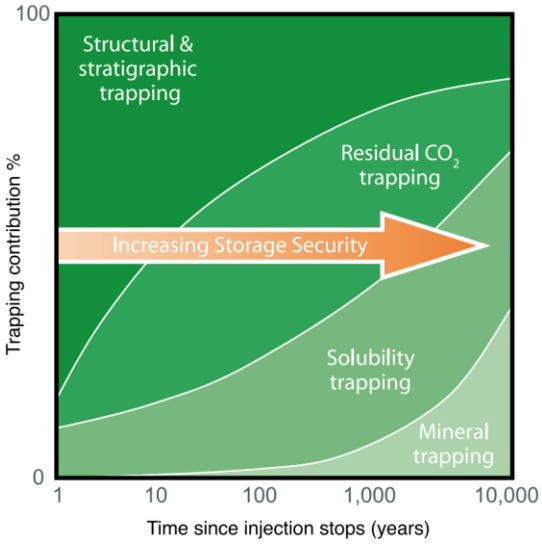

Figure 2 CO_2 Trapping Mechanisms and Storage Safety (IPCC, 2005)

Brine and CO_2 Leakage from Geological Carbon Storage

Brine and CO_2 leakage through caprocks have the potential to degrade water quality during GCS operations (Keating et al., 2010; Harvey et al., 2013; Trautz et al., 2013; Xiao et al., 2016). Elevated pressure due to the CO_2 injection raises concerns over the pressure-driven flow of CO_2-charged brine through old oil & gas wells, undetected faults, and fractures (Birkholzer et al., 2009; Duguid and Scherer, 2010; Strandli and Benson, 2013; Guyant et al., 2016). Several studies showed that the elevated trace element concentrations and undesired geochemical reactions might contaminate potable groundwater resources (Zheng et al., 2009; Apps et al., 2010; Lu et al., 2010; Little and Jackson, 2011; Qafoku et al., 2017). Geochemical modeling and field experiments have been performed to better understand the interactions between CO_2, minerals in hosting rocks, and potable groundwater. For instance, the modeling study by Zheng and Spycher (2018) studied the fate of trace elements before and after leakage. This study evaluated the interaction between CO_2 and shallow aquifer material containing sand (quartz dominated) and clay facies (kaolinite, illite, or smectite dominated). Much uncertainty still exists about the influence of shale caprocks on the mobilization of trace elements during a leakage.

Caprocks are relatively impermeable sedimentary formations that overlie hydrocarbon reservoirs and deep saline aquifers. Shale is one of the most common caprocks in sedimentary environments. Shale–brine–CO_2 interaction is significant because shale formations contain significant amounts of metal-bearing clay and sulfide minerals that have the potential to degrade water quality. Minerals in shale rocks are usually classified into four categories; siliceous minerals such as quartz, k-feldspar, and albite; clay minerals including kaolinite, illite, chlorite, and montmorillonite; carbonate minerals dominated by calcite and dolomite; and metal-bearing sulfide minerals such as pyrite.

Mineral dissolution is mainly controlled by the solubility of the minerals under varying geochemical conditions. In general, the order of sequence of mineral solubility from high to low is calcite, dolomite, pyrite, plagioclase feldspar, k-feldspar, clay minerals, and quartz (Tang et al., 2016). The solubility of metal-bearing pyrite is strongly dependent on the concentration of oxygen and redox conditions in the environment. Three mechanisms that potentially trigger trace element mobilization are the decrease in pH, reductive dissolution of metal-bearing oxides, and increased competition in sorption between metal cations in the fluid (Wang and Jaffe, 2004; Zheng et al., 2009; Lu et al., 2010). Furthermore, trace element-bearing carbonate, clay, and sulfide minerals all have the potential to release trace elements by dissolution, desorption, or cation exchange reactions. Thus, understanding mineral dissolution, ion exchange, and surface complexation reactions are crucial. Carbonate minerals such as calcite are known to buffer the solution pH. It is also known that mineral solubility and trace element mobility tend to increase in acidic environments (Drever, 1988; Lee and Saunders, 2003). Thus, carbonate minerals and their controls on pH fluctuations are key factors that affect the trace element speciation, precipitation, and sorption in case of an unexpected leakage through shale caprocks.

A crucial question about trace element mobilization in host reservoirs and shale caprocks is about the trace element sources. The first source is the surface of the clay and oxide minerals. The sorbed trace elements can be released into the solution by a notable change in pH (Lee and Saunders, 2003). The second source is metal-bearing brines. The leaked fluid may travel from the deep saline aquifer towards the shallow potable aquifer through leakage pathways. Thus, the trace element content of deep saline aquifers and shale caprocks are significant for the safety of potable aquifers. Furthermore, surface complexation reactions should be studied to fully address geochemical changes in this significant issue.

Trace element contamination is particularly important because of its known adverse effects on human health. For instance, nickel is a known carcinogenic agent (WHO, 2008). Some well-known effects of elevated arsenic concentration are cancers, skin damage, and problems with circulatory systems (WHO, 2008). Barium, which is another trace element found in carbonate-rich shale rocks, may increase blood pressure in the long term (Office of Ground Water and Drinking Water, 2009).

Study Area

The Black Warrior Basin (BWB) is located in northeast Mississippi and northwest Alabama (Figure 3). Coals produced from BWB support two major coal-fired power plants that emit more than 24 million metric tons of CO_2 to the atmosphere annually. The basin hosts diverse coal, coalbed methane, and conventional oil and natural gas resources of Cambrian through the Pennsylvanian age. The structure of this basin is mainly controlled by Ouachita Orogeny to the Southwest, the Appalachian Orogeny to the southeast, and the Nashville Dome to the north (Carroll et al., 1995).

Carbonate and siliciclastic strata which are ranging in age from Cambrian through Pennsylvanian are dominant in the BWB. The Rome and Conasauga Formation consisting of 365 meters of shale and carbonate, cover the basement. Cambrian-age Rome and Conasauga Formations were deposited during Iapetan rifting. Iapetan succession is overlain by a thick section of dolostone, limestone, and sandstone called Knox Group (Thomas, 1972). Knox group was deposited in a passive margin setting. Due to the thrust faults related to Appalachian Orogeny, thick sections of Conasauga Shale can be observed along the margin of BWB (Thomas, 2001; Thomas and Bayona, 2005). There is a northeast-thinning wedge that contains numerous disconformities and heterogeneous assemblage of limestone, shale, and iron-rich sedimentary rock

assigned to the Stones River Group (Middle Ordovician), the Sequatchie Formation (Upper Ordovician), the Red Mountain Formation (Silurian), the Chattanooga Shale (Middle-Upper Devonian), the Fort Pane Chert (Mississippian) and the Tuscumbia Limestone (Lower Mississippian) (Kidd, 1975). The Middle Ordovician to Lower Mississippian rocks were deposited in a passive margin setting and deposited on a southwest-sloping shelf. Chattanooga Shale is wide-spread and dominantly deposited along the southeastern margin of the BWB, where the basin borders the Appalachian thrust belt (Pashin, 2008, 2009; Haynes et al., 2010; Pashin et al., 2010) (Figure 3). Upper Mississippian and Lower Pennsylvanian strata were deposited during Appalachian-Ouachita orogenesis (Thomas, 1974). These strata include the Pride Mountain Formation, the Hartselle Sandstone, the Bangor Limestone, and the Parkwood Formation. In the northeastern part of the basin, Evans Sandstone and Hartselle Sandstone change into a condensed formation of organic-rich shale that is assigned to Neal (Floyd) Shale. During Mississippian, interbedded siliciclastic and carbonate rock types are co-deposited with Neal (Floyd) Shale. Neal (Floyd) Shale was deposited in a continental slope and ocean-floor environment (Cleaves and Broussard, 1980; Pashin, 1993, 1994). The Lewis Sandstone (Pride Mountain Formation), the Hartselle Sandstone, the Carter Sandstone (Parkwood Formation), Gilmer Sandstone (Parkwood Formation), Coats sandstone (Parkwood Formation) are some formations that are producing oil and natural gas. Lewis Sandstone and Carter Sandstone produces most conventional hydrocarbons and the Hartselle Formation is a significant tar sand deposit (Wilson, 1982). The Pottsville Formation is the youngest stratigraphic unit in the Black Warrior Basin and is Early-Middle Pennsylvanian age (Figure 4). The Pottsville Formation contains shale, sandstone, and economic coal seams and its thickness may be up to 1981 meters (Pashin, 2004). The thickness may go as high as 2438 meters (Uddin et al., 2016). Mississippian Lewis Sandstone, Tuscumbia Limestone

are some high-quality reservoirs which are in contact with Mississippian Floyd Shale. Silurian Red Mountain, Ordovician Sequatchie, Stones River, Cambrian-Ordovician Knox are some high-quality reservoirs which are overlain by Devonian Chattanooga Shale. Mississippian rocks below Neal (Floyd) shale have a capacity of 205.1 Mt (P50) for CO_2 injection. Cambrian-Devonian rocks below Chattanooga Shale have a capacity of 1182.9 Mt (P50) for CO_2 injection (Clark et al., 2013). This study focuses on investigating the mineralogy and geochemistry of Neal (Floyd), Conasauga, Chattanooga, and Devonian shale units that may potentially serve as caprocks for CO_2 injection in BWB.

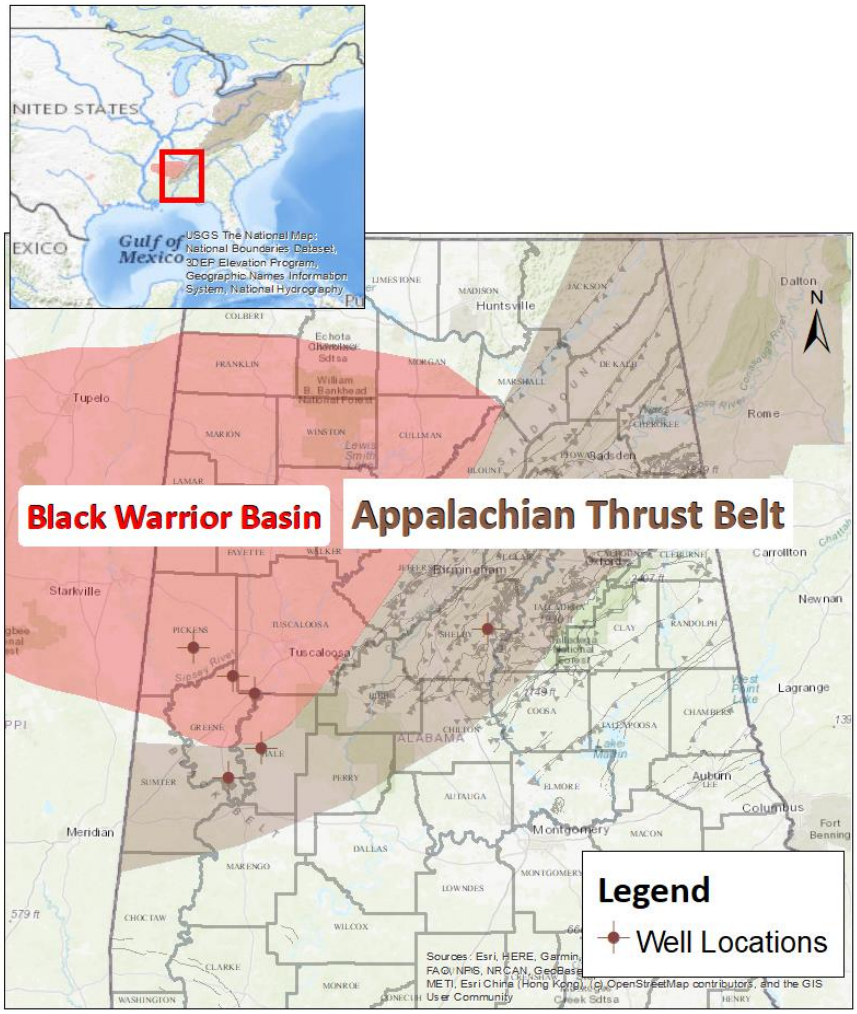

Figure 3 Black Warrior Basin and deep well locations in Alabama and Mississippi (modified from Pashin et al., 2012)

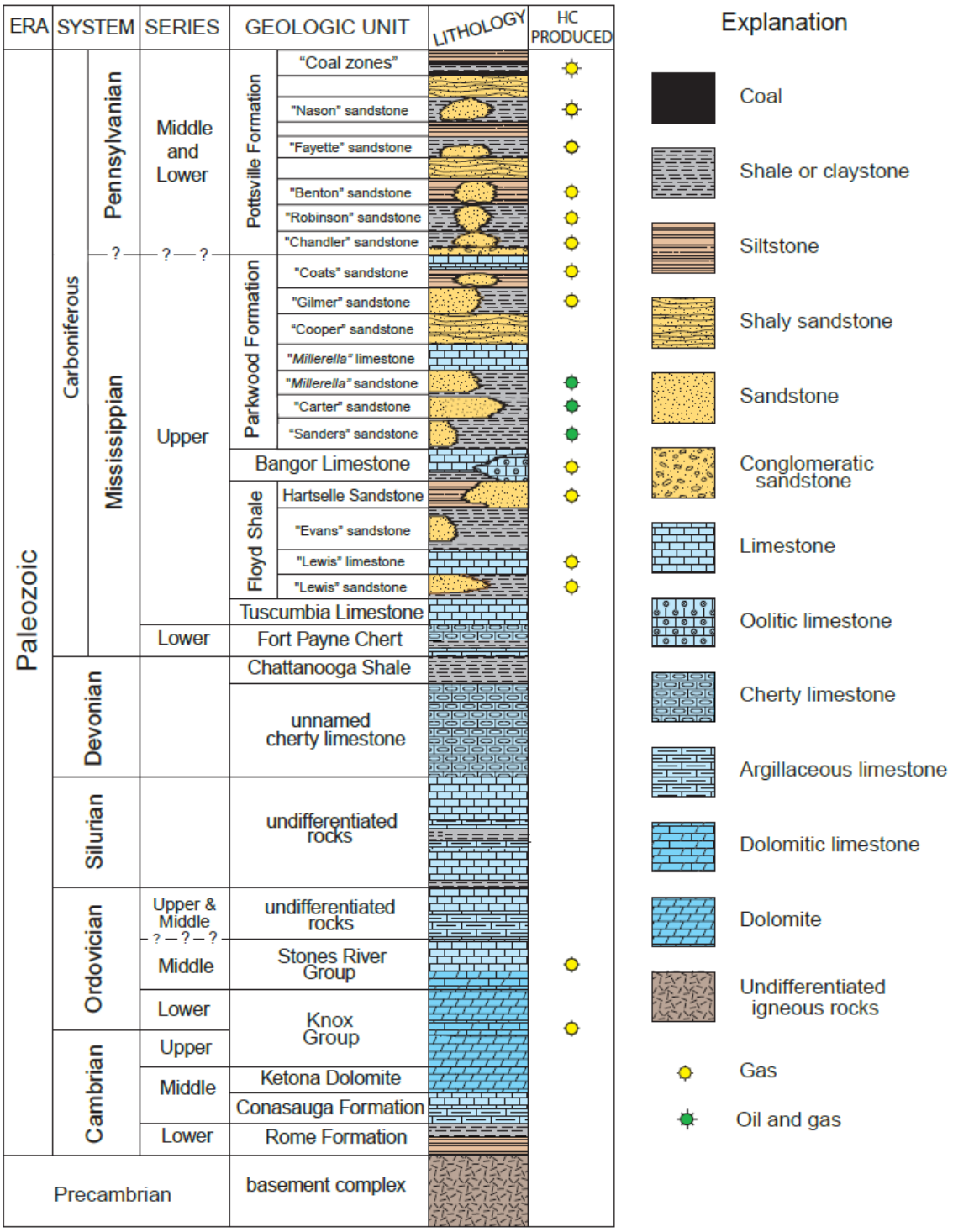

Figure 4 Generalized stratigraphic column for Black Warrior Basin (Hatch and Pawlewicz, 2007)

The Cambrian Conasauga Formation has a thickness of 457 to 914 meters. Due to normal faulting, its thickness may reach 3657 meters at certain localities. Conasauga is composed of

interbedded shale, limestone, and dolostone. Shale is dominant in the lower sections of the formation; limestone and dolostone are dominant in the upper parts (Pashin et al., 2012). In the shale, carbonate minerals dominate the bulk mineralogy with calcite ranging from 8-49% by weight. Quartz varies from 12-20% and clay minerals are between 12-50% (Pashin et al., 2012).

Devonian Chattanooga Formation locally may have high total organic content (TOC), up to 5%. In this shale formation quartz is dominant (between the range of 34-54%). Clay minerals are between 27-42%, and calcite is between 0-14 % (Pashin et al., 2012).

The Mississippian Neal (Floyd) Shale has abundant TOC (6%) and is a probable source of oil and gas (Carroll et al., 1995). The Neal (Floyd) Shale Formation is the equivalent (contemporaneous in origin) to the Barnett Shale of Texas. It is the source rock for conventional reservoirs. Neal (Floyd) Shale Formation also has the potential to be a gas shale play within the Mississippian stratigraphic section of the BWB. In this shale formation, clay minerals are abundant. Quartz varies from 25-47%, and carbonate minerals are negligible (Pashin et al., 2012).

Previous Work on Shale–Brine–CO_2 Interaction and Trace Element Mobilization

The potential risk of CO_2 leakage into shallow groundwater formations overlying CO_2 sequestration sites poses major concerns (Zheng et al., 2009; Harvey et al., 2013; Jones et al., 2015; Qafoku et al., 2017). Many researchers have utilized laboratory experiments (Jung et al., 2013; Shao et al., 2014, 2020; Marcon and Kaszuba, 2015), field tests (Kharaka et al., 2010; Peter et al., 2012; Cahill and Jakobsen, 2013; Trautz et al., 2013), and computer models (Zheng et al., 2013, 2016a, 2016b; Patil, 2016; Xiao et al., 2017; Zheng and Spycher, 2018) to investigate key physical and chemical processes associated with uncertainties and risks of CO_2 leakage. These studies are focused on geological storage formation and shallow groundwater formation.

It is well known that increased CO_2 concentrations in deep formations would reduce pH and trigger geochemical reactions that may result in mineral precipitation/dissolution reactions and trace element mobilization reactions (Apps et al., 2010; Little and Jackson, 2010; Lu et al., 2010b). Laboratory experiments were used to evaluate the changes in the mineral content of geological reservoirs (Table 2). Experiments have been conducted under various reservoir conditions at 75°C (Jung et al., 2013; Shao et al., 2014), 120°C (Aplin et al., 2006), 150°C (Credoz et al., 2009; Kohler et al., 2009), 160°C (Marcon and Kaszuba, 2015), 200°C (Kaszuba et al., 2005), and 250°C (Alemu et al., 2011) to understand how different minerals may react under reduced pH conditions. Reduced pH was found to resulting in substantial carbonate mineral dissolution at various temperatures. Silicate minerals were shown to be reactive only at elevated temperatures. Changes in silicate minerals at lower temperatures were found to be insignificant. Some experiments showed that the decrease in pH, increase in bicarbonate (HCO_3^-) and Ca^{2+} ions concentration lead to precipitation of secondary minerals or reprecipitation of carbonate minerals at the end of the experiment. For example, Alemu et al., (2011) observed that both ankerite ($Ca(Fe,Mg,Mn)(CO_3)_2$) and calcite dissolved first and then subsequently re-precipitated as calcite. The results obtained by laboratory experiments indicated that carbonate mineral content determines the buffer capacity of a geological formation (Assayag et al., 2009; Lu et al., 2010).

Analysis of different rocks by Lu et al., (2010b) showed that the decrease in pH was approximately 1 unit in carbonate systems and around 2 units in siliciclastic systems. This was expected since carbonate mineral dissolution is thermodynamically very favorable and rapid under the presence of protons. Additionally, carbonate mineral dissolution increases alkalinity which increases the intrinsic buffer capacity of the water (Kharaka et al., 2010). Cui et al., (2017) also conducted an experiment using sandstone and carbonate samples. Injection of CO_2 resulted in

dissolution of ankerite and clay minerals and precipitation of plagioclase in the sandstone system. Furthermore, Ca^{2+} and Mg^{2+} ion concentrations were increased in the system. The dissolution of dolomite and re-precipitation of ankerite and calcite were observed at the end of the experiment in the carbonate system.

It is known that adsorption/desorption, cation exchange, and dissolution of carbonate minerals may control the release of trace elements at different reaction stages. These reactions are mainly driven by the change in pH and ionic competition. According to the results of batch experiments, there are two major metal behaviors observed after CO_2 intrusion (Little and Jackson, 2010; Lu et al., 2010; Mickler et al., 2013; Varadharajan et al., 2013). First, a fast initial release, driven by carbonate mineral dissolution and surface processes (e.g., desorption) due to CO_2 intrusion. Second, a slow-release trend, driven by kinetically constrained processes, such as mineral dissolution.

To study the effect of salinity (or ionic strength) on sorption Frye et al., (2012) conducted laboratory experiments by using cadmium (Cd). Laboratory experiments showed that Cd desorption is enhanced by high ionic strength due to increasing ion competition at sorbing sites. They also studied the role of calcite in Cd mobilization. Results show that calcite content as low as 10% can effectively mitigate the effect of pH reduction and Cd release since Cd release is a pH-dependent sorption process. Montes-Hernandez et al., (2013) investigated the effect of CO_2 intrusion on sorption of trace elements onto calcite and goethite (FeO(OH)) by laboratory experiments. Experiments showed that calcite dissolution serves to buffer the pH and prevent Cd(II) and Cu(II) remobilization. In contrast, arsenite As(III) which was strongly adsorbed on goethite, was partially remobilized after the CO_2 intrusion.

Field studies were conducted to investigate CO_2 intrusion into the shallow groundwater aquifer. Controlled CO_2 release tests are performed at certain shallow aquifers (Table 3) to test the responses of aquifer minerals and adsorbed trace elements (Kharaka et al., 2010; Peter et al., 2012; Mickler et al., 2013; Trautz et al., 2013; Yang et al., 2013; Cahill et al., 2014; Humez et al., 2014; Rillard et al., 2014). According to the field tests presented in Table 3, pH drops by 1-3 units would mobilize several trace elements. What is striking in field experiments is the effect of water flux on the pH recovery time. Higher water flux tends to result in a rapid pH recovery in a transport-dominated system. Similar to the results in laboratory studies, the dissolution of proton-consuming minerals such as carbonate minerals, controls the decrease in pH. Kharaka et al., (2010) showed the rapid changes in pH, alkalinity, and electrical conductance (EC) at the ZERT-Bozeman field. The injection of CO_2 increased the concentrations of Ca, Mg, Fe, Mn, BTEX, and other metals. However, except for pH, parameters returned to background levels after CO_2 injection ended. Trautz et al., (2013) conducted similar controlled experiments in Mississippi, USA at a depth of ~50 m. Initially, the concentrations of several elements (Ca, Mg, Na, K, Ba, Sr, Fe, Mn) and alkalinity rapidly increased as the pH dropped from ~8 to ~5. The concentrations of these elements remained below the EPA maximum concentration limits and pH remained relatively low after the injection stopped. All field experiments showed that the water flux is another important control on the element mobilization and groundwater chemistry recovery.

These laboratory and field studies contribute in several ways to our understanding of geochemical reactions in shallow sandstone and carbonate groundwater aquifers and geological reservoirs. This thesis focuses on trace element mobilization from shale caprocks via mineral precipitation/dissolution, adsorption/desorption, and surface complexation reactions, which is less explored by the previous studies.

Table 2 Summary of the experimental studies.

Author	**Temperature**	**Pressure (bar)**	**Time**	**Final pH**
Kaszuba et al., 2005	200 °C	200	32 + 45 days	5.5 – 4.9
Aplin et al., 2006	120 °C	-	-	-
Kohler et al., 2009	150 °C	150	2 Months	-
Credoz et al., 2009	80 – 150 °C	150	30 – 45 – 90 days	4.8
Little and Jackson, 2010	~ 25 °C	10	>300 days	4.4
Lu et al., 2010a	~ 25 °C	-	15 days	~ 4.3
Alemu et al., 2011	80 – 250 °C	110	7 – 35 days	5.36 – 4.21
Rempel et al., 2011	60 °C	65 – 160	5 days	1 – 3 units decrease
Jung et al., 2013	~ 75 °C	100	6 weeks	4.8
Shao et al., 2014	75 °C	101	3 – 30 days	4.4 – 3.3
Marcon and Kaszuba, 2015	160 °C	250	34 – 48 days	1 – 2 units decrease
Shao et al., 2020	50 °C	206	30 days	3.8 – 3.9

Table 3 Controlled CO_2 release test sites, mobilized elements

Test Site	**Mobilized Elements**	**References**
Cranfield, Adams County, Mississippi, USA	B, Ba, Co, Mn, Sr	(Yang et al., 2013)
Brackenridge field site, Austin, Texas, USA	Ba, Sr, U, Zn	(Mickler et al., 2013)
Lodève, France	As, Fe, Mn, Zn	(Rillard et al., 2014)
ZERT field site, Bozeman, Montana, USA (ZERT)	Al, As, Ba, Cd, Cu, Fe, Mn, Pb, Se, Sr	(Kharaka et al., 2010)
CO_2FieldLab site, Norway (CO_2FieldLab)	Al, As, Ba, Li, Mn, Ni, Sr, Zn	(Humez et al., 2014)
Brandenburg, Germany	Al, Ba, Cd, Cu, Mn, Ni, Pb, Zn	(Peter et al., 2012)
Vrøgum, Denmark	Al, Ba, Sr, Zn	(Cahill et al., 2014)
Escatawpa, Mississippi, USA	Ba, Cr, Fe, Mn, Sr	(Trautz et al., 2013)

Table 4 Caprock properties of several carbon storage sites (adapted from Espinoza and Santamarina, 2012).

Field Site	Clay Minerals (weight %)	Other Minerals	Depth (m)	Porosity (%)
Frio, USA	Illite-smectite~45% Illite ~10% Kaolinite 13% Chlorite ~3%	Calcite	1450	8–10
Sleipner, Norway	Mica-Illite ~25% Kaolinite 14–18% Smectite 3–9% Chlorite 1–4%	Calcite 1–3% Siderite 2%	750	35
Krechba, Algeria	Muscovite-illite ~25–50% Chlorite ~20–4% Kaolinite ~8–4%	Siderite ~15–0%	1850	1.8–11.3
Otway, Australia	Kaolinite 44–17% Illite 6–1% Smectite 3–1%	Siderite 35–2%	1980	2.5–7.5
SACROC, USA	Illite-smectite 62%	Calcite 2.5% Dolomite 2% Halite 0.1%	2000	1.3
Rousse, France	Illite 2.2–14.5% Kaolinite 0.3–4.1% Chlorite 0.1–2%	Calcite 30–65% Dolomite 3–63% Siderite 0.1–6.2%	4000	0.5–3
Carnarvon, Australia	Illite-smectite 30–25% Illite 15–20% Kaolinite ~15% Chlorite ~5%	Siderite 1–4%	1100	21
Ketzin, Germany	Illite 42–74% Chlorite 1–3%	Dolomite 4–35% Halite 0–1 %	600	10

Objectives

This research focuses on characterizing three shale caprocks in BWB and their potential interaction with CO_2. The main objectives are to (1) characterize the mineralogy of shale caprocks using X-Ray Diffraction (XRD) analysis, (2) quantify the elemental composition of shale caprocks using X-Ray Fluorescence (XRF), Electron Microprobe (EMP), and Inductively Coupled Plasma Mass Spectrometer (ICP-MS) analysis, (3) quantify total organic carbon (TOC) content in shales using RockEval Pyrolysis, and (4) model shale-brine-CO_2 interactions and trace element mobilization controlled by mineral precipitation/dissolution, adsorption/desorption, and ion exchange reactions.

Methodology

Core Sample Collection

Shale samples were collected from drill cores stored in the Core Warehouse of the Alabama Geological Survey. Representative samples from the Neal (Floyd) Formation, Conasauga Formation, Chattanooga Formation, and Devonian Formation are used for this study. The formation name, county, age, depth, and location (latitude and longitude) of the samples are shown in Table 5.

Table 5 Location, depths, and permit numbers of drill core samples used in this study

Formation	County	Age	Depth (meters)	Permit#	Longitude	Latitude
Neal (Floyd)	Pickens	Mississippian	2026	14289	-88.06002	33.20421
Conasauga	Shelby	Cambrian	4318	3518	-86.52885	33.28967
Conasauga	St. Clair Co.	Cambrian	2298	15720	-86.22214	33.85764
Chattanooga	Greene Co.	Devonian	2572	3800	-87.87437	32.63802
Devonian	Hale Co.	Devonian	3139	3939	-87.70136	32.76762

X-Ray Diffraction (XRD) Analysis

X-ray Diffraction (XRD) is a non-destructive instrumental technique that is used to identify minerals, as well as other crystalline materials. XRD is particularly useful for identifying fine-grained minerals in shales. XRD analysis on shale samples was conducted by using Bruker D2 Phaser X-ray Diffractometer in Auburn University, Department of Geosciences XRD/XRF Laboratory. First, shale samples were crushed and powdered by using the Planetary Ball Mill. Samples were run from 2-theta values of 5-75° with a 0.02 step interval, under 25°C using Cu anode. DIFFRAC.EVA software was used to search and match peaks in the spectrum for silicate, carbonate, sulfide, and clay minerals. XRD also reveals a semi-quantitative makeup of shale

samples, since areas under the peak reflect the amount of each phase present in the sample. XRF is used in conjunction with XRD to find out the bulk chemical composition of samples from BWB shale units.

X-Ray Fluorescence (XRF) Analysis

Handheld XRF provides a fast, non-destructive elemental analysis of geologic materials. It is a mature technique for the elemental analysis of materials. It is rapid, simple, and inexpensive and allows the analysis of a wide range of elements (De Viguerie et al., 2009).

XRF analysis on the same set of shale samples was performed by Tracer IV-SD handheld in the Department of Geosciences, XRD/XRF Laboratory. Samples were polished and fresh surfaces were used to identify the elemental composition. Three different filters with different voltage and amperage were used in each sample to identify different elemental groups. XRF analysis was repeated at three separate locations on each sample. Major (Al, Si, K, Ca, S) and trace elements (Ti, V, Cr, Mn, Fe, Co, Ni, Cu, Zn, As, Sr, Mo, Ba, Pb, Th) were identified. XRF is capable of identifying and quantifying elements down to parts per million (ppm) level. Three reference shale samples were gathered from USGS (SBC-1, SCO-2, SGR-1b) and used to quantify XRF data.

Electron Microprobe (EMP) Analysis

Electron Microprobe (EMP) was used to characterize the mineral surfaces and distribution of trace elements in the samples. Samples were sent to National Petrographic Service, Texas for thin section preparation. Samples were analyzed by JEO-JXA 8600 Superprobe Electron Microscope and Geller System automation in the Department of Geosciences, Auburn University. EMP can analyze small 1-2 micrometer spots. Moreover, these observations can be quantified using necessary reference samples (Reed, 2005). All the samples are coated with carbon to increase

the quality and resolution of the result. The Auburn microprobe facilities are equipped with backscattered electrons (BSE) and scanning electron microscope (SEM) imaging along with energy-dispersive X-ray spectroscopy (EDS) and wavelength-dispersive spectroscopy (WDS) detectors. The software programs used to analyze the samples are Geller System dPict: BSE and Elemental Mapping, Geller System dQuant, and National Institute of Health ImageJ: Image processing.

RockEval Pyrolysis

The samples were sent to Core Labs to measure the richness and maturity of potential source rocks using RockEval Pyrolysis. First pyrolysis temperature was kept isothermally at 300°C for 3 minutes to measure free hydrocarbons (S_1 peak). Next, the temperature was increased from 300°C to 500°C at 25°C/min to measure volatilized heavy hydrocarbon compounds and kerogen (S_2 peak). The CO_2 released from kerogen cracking was measured as an S_3 peak. Thermal maturity (T_{max}) was defined as the temperature at which S_2 reaches its maximum. The residual carbon content of the sample is recorded as S_4. Total organic carbon (TOC) was calculated using S_1 (free hydrocarbons), S_2 (amount of hydrocarbon generated during pyrolysis), and S_4 (residual carbon) peaks.

Microwave-Assisted Acid Digestion and ICP-MS Analysis

After crushing and powdering, rock samples were heated at 105 °C for 3 hours to remove residual water. Next, approximately 0.2 g of samples were weighted (Table 6) and placed into polytetrafluoroethylene (PTFE) microwave vessels. The samples were treated with nitric acid (HNO_3) and hydrochloric acid (HCl) for partial digestion. Milestone ETHOS Easy Microwave Digestor with MAXI-44 vessel was used to digest samples. The temperature has risen to 180 °C in 15 minutes and remained at 180°C for 15 minutes. At the end of the microwave program, vessels

were allowed to cool down for 20 minutes before removing from the microwave system. Next, contents were filtered by DigiFILTER 1.0-micron filter and transferred to 50 mL polypropylene tubes. The filtered solutions were diluted for ICP-MS analysis. An Agilent 7900 Quadrupole ICP-MS system in Auburn University Center for Advanced Science, Innovation and Commerce (CASIC) was used to quantify the elemental composition of digested samples. ICP-MS can measure trace elements at very low detection limits (to ppt levels) as well as major elements (at ppm levels). Indium (In) and Scandium (Sc) were used as internal standards. All the materials used to digest and analyze the samples are demonstrated to be free from interferences under conditions of the analysis by analyzing method blanks and quality control (QC). Furthermore, 10 mg/l complete group calibration standard (VWR International catalog number: BDH82026-108) was used to confirm the results of ICP-MS analysis (Table 7). The analyzed elements are Be, Na, Mg, Al, K, Ca, V, Cr, Mn, Fe, Co, Ni, Cu, Zn, As, Se, Sr, Mo, Ag, Cd, Sb, Ba, Tl, Pb, Th, and U. The USGS Standards SCB-1, SGR-1B, and SCO-2 were analyzed to test the partial digestion performance (Table 8, Table 9). The following formula was used to convert the extract concentration obtained from the instrument in mg/L to mg/kg dry-weight of sample;

$$Sample\ Concentration = \frac{C \times V \times D}{W} \quad (1)$$

C = Concentration in extract (mg/L)

D = Dilution factor

V = Volume of extract, mL

W = Weight of undried sample extracted, g

Table 6 Sample names and weights

Sample Name	Weight (g)
Conasauga Shale St. Claire Co. 7558-7558.8 ft.	0.1972
Devonian Shale Hale Co. 10,354 ft.	0.1980
Chattanooga Shale Greene Co. 8445-8446 ft.	0.2139

Neal (Floyd) Shale Pickens Co. 6566-6568 ft.	0.2053
Conasauga Shale Shelby Co. 14181 ft.	0.2169

Table 7 ICP-MS results of 10 mg/l multielement calibration standard BDH82026-108. There are no Mo and Sb elements in the calibration standard.

Sample	Concentrations (mg/l)
Be	8.41
Na	11.05
Mg	9.36
Al	9.00
K	6.19
Ca	11.94
V	9.34
Cr	9.42
Mn	9.53
Fe	9.78
Co	9.86
Ni	9.81
Cu	9.92
Zn	9.68
As	9.28
Se	11.82
Sr	9.57
Mo	0.01
Ag	6.28
Cd	9.42
Sb	0.00
Ba	9.49
Tl	8.33
Pb	10.05
Th	9.55
U	9.47

Table 8 ICP-MS Results of USGS Shale standards SGR-1b, SCO-2 and SBC-1

Sample Name	**Oxides**	**USGS Certified Results (wt%)**	**ICP-MS Results (wt%)**	**Recovery**
SGR-1b	Al_2O_3	6.52	0.76	12%
SCO-2	Al_2O_3	13.13	5.64	43%
SBC-1	Al_2O_3	21.00	9.60	46%
SGR-1b	CaO	8.38	8.39	100%

SCO-2	CaO	3.94	3.50	89%
SBC-1	CaO	2.95	2.90	98%
SGR-1b	Fe_2O_3	3.03	2.93	97%
SCO-2	Fe_2O_3	4.64	3.87	83%
SBC-1	Fe_2O_3	9.71	8.57	88%
SGR-1b	K_2O	1.66	0.35	21%
SCO-2	K_2O	2.45	0.76	31%
SBC-1	K_2O	3.45	1.43	41%
SGR-1b	MgO	4.44	4.10	92%
SCO-2	MgO	2.85	2.22	78%
SBC-1	MgO	2.60	1.97	76%
SBC-1	MnO	0.15	0.14	91%
SGR-1b	Na_2O	2.99	0.52	17%
SCO-2	Na_2O	1.02	0.12	12%
SBC-1	Na_2O	<0.15	0.08	-

Table 9 ICP-MS Results of USGS Shale standards SGR-1b, SCO-2 and SBC-1

Sample Name	**Elements**	**USGS Certified Results (mg/kg)**	**ICP-MS Results (mg/kg)**	**Recovery**
SGR-1b	As	67.00	64.32	96%
SCO-2	As	11.80	11.29	96%
SBC-1	As	25.70	28.27	110%
SGR-1b	Ba	290.00	254.69	88%
SCO-2	Ba	580.00	206.33	36%
SBC-1	Ba	788.00	511.20	65%
SCO-2	Be	1.75	0.91	52%
SBC-1	Be	3.20	1.85	58%
SGR-1b	Cd	0.90	1.12	125%
SBC-1	Cd	0.40	0.45	112%
SGR-1b	Co	12.00	12.23	102%
SCO-2	Co	10.80	10.95	101%
SBC-1	Co	22.70	21.49	95%
SGR-1b	Cr	30.00	28.56	95%
SCO-2	Cr	68.30	39.92	58%
SBC-1	Cr	109.00	68.08	62%
SGR-1b	Cu	66.00	67.37	102%
SCO-2	Cu	23.50	21.24	90%
SBC-1	Cu	31.00	30.60	99%

SGR-1b	Mn	267.00	245.75	92%
SGR-1b	Mo	35.00	33.90	97%
SCO-2	Mo	1.20	0.89	74%
SBC-1	Mo	2.40	2.10	88%
SGR-1b	Ni	29.00	30.47	105%
SCO-2	Ni	27.80	24.61	89%
SBC-1	Ni	82.80	79.20	96%
SGR-1b	Pb	38.00	47.17	124%
SCO-2	Pb	20.00	17.75	89%
SBC-1	Pb	35.00	33.09	95%
SGR-1b	Sb	3.40	2.75	81%
SCO-2	Sb	0.90	0.40	44%
SBC-1	Sb	1.01	0.56	55%
SGR-1b	Se	3.50	5.01	143%
SGR-1b	Sr	420.00	393.64	94%
SCO-2	Sr	195.00	122.59	63%
SBC-1	Sr	178.00	121.35	68%
SGR-1b	Th	4.80	4.36	91%
SCO-2	Th	9.00	6.88	76%
SBC-1	Th	15.80	10.85	69%
SBC-1	Tl	0.89	0.45	51%
SGR-1b	U	5.40	5.03	93%
SCO-2	U	3.20	1.52	48%
SBC-1	U	5.76	2.60	45%
SGR-1b	V	130.00	122.30	94%
SCO-2	V	117.00	74.12	63%
SBC-1	V	220.00	137.94	63%
SGR-1b	Zn	74.00	76.83	104%
SCO-2	Zn	97.00	87.04	90%
SBC-1	Zn	186.00	182.42	98%

Geochemical Modeling – Description of Geochemist's Workbench Code

Quantifying shale-brine-CO_2 interactions requires a modeling capability that explicitly accounts for multi-component in both aqueous and solid (mineral) phases, including thermodynamically and kinetically controlled geochemical reactions. Geochemist's Workbench (GWB) (Bethke, 2007) was used to simulate the geochemical reactions including mineral

precipitation and dissolution, adsorption and desorption, and cation exchange reactions. The descriptions of the code and modeling approaches are described below.

GWB calculates chemical equilibria and kinetic reactions among mineral solids, aqueous species, and gases, using datasets of thermodynamic equilibrium and kinetic constants from 0 to 300°C. In this study, GWB was used to calculate saturation indices (SI, log Q/K) of minerals, mineral precipitation/dissolution, and speciation reactions. Mineral saturation indices reveal the major precipitation and dissolution reactions in the shale–brine–CO_2 systems. Surface complexation reactions, cation exchange, and mineral reaction kinetics datasets (Table 11Table 12) were created using RES³T - Rossendorf Expert System for Surface and Sorption Thermodynamics database (Brendler et al., 2003). A representative brine from the BWB was used to set up initial conditions (Table 13).

Several reactive path models were built by using GWB to trace how fluid chemistry evolves and which minerals precipitate or dissolve throughout the geochemical process. Metal absorption and desorption were modeled using surface complexation theory (Dzombak and Morel, 1990; Stumm, 1992). Injection of CO_2 starts the dissolution of CO_2 in groundwater according to the following reaction;

$$CO_{2(g)} \rightarrow CO_{2(aq)} + H_2O \rightarrow HCO_3^- + H^+ \rightarrow CO_3^{2-} + 2H^+ \quad (2)$$

Table 10 Surface complexation reactions and surface complexation constants on ferrihydrite (Dzombak and Morel, 1990; Appelo et al., 2002)

Surface Complexation Reactions	**Equilibrium Constants (log K)**
>(s)FeO^- + H^+ → >(s)FeOH	8.93
>(s)$FeOCo^+$ + H^+ → >(s)FeOH + Co^{2+}	0.46
>(s)$FeOH_2^+$ → >(s)FeOH + H^+	-7.29
>(s)$FeOHCa^{2+}$ → >(s)FeOH + Ca^{2+}	-4.97
>(s)$FeONi^+$ + H^+ → >(s)FeOH + Ni^{2+}	-0.37
>(s)$FeOZn^+$ + H^+ → >(s)FeOH + Zn^{2+}	-0.99
>(s)$FeOHSr^{2+}$ → >(s)FeOH + Sr^{2+}	-5.01
>(w)FeO^- + H^+ → >(w)FeOH	8.93
>(w)$FeOCo^+$ + H^+ → >(w)FeOH + Co^{2+}	3.01
>(w)$FeOH_2^+$ → >(w)FeOH + H^+	-7.29
>(w)$FeOHCa^{2+}$ → >(w)FeOH + Ca^{2+}	5.85
>(w)$FeOZn^+$ + H^+ → >(w)FeOH + Zn^{2+}	1.99
>(w)$FeOHSr^{2+}$ → >(w)FeOH + Sr^{2+}	6.58

Table 11 Cation exchange reactions and selectivity coefficients of Na-illite

Cation Exchange Reactions	**Selectivity Coefficients**
Na-illite + H^+ ⇔ H-illite + Na^+	1.0 (Gilbert and Laudelout, 1965)
Na-illite + K^+ ⇔ K-illite + Na^+	12.9 (Bradbury and Baeyens, 2000)
2Na-illite + Mg^{+2} ⇔ Mg-illite + 2Na^+	11.0 (Bradbury and Baeyens, 2005)
2Na-illite + Ca^{2+} ⇔ Ca-illite + 2Na^+	11.0 (Bradbury and Baeyens, 2005)
3Na-illite + Al^{3+} ⇔ Al-illite + 3Na^+	10.0 (Bradbury and Baeyens, 2005)
2Na-illite + Sr^{2+} ⇔ Sr-illite + 2Na^+	63.0 (Montoya et al., 2018)
2Na-illite + Ni^{2+} ⇔ Ni-illite + 2Na^+	11.0 (Bradbury and Baeyens, 2005)
2Na-illite + Co^{2+} ⇔ Co-illite + 2Na^+	19.9 (Montoya et al., 2018)
2Na-illite + Zn^{2+} ⇔ Zn-illite + 2Na^+	3.98 (Montoya et al., 2018)

Table 12 Kinetic Parameters

Mineral Name	**Surface Area (cm^2/g)**	**k_{25} ($mol/cm^2/s$)**	**Activation Energy (kJ/mol)**	**n**	**Source**
Albite	10	6.92×10^{-11}	65.0	0.45	(Palandri and Kharaka, 2004)
Calcite	10	5.01×10^{-1}	14.4	1.00	(Palandri and Kharaka, 2004)
Dawsonite	9.8	6.46×10^{-4}	36.1	0.50	(Zheng et al., 2013)
Dolomite	12.9	2.34×10^{-7}	43.5	0.50	(Xu et al., 2010)
Illite	151.6	1.05×10^{-14}	23.6	0.34	(Palandri and Kharaka, 2004)
K-feldspar	9.8	8.71×10^{-11}	51.7	0.50	(Palandri and Kharaka, 2004)

Quartz	9.8	4.52×10^{-14}	90.1	-	(Hellevang et al., 2013)
Kaolinite	151.6	4.89×10^{-12}	65.9	0.78	(Palandri and Kharaka, 2004)
Chlorite	9.8	8.2×10^{-9}	30	0.74	(Brandt et al., 2003)

Table 13 Chemical composition of fluid (US Geological Survey, 2015) in the initial system for all scenarios.

Species	**Concentrations (mg/l)**	**Species**	**Concentrations (mg/l)**
pH	6.42	$SiO_{2(aq)}$	1.5
HCO_3^-	116	Al^{3+}	0.077
Ca^{2+}	1100	Sr^{2+}	100
Cl^-	17350	Ni^{2+}	10
Mg^{2+}	378	Zn^{2+}	10
Na^+	9055	Co^{2+}	10
K^+	300		

Results

Characterization of Shale Samples

XRD Results

Table 14 summarizes semi-quantitative XRD results of shale samples from different geological units.

Conasauga Shale sample CS from Shelby County is dominated by carbonate minerals (Figure 5). Calcite constitutes 87.9% of the sample and dolomite constitutes only 1%. This unit has the highest carbonate and lowest quartz content. Clay mineral content is very low. Clay mineral peak intensity is very low in the XRD result due to carbonate domination. Albite ($NaAlSi_3O_8$) constitutes 8.7% of the sample. The sample contains a small amount of pyrite (1.1%). The total organic content (TOC) of this unit is 0.12%.

Conasauga Shale sample CSC from St. Claire County (Figure 6) is dominated by carbonates as well. Carbonates constitute 32.5% of the sample with 20.8% of calcite and 11.7% of dolomite. The quartz content of 22.8 % is higher than that of the Conasauga Shale CS. Albite content is 21.3% and pyrite content is 1.5%. The clay mineral content is 21.9%, including 13% of illite and 8.9% of chlorite. TOC of this unit is 0.88%.

Neal/Floyd Shale sample NFP from Pickens County is dominated by quartz and clay minerals. Quartz constitutes 50.3% and clay minerals constitute 30.2%. Clay minerals consist mainly of illite (24.4%) and chlorite (5.8%). The pyrite content (2%) and albite content (17.5%) are both higher than those in the Conasauga Shale. The TOC of this sample is 6.22%, much higher than that in the Conasauga Shale.

Chattanooga Shale sample CG from Greene County (Figure 8) is dominated by carbonates. Calcite constitutes 40.4% and dolomite constitutes 2.6%. Quartz content is 29% and albite content

is 10.5%. Pyrite content is 1.9%. Total clay content is 15.6% with 13.2% of illite and 2.4% of chlorite. TOC of this unit is 4.46% which is also higher than that in the Conasauga Shale.

Devonian Shale sample DH from Hale County (Figure 9) is dominated by carbonates. Calcite is 63.1% in this shale sample. This shale unit has the lowest sulfide content with 0.9% of pyrite. Illite constitutes 14.5% of the unit. This shale sample also has the lowest feldspar content with 4.3% albite.

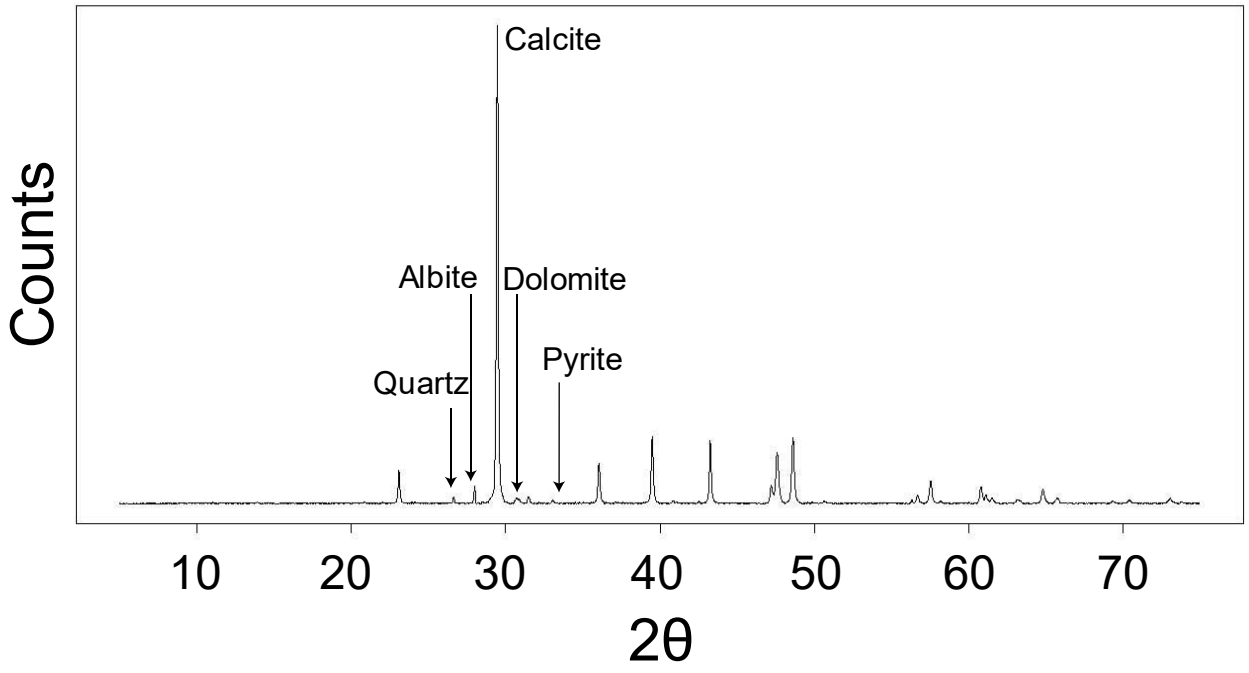

Figure 5 XRD result of Conasauga Shale Shelby County 14,181 ft.

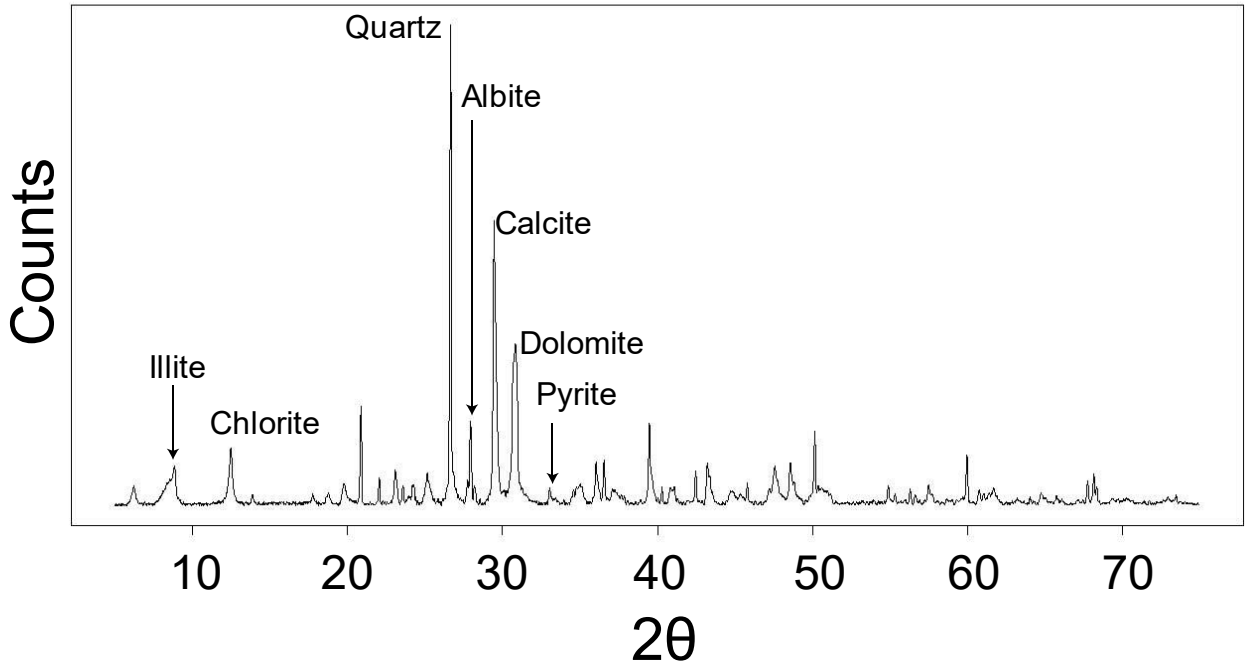

Figure 6 XRD result of Conasauga Shale St. Claire County 7,540 ft

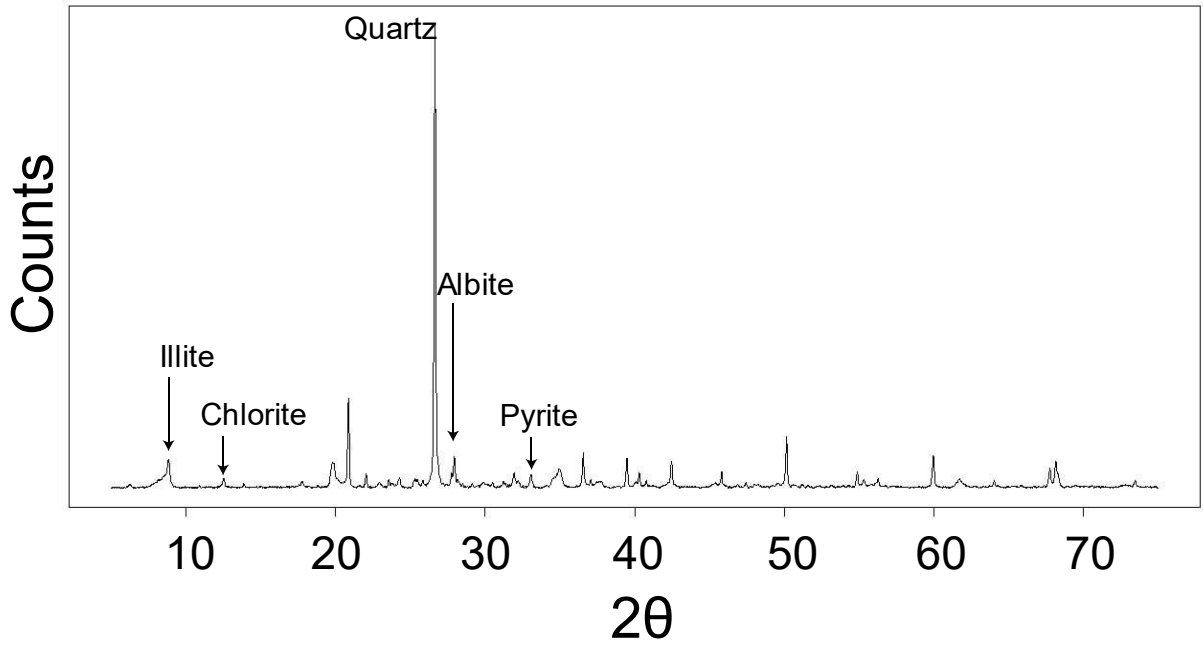

Figure 7 XRD result of Neal/Floyd Shale Pickens County 6,566-6,568 ft.

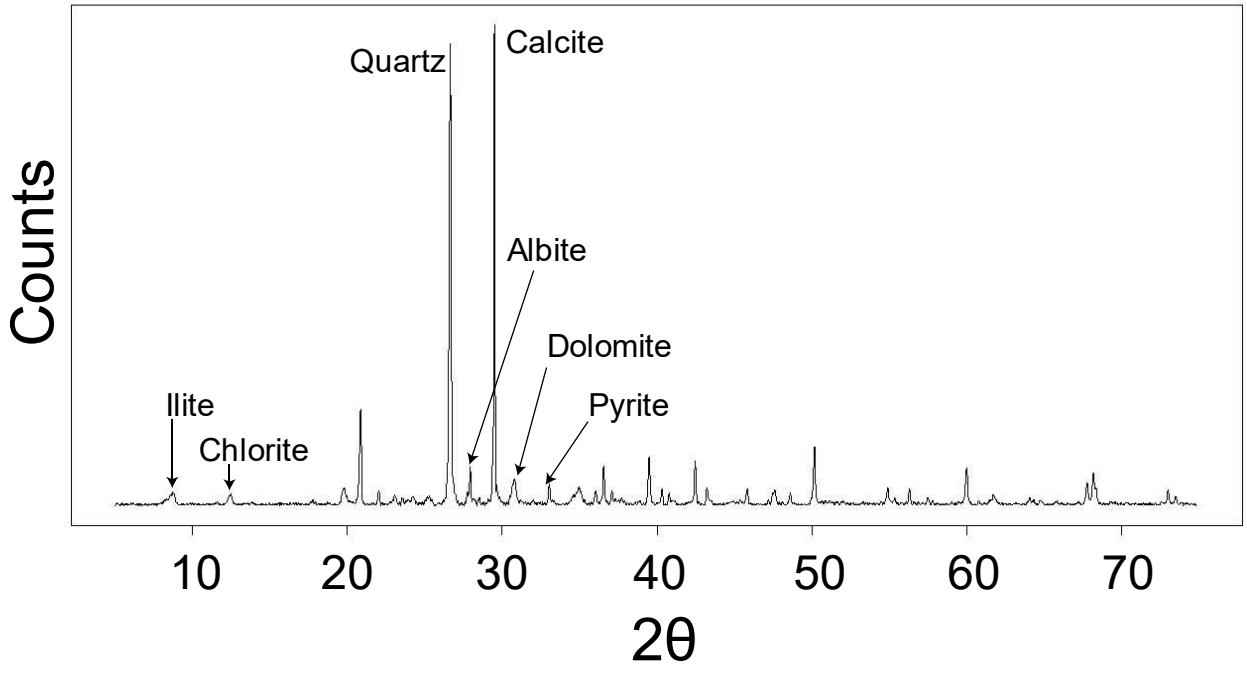

Figure 8 XRD result of Chattanooga Shale Greene 8441 ft.

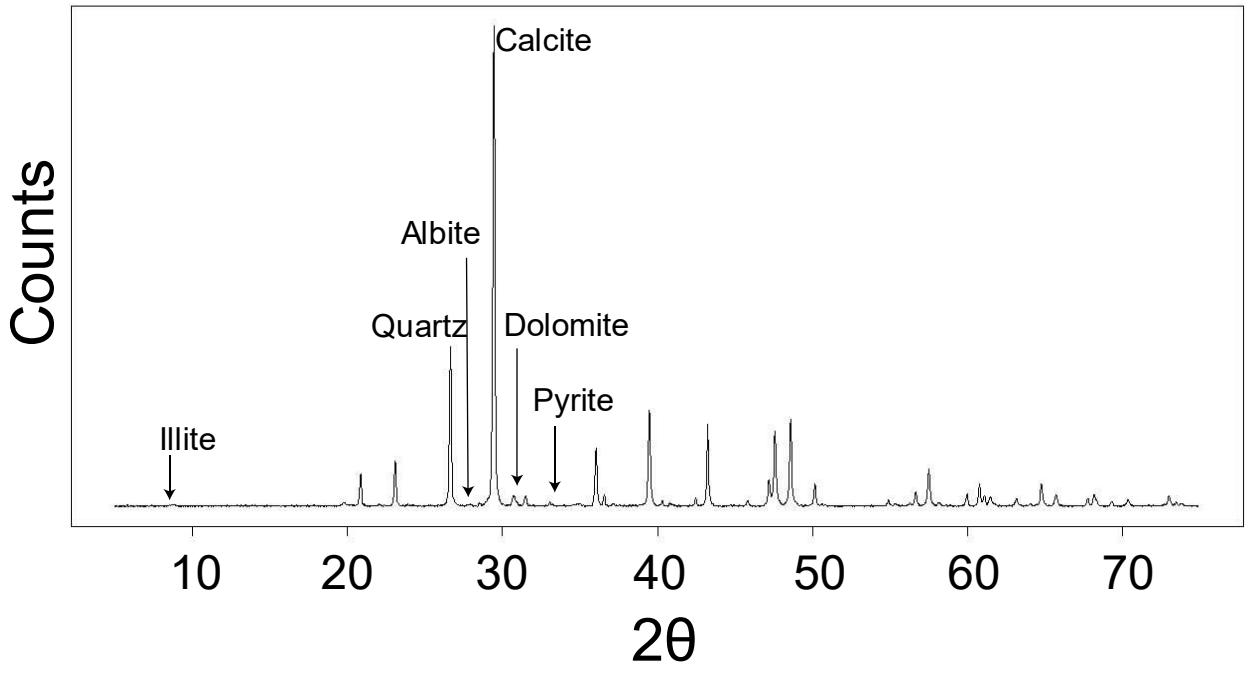

Figure 9 XRD result of Devonian Shale Hale County 10,301 ft.

XRF Results

X-ray Fluorescence (XRF) analysis was performed on the same set of shale samples to explore major and trace element concentrations. This study demonstrates the capability of combined XRD-XRF analysis for a more accurate evaluation of mineralogy and chemistry of fine-grained shales. Table 15 shows the summary of semi-quantitative XRF results of representative shale samples. The results are compared to the average concentrations in shales (Hem, 1985) and continental crust (Wedepohl, 1995).

The representative Conasauga Shale, Shelby County sample CS has high calcium (51%), low silica (7%), and low aluminum (0.02%) concentrations. XRD results of high calcite and low feldspar, quartz, and clay contents explain its bulk geochemical composition. This unit contains large calcite veins locally which may increase the calcium content significantly. This sample also contains a significant amount of strontium (645 mg/kg). This shale sample also contains significant amounts of trace elements, including vanadium, chromium, cobalt, nickel, copper, arsenic, barium, and lead, with respect to those in the continental crust (Table 15).

Neal/Floyd Shale, Pickens County sample NFP is rich in Al (11%) and Si (35%) compared to CS. A significant amount of clay and feldspar accounts for high Al and Si concentrations. This sample also has a higher sulfur and iron content than those in CS. The concentration of K in NFP is higher than that in CS due to the relatively high clay mineral content. The calcium concentration is very low, reflecting low calcite content. Concentrations of most trace elements (e.g., chromium, vanadium, nickel, zinc, molybdenum, and lead) in NFP are significantly higher than those in CS or average continental crust (Table 15). Titanium, manganese, iron, cobalt, copper, arsenic, strontium are other notable elements.

Conasauga Shale, St. Claire County sample CSC is rich in Al (8.62%) and Si (20%) due to its high clay mineral and feldspar (albite) content. This shale unit has the highest iron (2.6 wt %) and arsenic (16.8 mg/L) content among all samples analyzed, perhaps due to its high sulfide mineral content. Strontium content is high. Samples with higher carbonate mineral contents tend to be rich in strontium. The manganese content is also the highest relative to other shale units. One other significant trace element is copper which is the second-highest among these shale units. Sulfur content is also very significant in this shale sample with 0.90%. This sample also contains lead, molybdenum, nickel, cobalt, vanadium.

Chattanooga Shale, Greene County sample CG has a significant Al concentration. A significant amount of clay and feldspar are the reason for high Al concentration. It has approximately 13% of Si which is below the average content in the continental crust. This shale unit is rich in sulfur with respect to the average continental crust and shale. Moreover, cobalt and molybdenum contents are the second-highest among the shale units studied in this work. This unit also contains vanadium, titanium, chromium, manganese, iron, cobalt, nickel, copper, zinc, arsenic, strontium, barium, and lead.

Devonian Shale, Hale County sample DH has the highest Al concentration. A large amount of clay and feldspar would account for high Al concentrations. It has approximately 19% of Si which is below the average of continental crust and shale. This shale unit also contains a significant amount of calcium (25.5 %) and strontium (583 mg/L) due to its high carbonate mineral content. Moreover, barium content is the highest, at 767 mg/L. This unit also contains titanium, vanadium, chromium, manganese, cobalt, nickel, copper, arsenic, molybdenum, and lead.

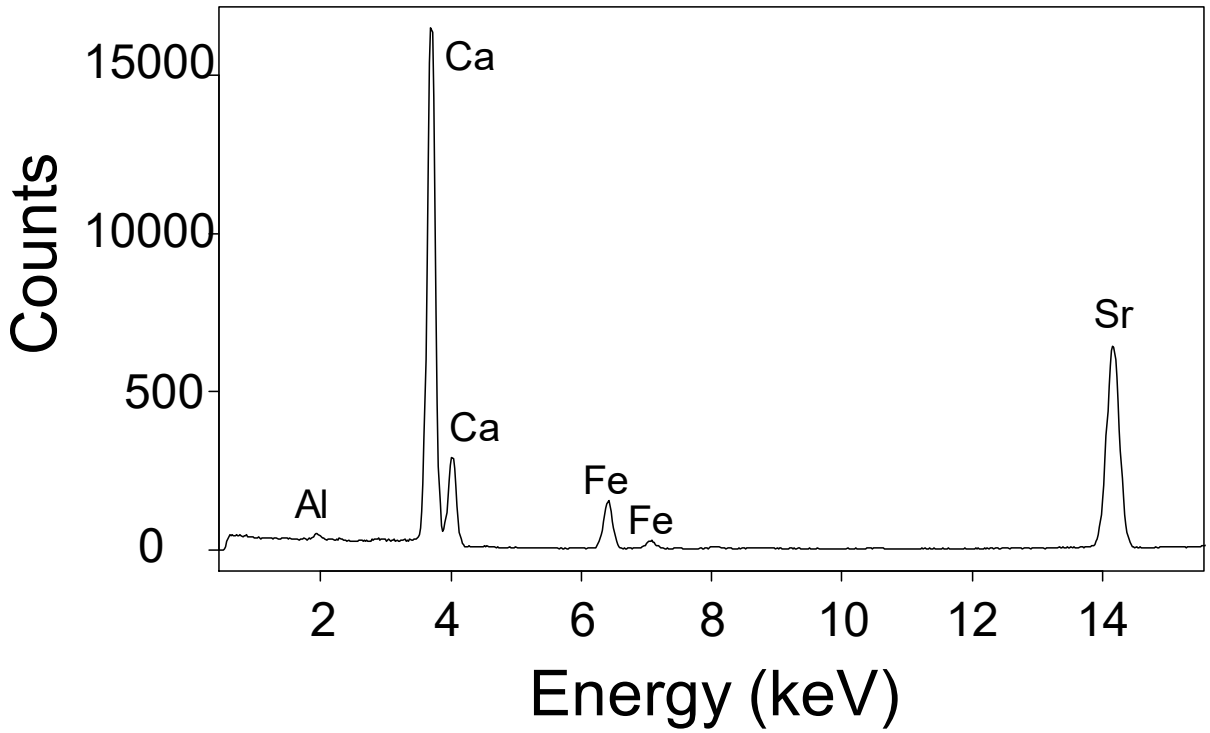

Figure 10 XRF result of Conasauga Shale Shelby County 14,181 ft.

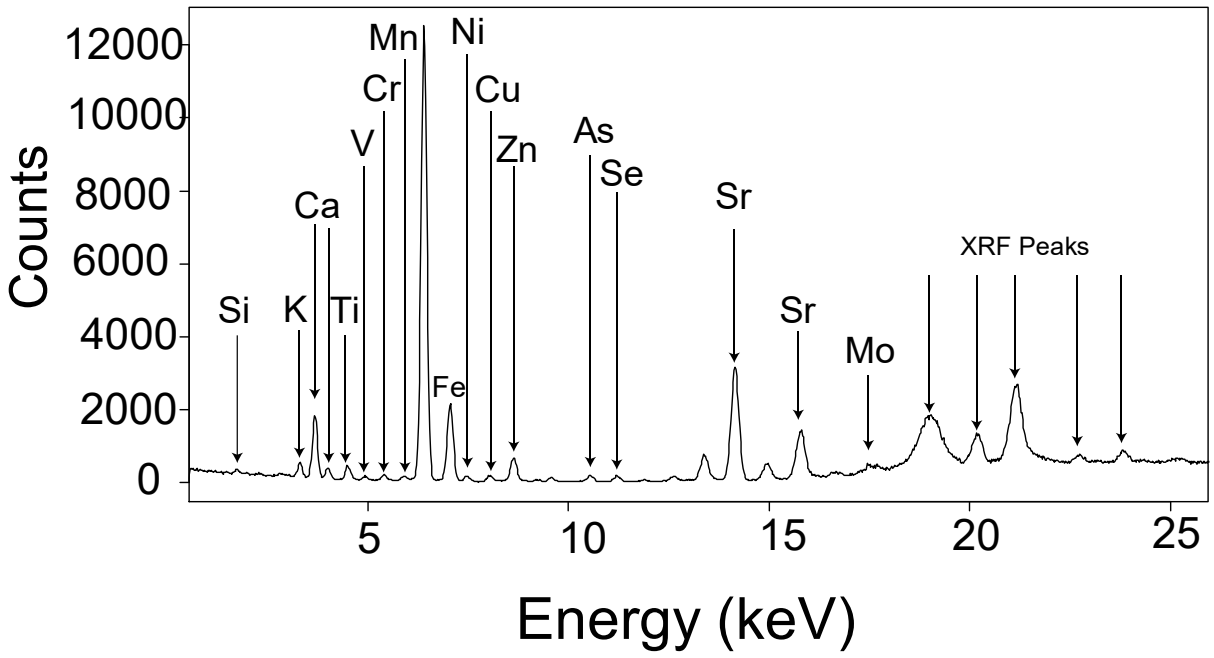

Figure 11 XRF result of Neal/Floyd Shale Pickens County 6,566-6,568 ft.

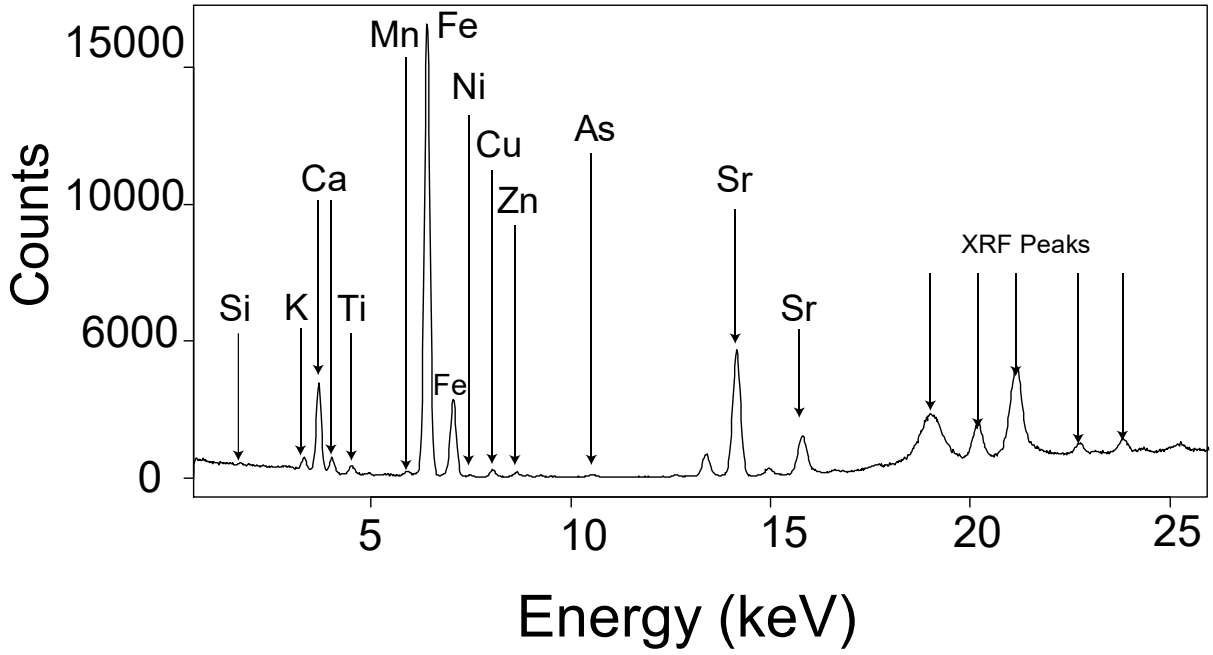

Figure 12 XRF result of Conasauga Shale St. Claire County 7,540 ft

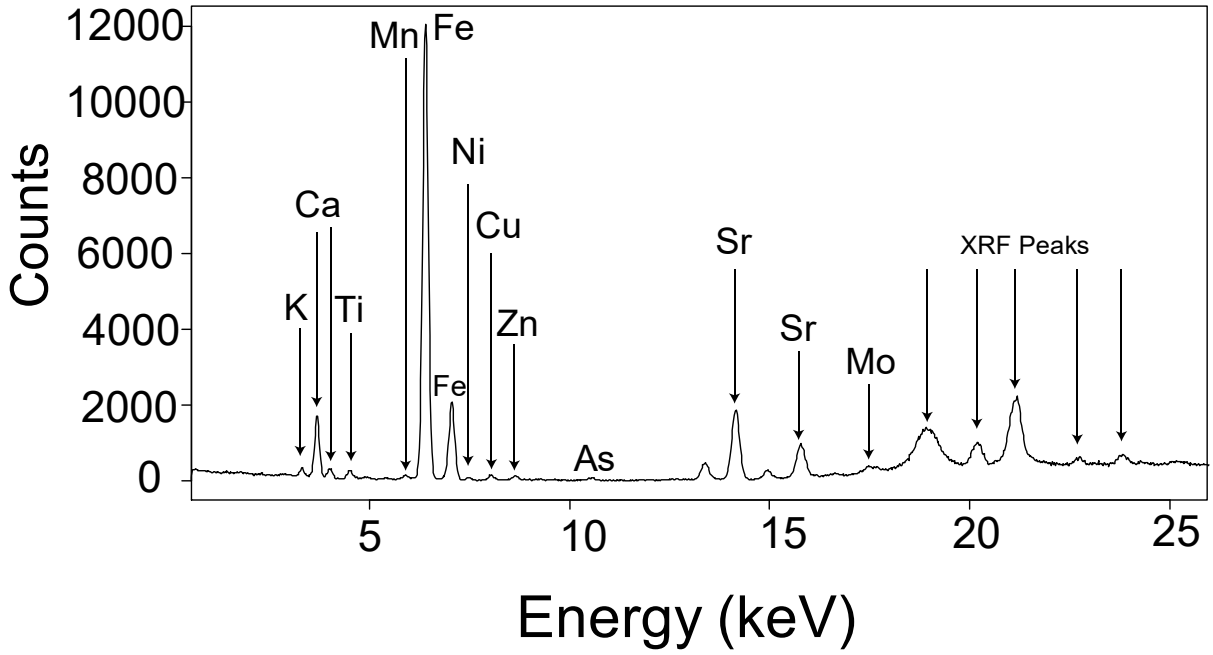

Figure 13 XRF result of Chattanooga Shale Greene 8441 ft.

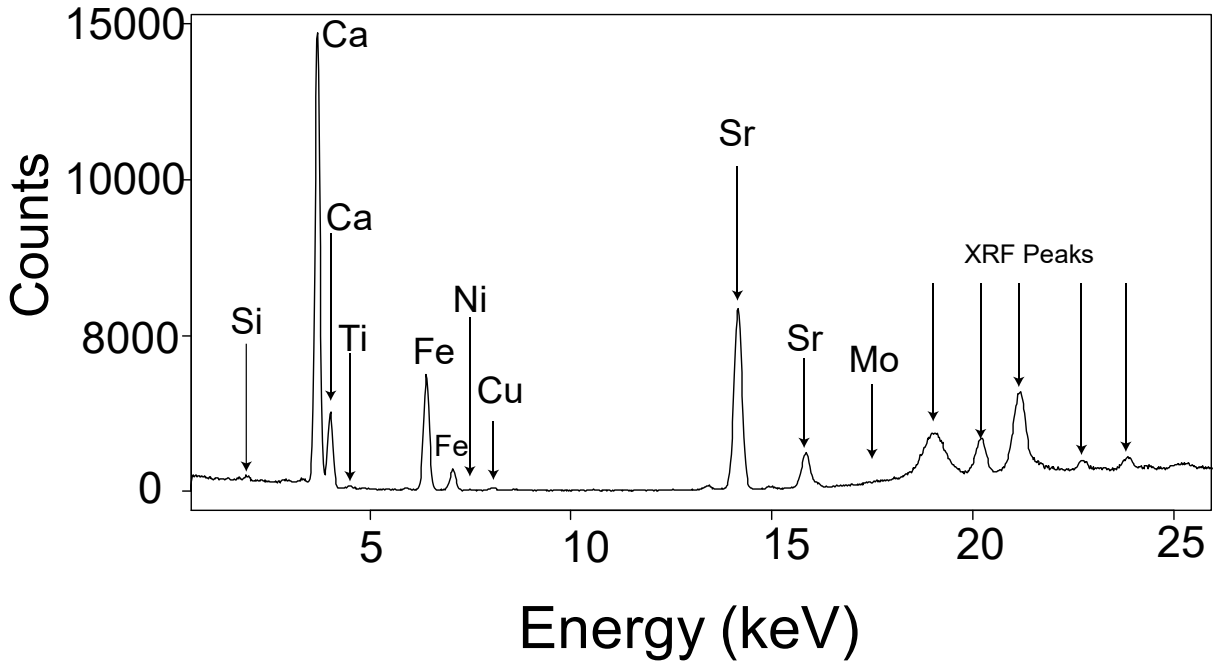

Figure 14 XRF result of Devonian Shale Hale County 10,301 ft.

Table 14 Semi-quantitative XRD results of CS (Conasauga Shale Shelby County), NFP (Neal/Floyd Shale Pickens County) CSC (Conasauga Shale St. Claire County), CG (Chattanooga Shale Greene County), DH (Devonian Shale Hale County)

	Quartz wt.%	Albite wt.%	Calcite wt.%	Dolomite wt.%	Pyrite wt.%	Illite wt.%	Chlorite wt.%	Total Carbonates wt.%	Total Clays wt.%
CS	1.3	8.7	87.9	1	1.1	0	0	88.9	0
NFP	50.3	17.5	0	0	2	24.4	5.8	0	30.2
CSC	22.8	21.3	20.8	11.7	1.5	13	8.9	32.5	21.9
CG	29	10.5	40.4	2.6	1.9	13.2	2.4	43	15.6
DH	16.3	4.3	63.1	0.9	0.9	14.5	0	64	14.5

Table 15 XRF results of CS (Conasauga Shale Shelby County), NFP (Neal/Floyd Shale Pickens County) CSC (Conasauga Shale St. Claire County), CG (Chattanooga Shale Greene County), DH (Devonian Shale Hale County)

		CS	NFP	CSC	CG	DH	Average Crust	Average Shale
Al	**wt%**	0.1	11.17	8.62	7.77	13.48	7.74	8.01
Si	**wt%**	7.03	35.9	20.55	13.72	19.38	30.35	26
S_{total}	**wt%**	0.68	0.97	0.91	0.79	0.78	0.1	0.19
Cl	**wt%**	0.00492	0.00634	0.00997	0.00703	0.00183	0.064	0.017
K	**wt%**	0	2.04	2.39	0.89	0.28	2.87	2.49
Ca	**wt%**	51.73	3.92	6.63	3.62	25.5	2.95	2.25
Ti	**wt%**	0.01	0.36	0.29	0.18	0.01	0.31	0.44
V	**wt%**	0.00061	0.01737	0.00833	0.0085	0.0066	0.0053	0.0101
Cr	**wt%**	0.00054	0.06029	0.00508	0.00175	0.00088	0.0035	0.0423
Mn	**wt%**	0.02	0.02	0.03	0.01	0	0.05	0.06
Fe	**wt%**	0.17	1.96	2.61	1.85	0.35	3.09	3.88
Co	**wt%**	0.00058	0.00083	0.00038	0.001	0.00072	0.00116	0.00081
Ni	**wt%**	0.00192	0.01537	0.00544	0.00445	0.00056	0.00186	0.0029
Cu	**wt%**	0.00026	0.0048	0.00849	0.00365	0.00128	0.00143	0.0045

Zn	**wt%**	0	0.04106	0.00356	0.00103	0	0.0052	0.013
As	**wt%**	0.00143	0.00079	0.00169	0.00144	0.00079	0.0002	0.0009
Sr	**wt%**	0.06344	0.03302	0.04524	0.02169	0.05838	0.0316	0.029
Mo	**wt%**	0	0.0013	0.00033	0.00077	0.0001	0.00014	0.00042
Ba	**wt%**	0.02374	0.03227	0.04539	0.03543	0.07674	0.0668	0.025
Pb	**wt%**	0.00164	0.00445	0.00276	0.0022	0.00169	0.0017	0.008
Th	**wt%**	0.00048	0.00059	0.00073	0.00062	0.00051	0.00103	0.0013

Table 16 Average Crust and Shale ratios (average shale is from Hem, 1985, average crust is from Wedepohl, 1995)

		CS Crust Ratio	**NFP Crust Ratio**	**CSC Crust Ratio**	**CG Crust Ratio**	**DH Crust Ratio**	**CS Average Shale Ratio**	**NFP Average Shale Ratio**	**CSC Average Shale Ratio**	**CG Average Shale Ratio**	**DH Average Shale Ratio**
Al	**wt%**	0.01	1.44	1.11	1.00	1.74	0.01	1.39	1.08	0.97	1.68
Si	**wt%**	0.23	1.18	0.68	0.45	0.64	0.88	1.38	0.79	0.53	0.75
S_{total}	**wt%**	6.80	9.70	9.10	7.90	7.80	0.08	5.11	4.79	4.16	4.11
Cl	**mg/kg**	0.08	0.10	0.16	0.11	0.03	6.14	0.37	0.59	0.41	0.11
K	**wt%**	0.00	0.71	0.83	0.31	0.10	0.00	0.82	0.96	0.36	0.11
Ca	**wt%**	17.54	1.33	2.25	1.23	8.64	6.46	1.74	2.95	1.61	11.33
Ti	**wt%**	0.03	1.16	0.94	0.58	0.03	0.00	0.82	0.66	0.41	0.02
V	**mg/kg**	0.12	3.28	1.57	1.60	1.25	0.77	1.72	0.82	0.84	0.65
Cr	**mg/kg**	0.15	17.23	1.45	0.50	0.25	0.67	1.43	0.12	0.04	0.02
Mn	**wt%**	0.40	0.40	0.60	0.20	0.00	0.00	0.33	0.50	0.17	0.00
Fe	**wt%**	0.06	0.63	0.84	0.60	0.11	0.02	0.51	0.67	0.48	0.09
Co	**mg/kg**	0.50	0.72	0.33	0.86	0.62	0.72	1.02	0.47	1.23	0.89
Ni	**mg/kg**	1.03	8.26	2.92	2.39	0.30	2.40	5.30	1.87	1.53	0.19

Cu	**mg/kg**	0.18	3.36	5.94	2.55	0.89	0.33	1.07	1.89	0.81	0.28
Zn	**mg/kg**	0.00	7.90	0.68	0.20	0.00	0.00	3.16	0.27	0.08	0.00
As	**mg/kg**	7.17	3.94	8.43	7.19	3.94	1.79	0.88	1.87	1.60	0.88
Sr	**mg/kg**	2.01	1.04	1.43	0.69	1.85	79.20	1.14	1.56	0.75	2.01
Mo	**mg/kg**	0.00	9.30	2.34	5.51	0.74	0.00	3.10	0.78	1.84	0.25
Ba	**mg/kg**	0.36	0.48	0.68	0.53	1.15	29.64	1.29	1.82	1.42	3.07
Pb	**mg/kg**	0.97	2.62	1.63	1.30	0.99	2.05	0.56	0.35	0.28	0.21
Th	**mg/kg**	0.46	0.57	0.71	0.60	0.49	0.60	0.45	0.56	0.47	0.39

Electron Microprobe Analysis

Polished sections of samples from the Conasauga Shale Shelby County (CS), Neal (Floyd) Shale Pickens County (NFP), Conasauga Shale St. Claire County (CSC), Chattanooga Shale Greene County (CG), and Devonian Shale Hale County (DH) were prepared to map element distribution using Electron Microprobe (EMP).

Conasauga Shale Shelby County (CS) – 14181

Figure 15 shows the elemental maps of Al, Ca, Fe and Si. EMP results show that calcium is by far the most dominant element compared to Al, Fe, and Si. EMP results show significantly uneven elemental distributions. Although Ca is dominant throughout the elemental map, Al and Si are concentrated at the top of the elemental map. Fe is concentrated in far fewer certain spots with respect to other elements. The EMP results are coherent with XRD and XRF results, suggesting calcite is the predominated mineral and Ca represents the most abundant element. Albite, quartz, and pyrite are present in the samples in relatively small quantities, reflected by relatively low contents of Al, Fe, and Si in XRF and EMP results.

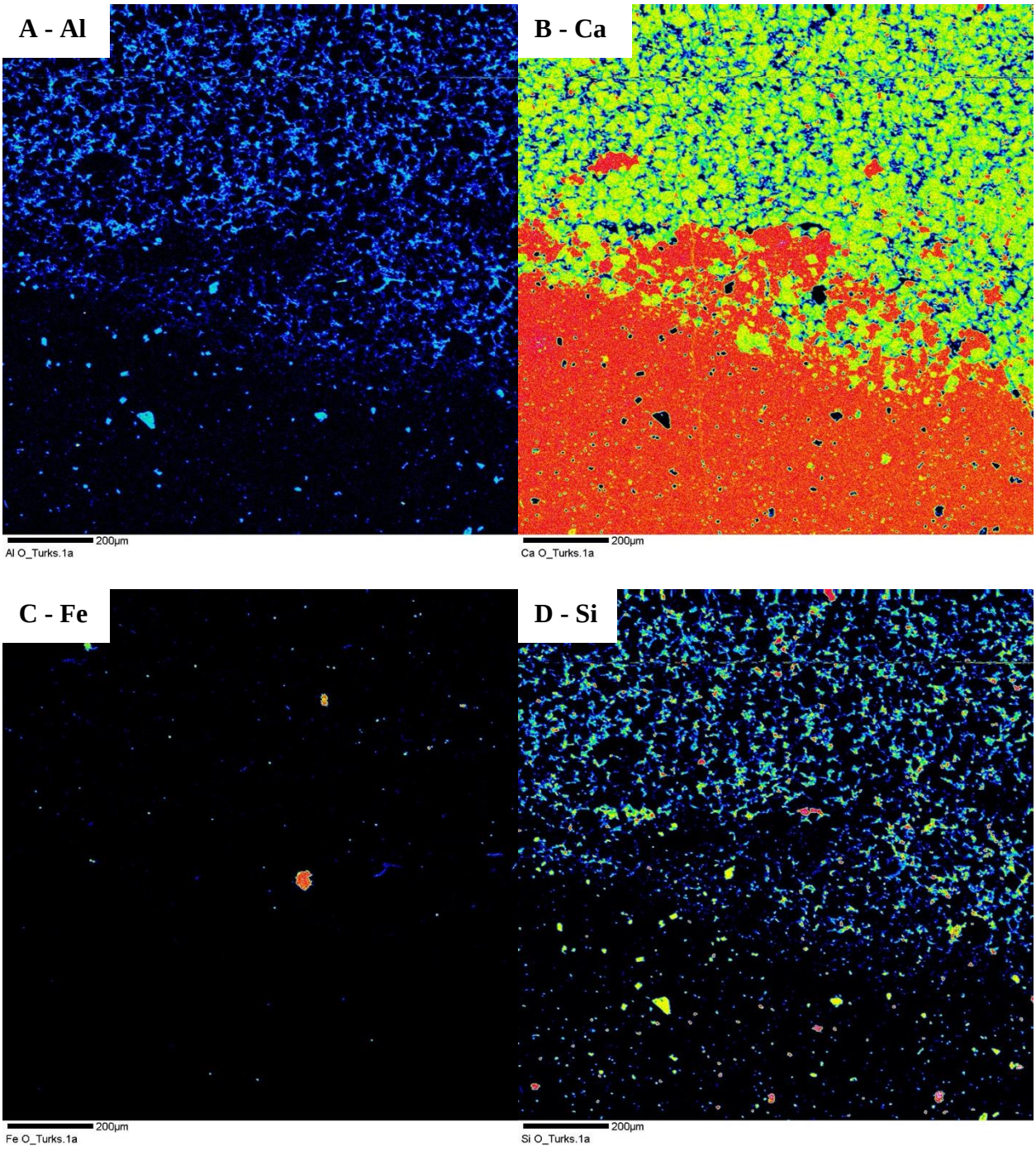

Figure 15 EMP Results of Conasauga Shale Shelby County (CS) – 14181 (Al, Fe, Ca, Si) (Red = High Concentration, Black = Low Concentration)

Neal (Floyd) Shale Pickens County (NFP) – 6568

Figure 16-Figure 18 show the elemental maps of Al, Fe, K, Ca, and Mg. Al and K are dominating the sample. Furthermore, the spatial correlation between Al and K is striking. Unlike the widespread distribution of Al and K, Ca and Mg seem to be concentrated along the bedding planes where carbonate minerals are present. Fe is concentrated in far fewer certain spots with respect to other elements. The spatial correlation between Ca and Mg, as well as among Al and K are also demonstrated in Figure 18. XRD, XRF, and EMP results reveal a high content of Al, Si, and K-bearing silicate and clay minerals, and Ca- and Mg-bearing carbonate minerals present in small quantity.

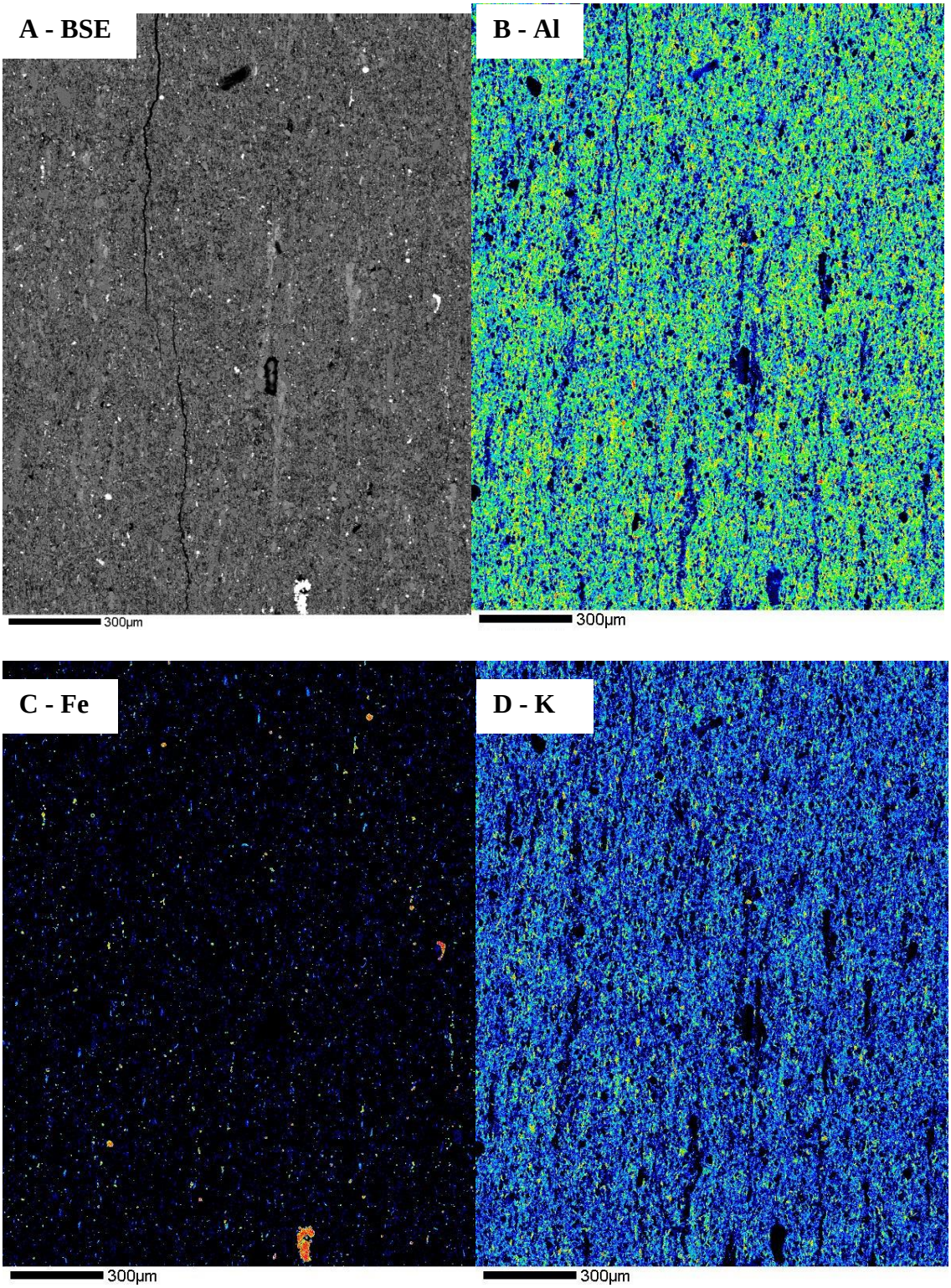

Figure 16 Neal (Floyd) Shale Pickens County (NFP) – 6568 (BSE, Al, Fe, K) (Red = High Concentration, Black = Low Concentration)

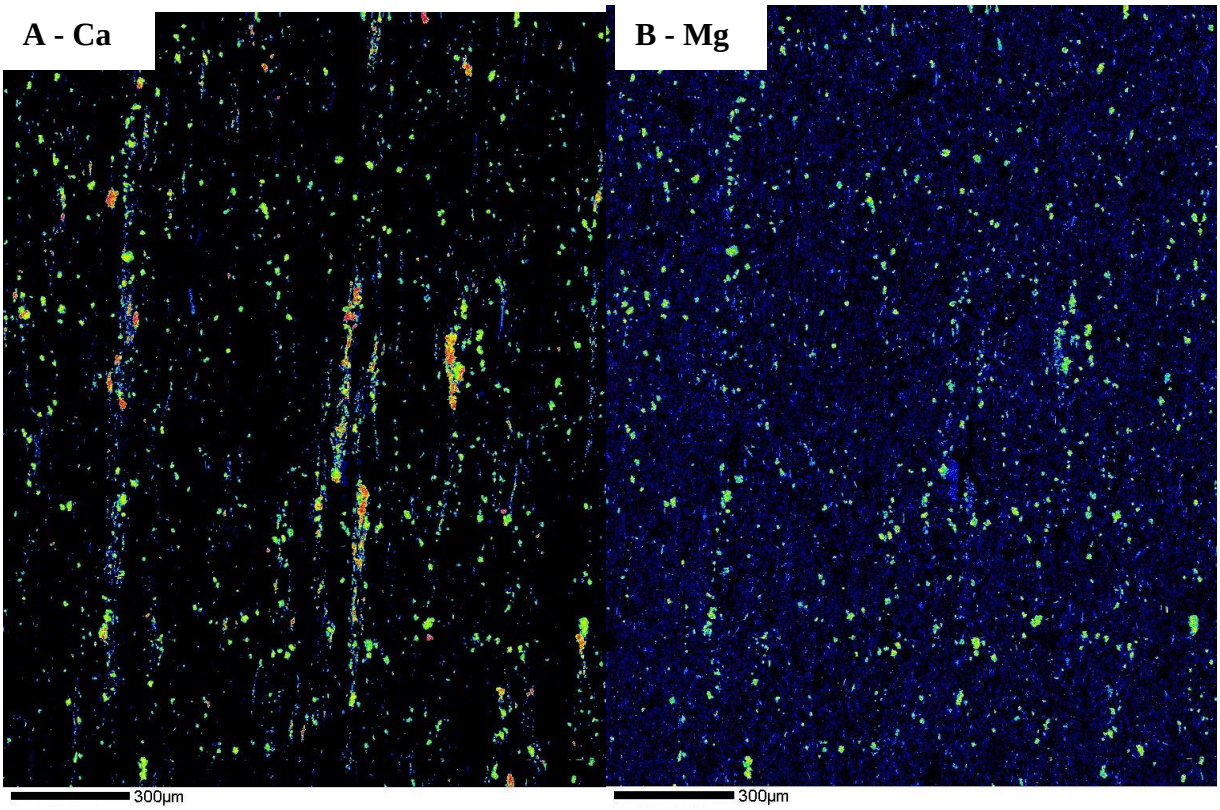

Figure 17 Neal (Floyd) Shale Pickens County (NFP) – 6568 (Ca, Mg) (Red = High Concentration, Black = Low Concentration)

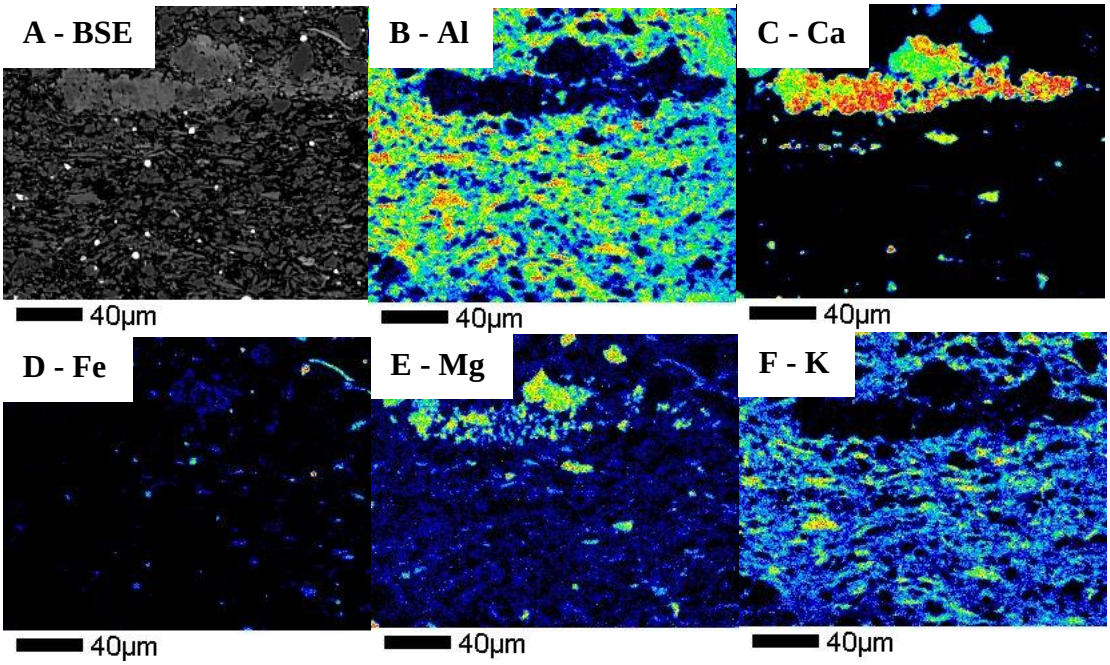

Figure 18 Neal (Floyd) Shale Pickens County (NFP) – 6568 (BSE, Al, Ca, Fe, Mg, K) (Red = High Concentration, Black = Low Concentration)

Conasauga Shale St. Claire County – 7558

Figure 19-Figure 21 show BSE image and elemental maps of Al, Si, K, Fe, S, Mg, Ca, Na, Mn, Ti. BSE image clearly shows the bedding planes. Al, Si, K, and Ca are dominating the sample. The spatial correlation between Al, K, and Si is striking, revealing high contents of silicate and clay minerals. Another strong spatial correlation can be observed between Ca and Mg in certain spots as big grains. This and XRD results suggest the presence of calcite and a small quantity of dolomite. The strong spatial correlation between Fe and S and XRD results reveals the presence of iron sulfide minerals (pyrite) in small quantities. Ti and Mn were also analyzed to see if there is a correlation, however, the results are inconclusive due to their low concentration.

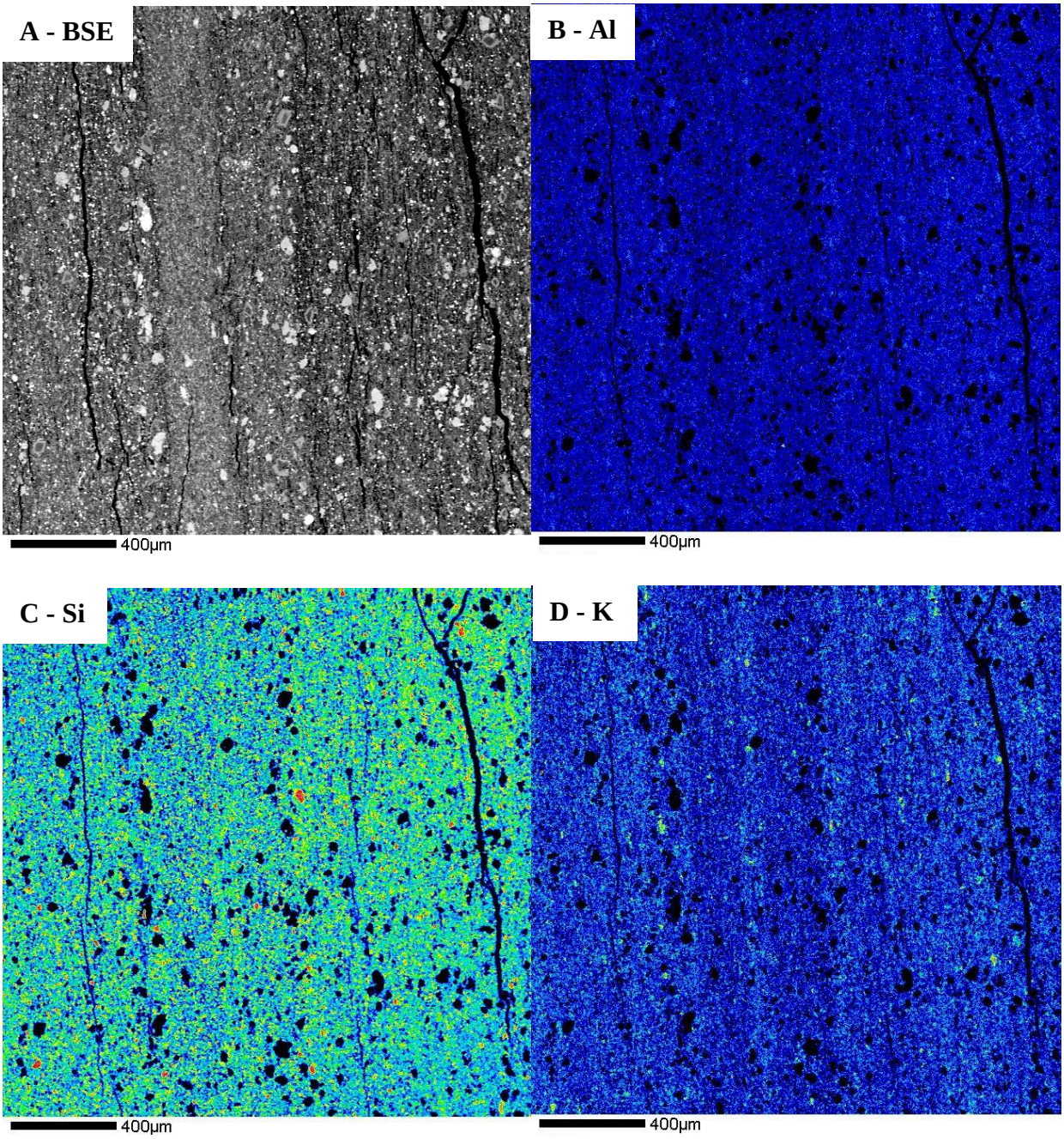

Figure 19 Electron Microprobe Results of Conasauga Shale St. Claire County – 7558 (BSE, Al, Si, K) (Red = High Concentration, Black = Low Concentration)

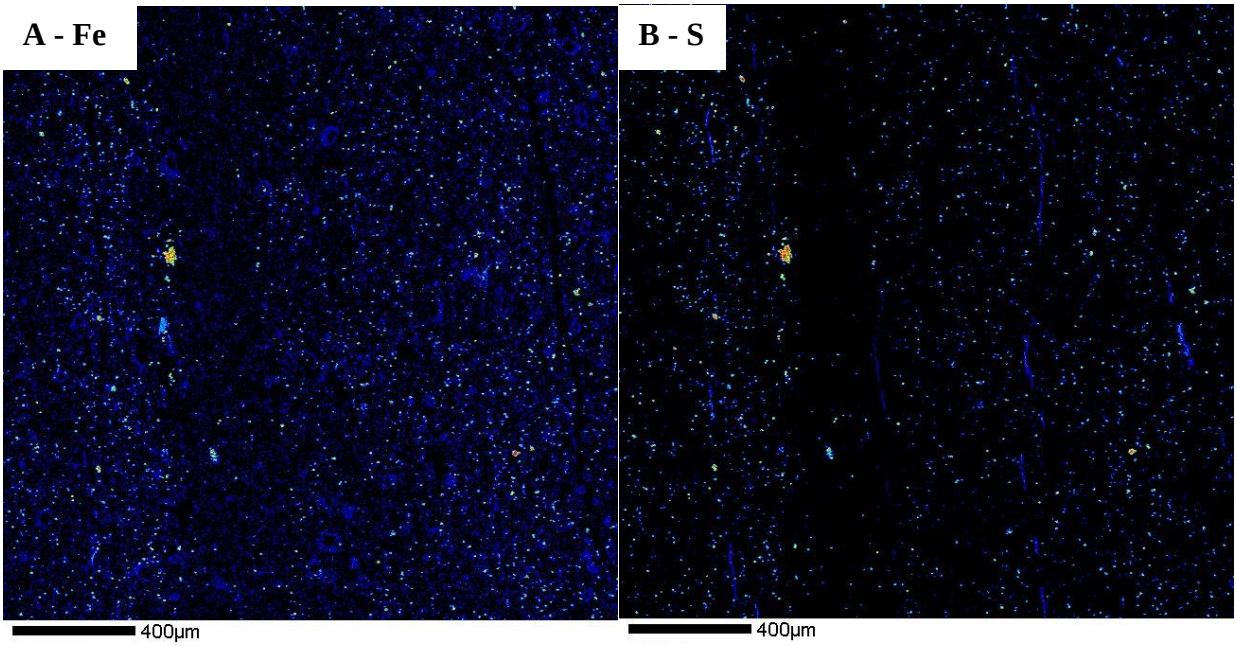

Figure 20 Electron Microprobe Results of Conasauga Shale St. Claire County – 7558 (Fe, S) (Red = High Concentration, Black = Low Concentration)

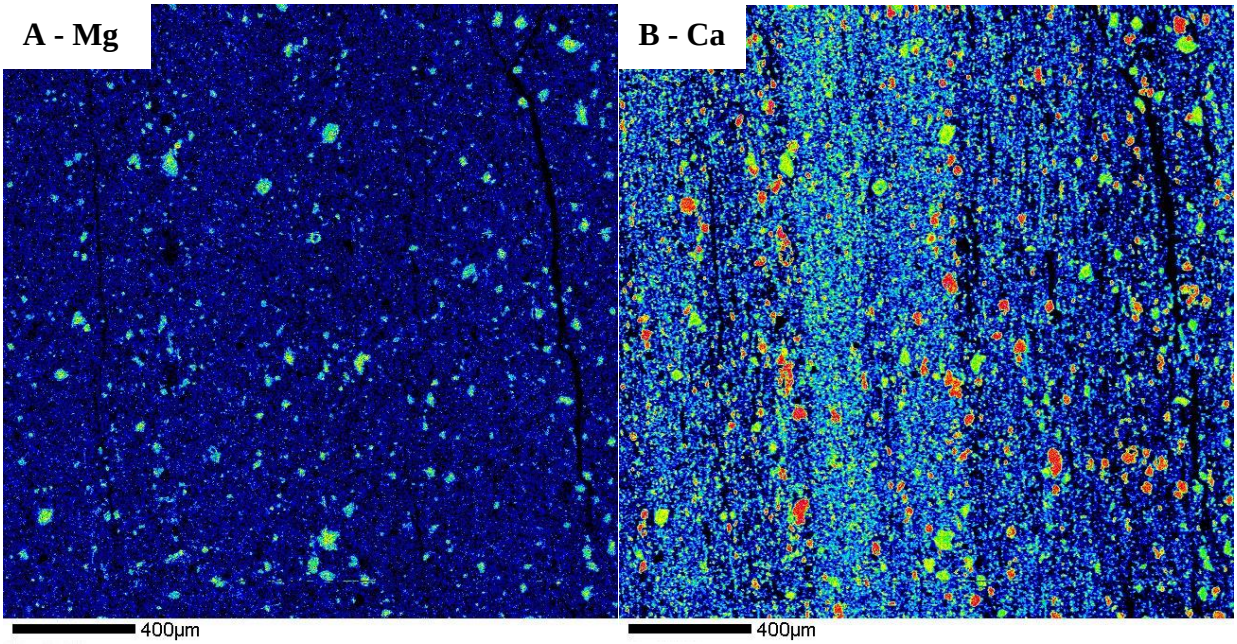

Figure 21 Electron Microprobe Results of Conasauga Shale St. Claire County – 7558 (Mg, Ca) (Red = High Concentration, Black = Low Concentration)

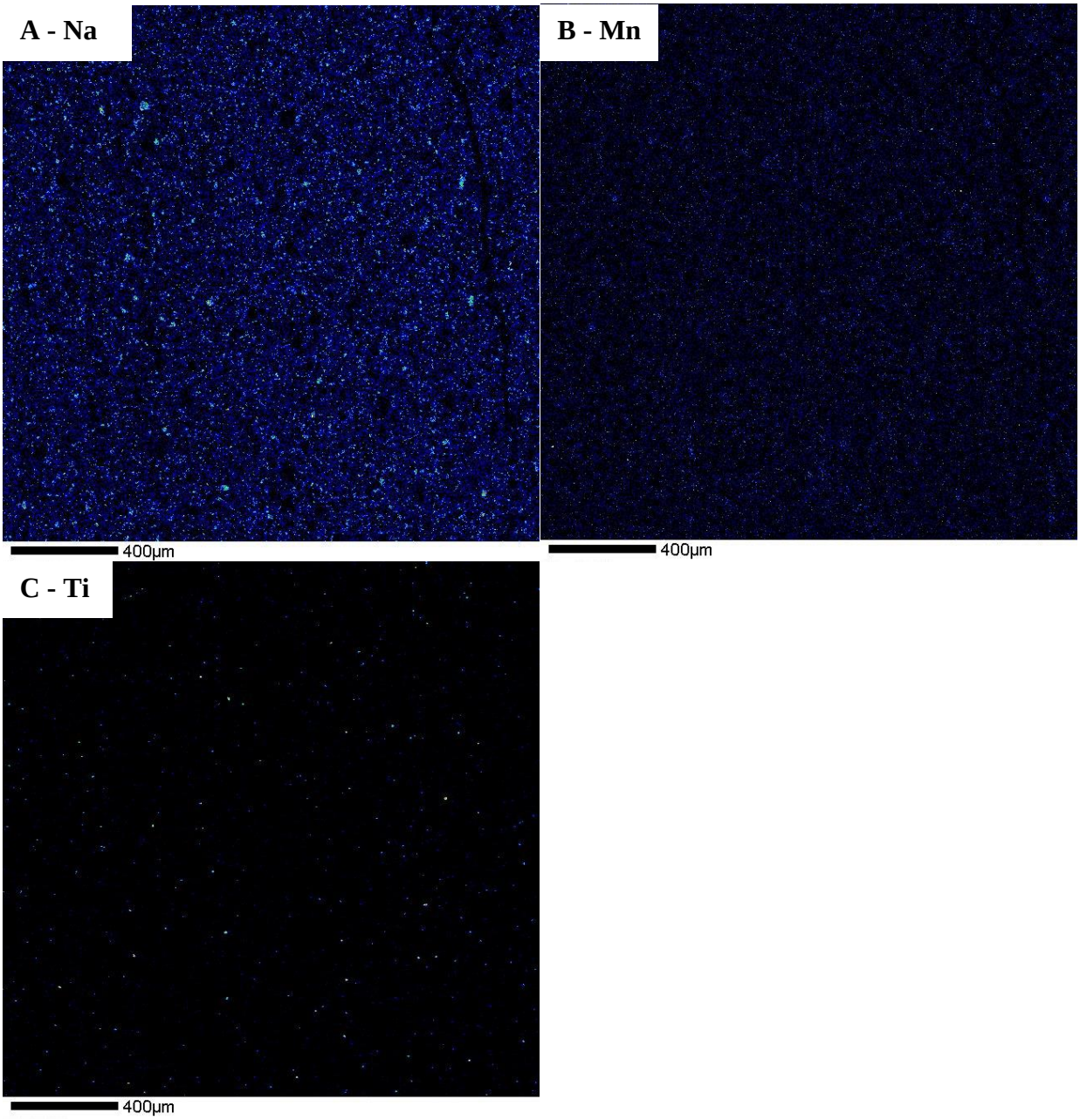

Figure 22 Electron Microprobe Results of Conasauga Shale St. Claire County – 7558 (Na, Mn, Ti) (Red = High Concentration, Black = Low Concentration)

Chattanooga Shale Greene County – 8445

Figure 23-Figure 26 show BSE image and elemental maps of Al, Si, K, Ca, Mg, S, Fe, Ti, Mn, Na. BSE image does not reveal clear bedding planes. Al, K, Si, and Mg are dominating the sample. The spatial correlation between Al, K, and Si reveals high contents of silicate and clay minerals. The unoriented and scattered distribution of Ca-rich grains is observed in certain parts of the sample. The strong spatial correlation is between Fe and S and XRD results support the presence of iron sulfide minerals (pyrite) in small quantities. Furthermore, Mg is dispersed in the EMP image, suggesting the presence of a very small quantity of dolomite in this shale sample.

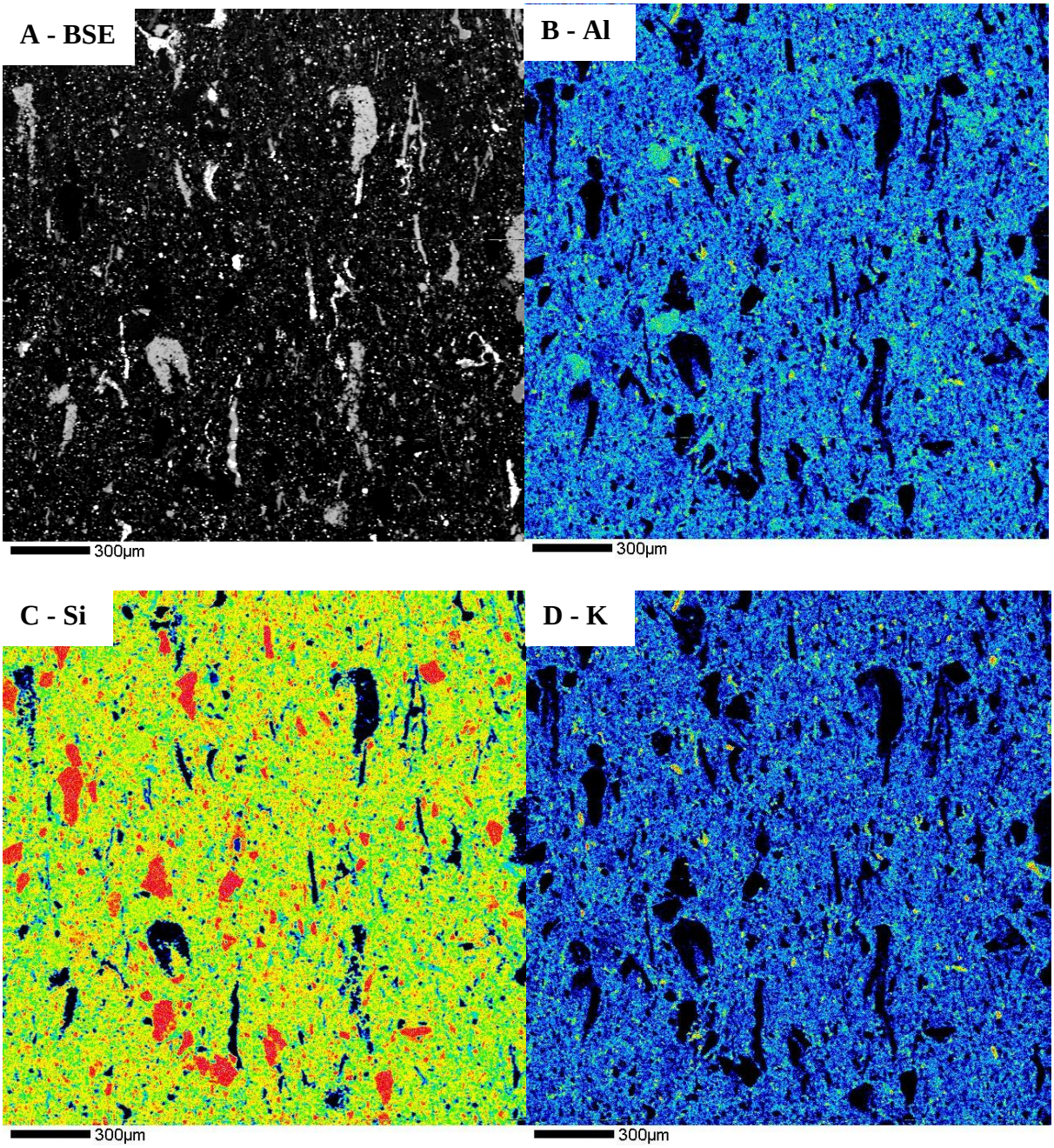

Figure 23 EMP Results of Chattanooga Shale Greene County – 8445 (BSE, Al, Si, K) (Red = High Concentration, Black = Low Concentration)

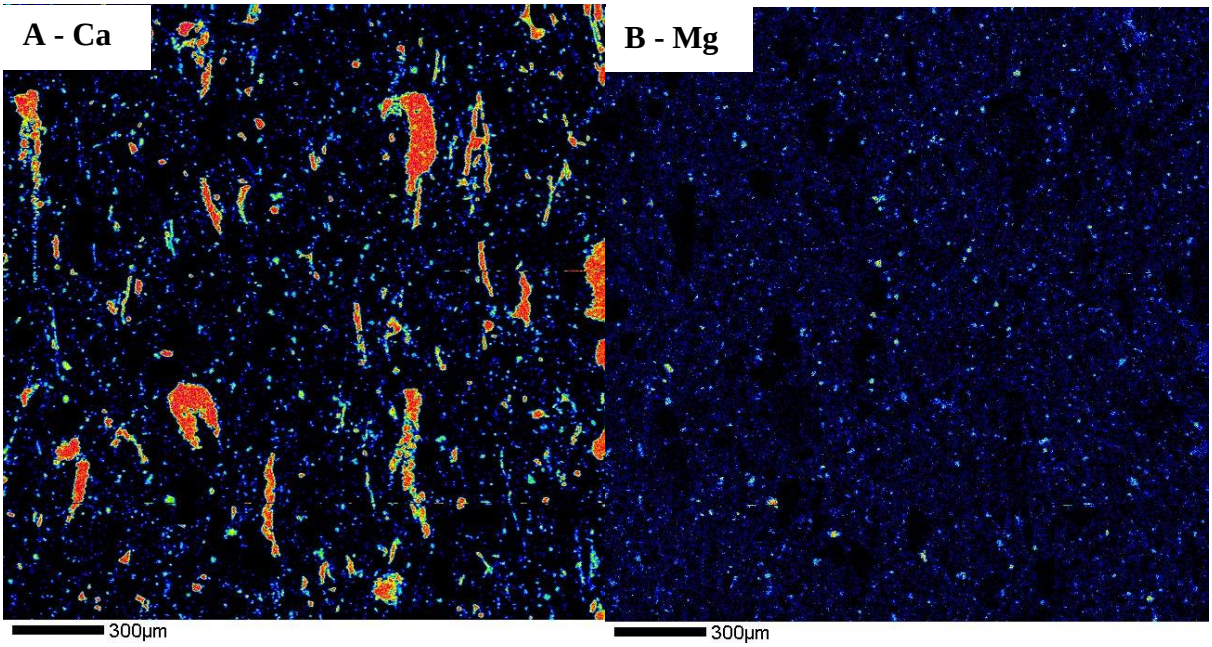

Figure 24 EMP Results of Chattanooga Shale Greene County – 8445 (Ca, Mg) (Red = High Concentration, Black = Low Concentration)

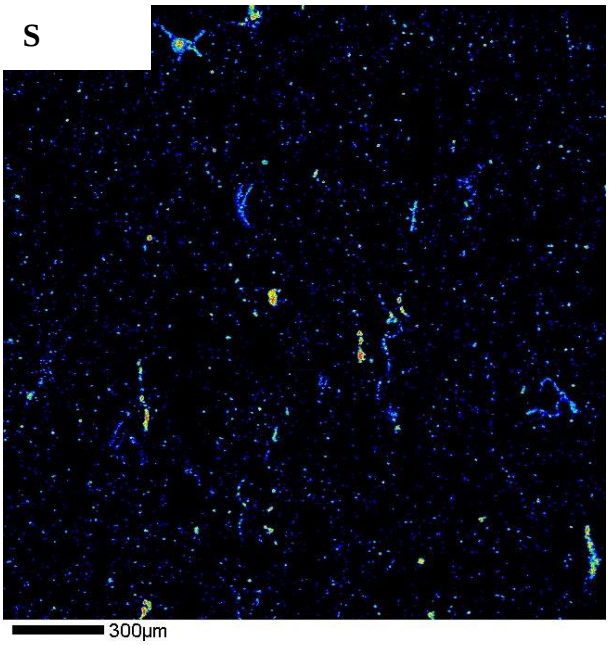

Figure 25 EMP Results of Chattanooga Shale Greene County – 8445 (S) (Red = High Concentration, Black = Low Concentration)

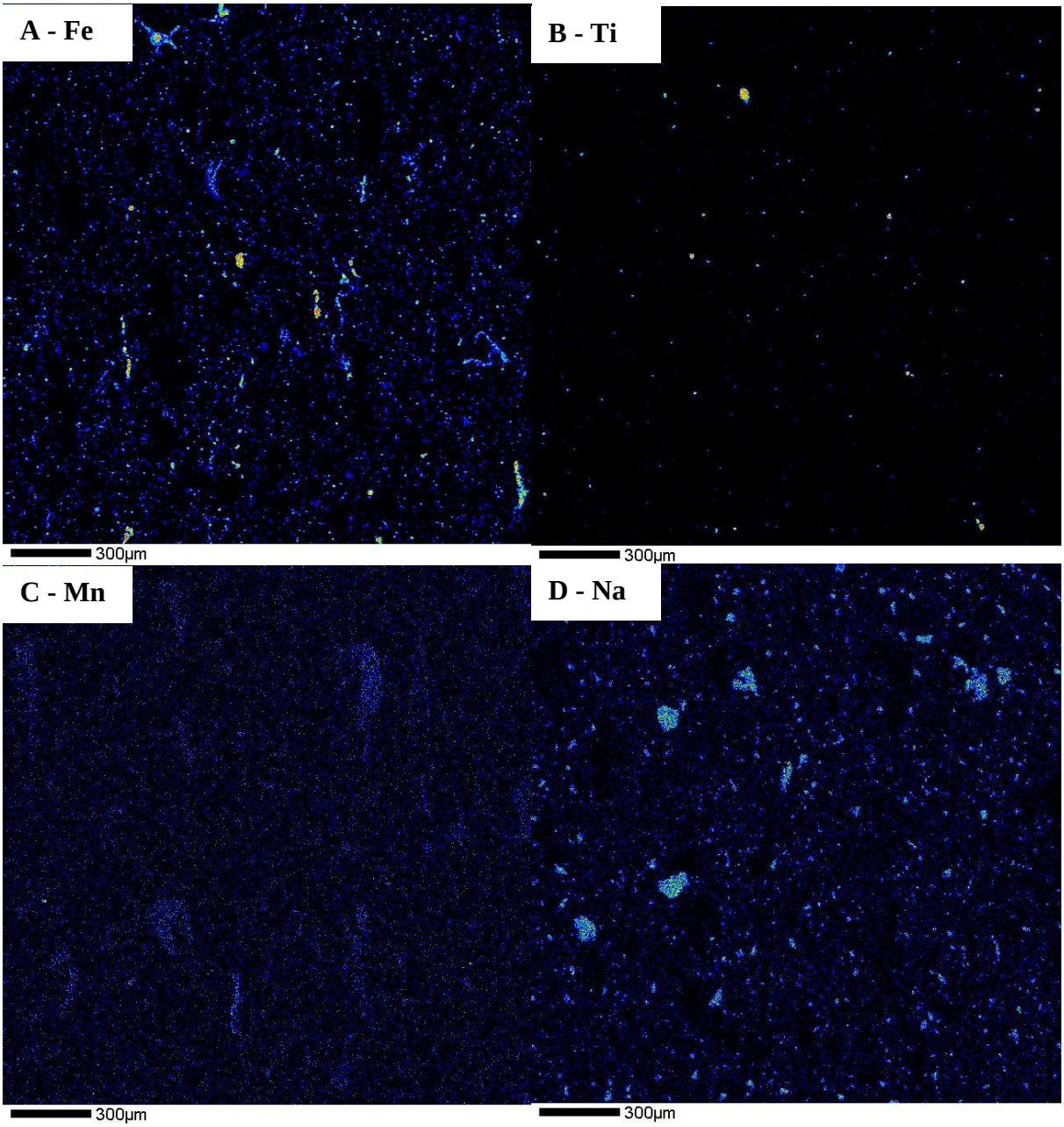

Figure 26 EMP results of Chattanooga Shale Greene County – 8445 (Fe, Ti, Mn, Na) (Red = High Concentration, Black = Low Concentration)

Devonian Shale Hale County – 10354

Figure 27-Figure 29 show BSE image and elemental maps of Al, Ca, Fe, K, Mg, Mn, Na, Ti, S, and Si. BSE does not reveal clear bedding planes. The high concentration of Ca is striking. Similar to other shale samples, there is a clear spatial correlation between Al, K, and Si, as well as between Fe and S. These correlations and XRD results suggest the presence of silicate, clay, and sulfide minerals.

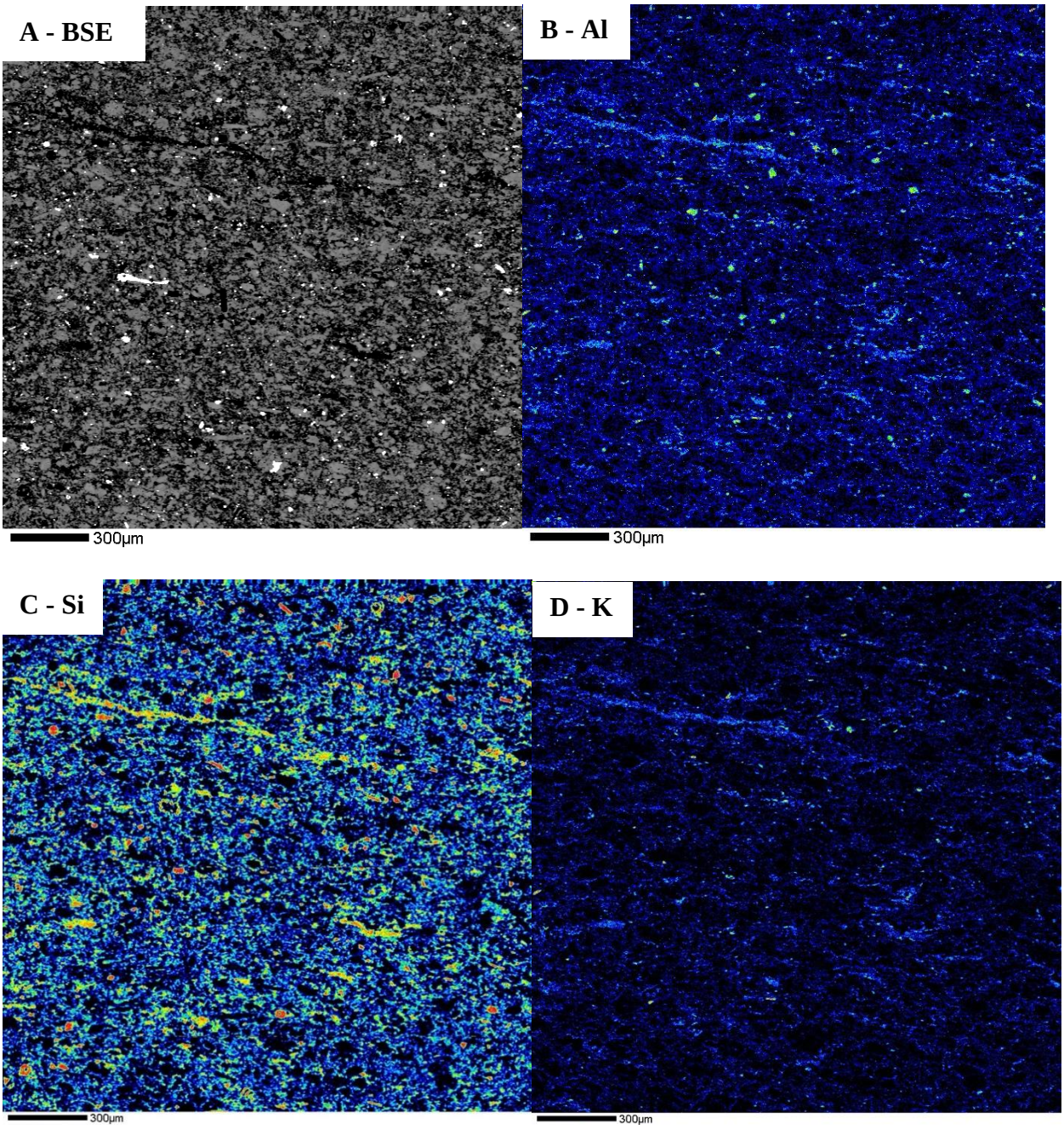

Figure 27 EMP Results of Devonian Shale Hale County – 10354 (BSE, Al, Si, K) (Red = High Concentration, Black = Low Concentration)

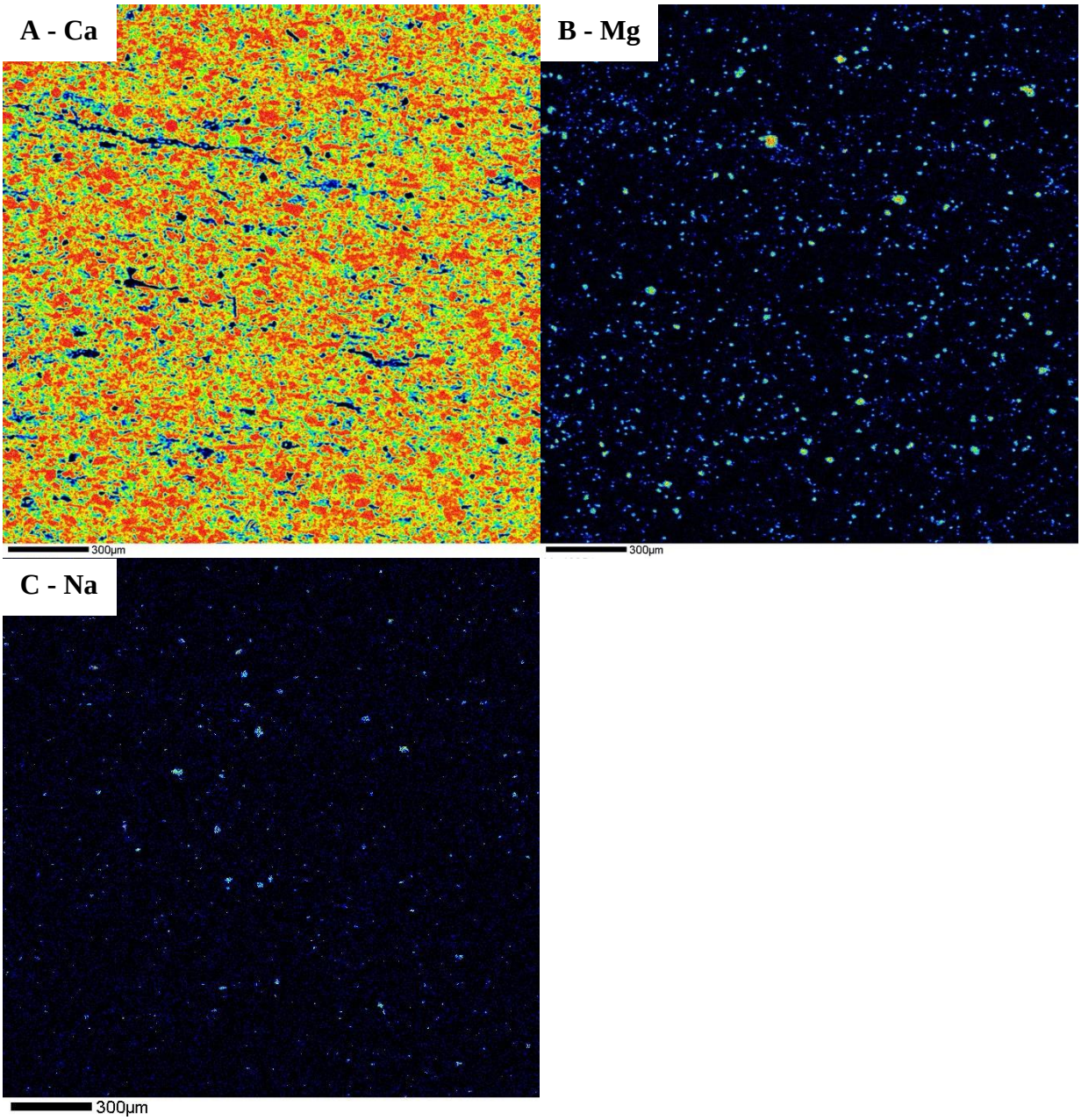

Figure 28 EMP Results of Devonian Shale Hale County – 10354 (Ca, Mg, Na) (Red = High Concentration, Black = Low Concentration)

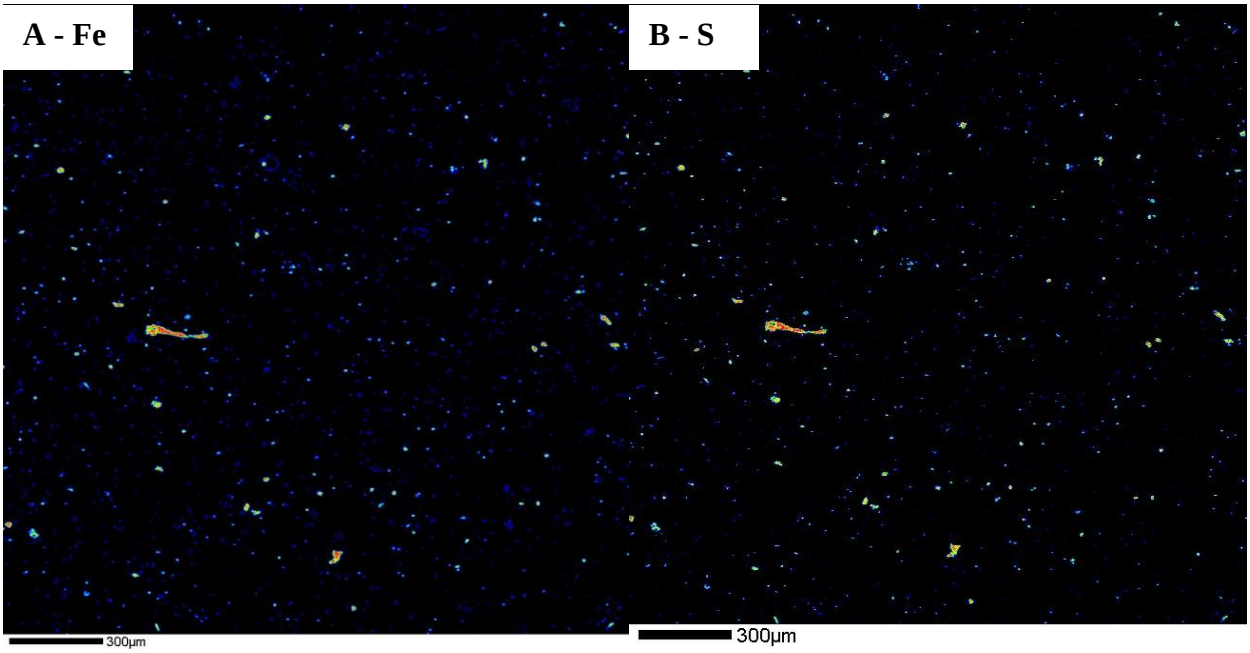

Figure 29 EMP Results of Devonian Shale Hale County – 10354 (Fe, S) (Red = High Concentration, Black = Low Concentration)

ICP-MS Results

ICP-MS provides quantitative multi-element analyses, with higher resolution and sensitivity with respect to XRF data. The ICP-MS results of different geological units are shown in Table 17 and Table 18.

The correlations of selected oxides, elements and minerals are given in Table 19. Total carbonate and clay mineral data are gathered from XRD analysis. There is a strong correlation between Al_2O_3, K_2O, Na_2O, and total clay minerals. Another strong correlation is between CaO and total carbonate mineral data. The increase in Al_2O_3 amount was also associated with various trace element concentrations such as V, Cu, Pb, Ni, Cr, Se, Zn, Be, and Co. By contrast, the increase in CaO concentration was associated with Sr and MgO concentration. Another positive correlation is observed between Fe_2O_3 and As concentration. It is found that the clay-rich and sulfide-rich shale samples were associated with Al, K, Na, V, Cu, Pb, Ni, Cr, Se, Zn, As, Be, and Co while carbonate-rich shale samples were associated with Ca Mg, and Sr.

Table 17 ICP-MS Results (wt%)

Oxide \ Sample Name	Conasauga Shale St. Claire Co. 7558-7558.8 ft.	Devonian Shale Hale Co. 10,354 ft.	Chattanooga Shale Greene Co. 8445-8446 ft.	Neal (Floyd) Shale Pickens Co. 6566-6568 ft.	Conasauga Shale Shelby Co. 14181 ft.
Na_2O	0.11	0.04	0.14	0.21	0.02
MgO	2.04	0.87	1.08	1.23	2.90
Al_2O_3	4.93	0.95	2.68	6.48	0.47
K_2O	1.10	0.29	0.70	1.41	0.13
CaO	11.61	39.21	4.89	1.87	53.86
MnO	0.04	0.02	0.04	0.02	0.01
Fe_2O_3	3.39	1.22	4.12	3.08	0.37

Table 18 ICP-MS Results (mg/kg), converted from the extract concentration obtained from the instrument (μg/L) to dry-weight of sample (mg/kg)

Element \ Sample Name	Conasauga Shale St. Claire Co. 7558-7558.8 ft.	Devonian Shale Hale Co. 10,354 ft.	Chattanooga Shale Greene Co. 8445-8446 ft.	Neal (Floyd) Shale Pickens Co. 6566-6568 ft.	Conasauga Shale Shelby Co. 14181 ft.
Ag	0.30	0.04	0.46	7.86	0.02
Cd	0.25	0.06	0.74	3.14	0.04
Sb	0.18	0.04	0.64	0.77	0.03
Ba	130.44	713.42	328.98	139.18	31.84
Tl	0.38	0.29	1.76	0.48	0.05
Pb	31.02	4.78	23.34	23.65	2.23
Th	2.63	1.14	5.15	5.84	0.44
U	1.24	0.89	11.28	1.75	1.04
V	83.36	21.14	62.01	184.99	5.27
Cr	33.56	6.93	54.08	563.69	3.58
Co	21.85	2.33	15.16	13.24	1.93
Ni	47.04	13.07	94.24	197.61	3.91
Cu	121.88	8.43	69.03	98.86	4.03
Zn	55.81	11.61	116.38	493.73	8.32
As	12.24	1.61	15.93	10.56	1.01
Se	1.62	0.75	5.65	45.43	0.28
Sr	381.54	794.92	159.31	117.75	1349.69
Be	1.05	0.41	1.06	1.39	0.17
Mo	4.61	3.34	40.42	24.32	0.50

Table 19 The correlations of oxides, trace elements and total carbonate and clay minerals.

	Na_2O	***Al_2O3***	***K_2O***	***CaO***	***Fe_2O_3***	***MgO***	***V***	***Cu***	***Pb***	***Ni***	***Cr***	***Se***	***Zn***	***Be***	***Co***	***Sr***	***As***	***Total Carbonates***	***Total Clays***	***TOC***
Na_2O	1.00																			
Al_2O_3	0.90	1.00																		
K_2O	**0.92**	**1.00**	1.00																	
CaO	-0.93	-0.85	-0.88	1.00																
Fe_2O_3	0.80	0.70	0.74	-0.96	1.00															
MgO	-0.46	-0.24	-0.29	0.53	-0.47	1.00														
V	**0.94**	**0.95**	**0.95**	-0.80	0.60	-0.34	1.00													
Cu	0.79	**0.92**	**0.93**	-0.87	0.83	-0.15	0.76	1.00												
Pb	0.78	0.84	0.87	-0.91	**0.92**	-0.23	0.68	**0.98**	1.00											
Ni	**0.96**	0.83	0.84	-0.80	0.62	-0.43	**0.95**	0.62	0.58	1.00										
Cr	0.82	0.77	0.75	-0.56	0.31	-0.29	**0.93**	0.46	0.36	**0.93**	1.00									
Se	0.83	0.76	0.74	-0.57	0.32	-0.31	**0.92**	0.45	0.35	**0.94**	**1.00**	1.00								
Zn	0.88	0.80	0.79	-0.65	0.42	-0.34	**0.94**	0.52	0.44	**0.97**	**0.99**	**0.99**	1.00							
Be	**0.97**	**0.93**	**0.95**	-0.98	0.89	-0.46	0.90	0.90	0.90	0.87	0.69	0.69	0.76	1.00						
Co	0.67	0.77	0.79	-0.84	0.89	-0.13	0.57	**0.96**	**0.99**	0.45	0.22	0.21	0.30	0.81	1.00					
Sr	-0.90	-0.80	-0.84	**0.99**	-0.94	0.66	-0.77	-0.81	-0.86	-0.78	-0.55	-0.55	-0.63	-0.95	-0.77	1.00				
As	0.77	0.66	0.71	-0.92	**0.99**	-0.34	0.56	0.82	**0.91**	0.59	0.27	0.28	0.39	0.85	0.89	-0.88	1.00			
Total Carbonates	-0.95	-0.96	-0.97	**0.91**	-0.75	0.49	-0.96	-0.84	-0.80	-0.90	-0.81	-0.80	-0.84	-0.96	-0.70	0.90	-0.69	1.00		
Total Clays	0.87	**0.91**	**0.93**	-0.86	0.70	-0.59	0.90	0.80	0.76	0.80	0.73	0.72	0.75	**0.91**	0.66	-0.88	0.61	-0.97	1.00	
TOC	**0.92**	0.62	0.65	-0.76	0.60	-0.90	0.80	0.39	0.41	**0.95**	0.80	0.82	0.87	0.79	0.24	-0.78	0.57	-0.78	0.71	1.00

Geochemical Modeling

Reactive Path Modeling – Mineral and Fluid Chemistry Evolution

Geochemist's Workbench was used to investigate the effect of increasing CO_2 fugacity on mineral precipitation and dissolution using various kinetic reaction rates. The models trace the chemical evolution of the system while CO_2 fugacity was slid from 1 to 100 bars in 10 years. Several models were produced by changing the calcite content to understand the effect of calcite in shale-brine-CO_2 interactions. Table 12 shows kinetic rate parameters and Table 13 shows the fluid chemistry of initial conditions used in the models. Mineral contents used in the models (Table 20) are determined by XRD analysis of shale samples.

Figure 30 and Table 21 show the change in pH in response to the increase in CO_2 fugacity. The increase in CO_2 fugacity decreased the pH value to a different extent. The dissolution of calcite serves as the primary pH buffer. A higher calcite content resulted in a higher pH value (4.64) and a lower calcite content resulted in a lower pH value (3.91). Furthermore, a lower calcite content resulted in a rapid decrease in pH and a higher calcite content resulted in a smaller decrease in pH, which can be seen in the first 100 bar fugacity of the model. There is a significant difference in the final pH of models containing 1 vol% and 0.00001 vol% calcite (Figure 30).

The decrease in pH, due to the increase in CO_2 fugacity, driving extensive mineral precipitation and dissolution reaction (Figure 31-Figure 32). The changes in various mineral content are shown in Figure 33-Figure 39. Albite, calcite, chlorite, illite, and k-feldspar were dissolved according to the following reactions:

$$CaCO_3\ (Calcite) + H^+ \rightarrow Ca^{2+} + HCO_3^- \quad (3)$$

$$NaAlSi_3O_8\ (Albite) + 4H^+ \rightarrow 2\ H_2O + Na^+ + Al^{3+} + 3SiO_{2(aq)} \quad (4)$$

$$KAlSi_3O_8\ (K\text{-}feldspar) + 4H^+ \rightarrow 2H_2O + K^+ + Al^{3+} + 3SiO_{2(aq)} \quad (5)$$

$$Mg_5Al_2Si_3O_{10}(OH)_8 \text{ (Chlorite)} + 16H^+ \rightarrow 12H_2O + 5Mg^{2+} + 2Al^{3+} + 3SiO_{2(aq)} \quad (6)$$

$$K_{0.6}Mg_{0.25}Al_{2.3}Si_{3.5}O_{10}(OH)_2 \text{ (Illite)} + 8H^+ \rightarrow 5H_2O + 0.6K^+ + 0.25Mg^{2+} + 2.3Al^{3+} + 3.5SiO_{2(aq)} \quad (7)$$

Dawsonite, illite, and kaolinite were precipitated from increasing Al^{3+}, SiO_2, and HCO_3^- released by dissolution of calcite, silicate, and clay minerals:

$$Na^+ + Al^{3+} + HCO_3^- + 2H_2O \rightarrow NaAlCO_3(OH)_2 \text{ (Dawsonite)} + 3H^+ \quad (8)$$

$$5H_2O + 2Al^{3+} + 2SiO_{2(aq)} \rightarrow Al_2Si_2O_5(OH)_4 \text{ (Kaolinite)} + 6H^+ \quad (9)$$

$$5H_2O + 0.6K^+ + 0.25Mg^{2+} + 2.3Al^{3+} + 3.5SiO_{2(aq)} \rightarrow K_{0.6}Mg_{0.25}Al_{2.3}Si_{3.5}O_{10}(OH)_2 \text{ (Illite)} + 8H^+ \quad (10)$$

Illite tends to dissolve when the calcite content was high. As the calcite volume decreased, illite would re-precipitate after a brief dissolution process (Figure 37). The volume of albite, chlorite and k-feldspar dissolution decreases when there was more calcite to buffer the pH. The volume of dawsonite and kaolinite formed from calcite and silicate minerals dissolution tends to increase with less calcite in the model. The total volume of mineral dissolution is greater than those precipitated (Figure 31), implying that the porosity of shale can be increased via water-rock interaction.

The changes in fluid ion content are shown in Figure 40-Figure 45. There is a significant difference between calcite bearing and calcite lacking model. The calcite-rich model resulted in higher $Ca^{2+,}$ and lower Al^{3+}, K^+, Mg^{2+}, and SiO_2 concentrations in the fluid. Decreasing dissolution of silicate minerals in the calcite-rich system results in less mobilization of Al^{3+}, K^+, and SiO_2. The concentration of Al^{3+} in solution appears to be controlled by the dissolution of albite and k-feldspar and the subsequent precipitation of kaolinite at higher CO_2 fugacity. The final Na^+ concentration in the fluid was not significantly affected by the calcite content and decreased throughout the model as it is used in dawsonite precipitation.

Table 20 Mineralogical composition in the initial geochemical system

Minerals	Volume (vol%)
Quartz	45
Illite	25
K-Feldspar	15
Albite	7
Chlorite	2
Calcite	1, 0.1, 0.01, 0.001, 0.0001, 0.00001, 0.000001, 0
Kaolinite	0
Dawsonite	0
Dolomite	0

Table 21 Final pH values with varying calcite content

Calcite Content (vol%)	Final pH values
1	4.643
0.1	4.643
0.01	4.642
0.001	4.101
0.0001	3.925
0.00001	3.913
0.000001	3.912
0	3.912

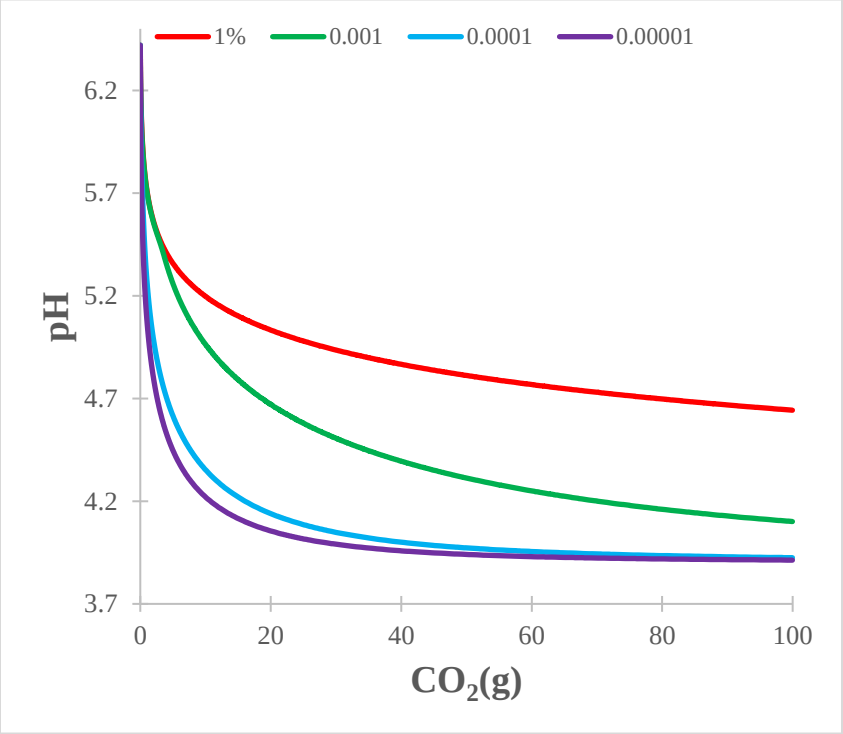

Figure 30 pH changes in response to increasing CO_2 fugacity under different calcite content (red = 1 vol%, green = 0.001 vol%, blue = 0.0001 vol%, purple = 0.00001 vol%)

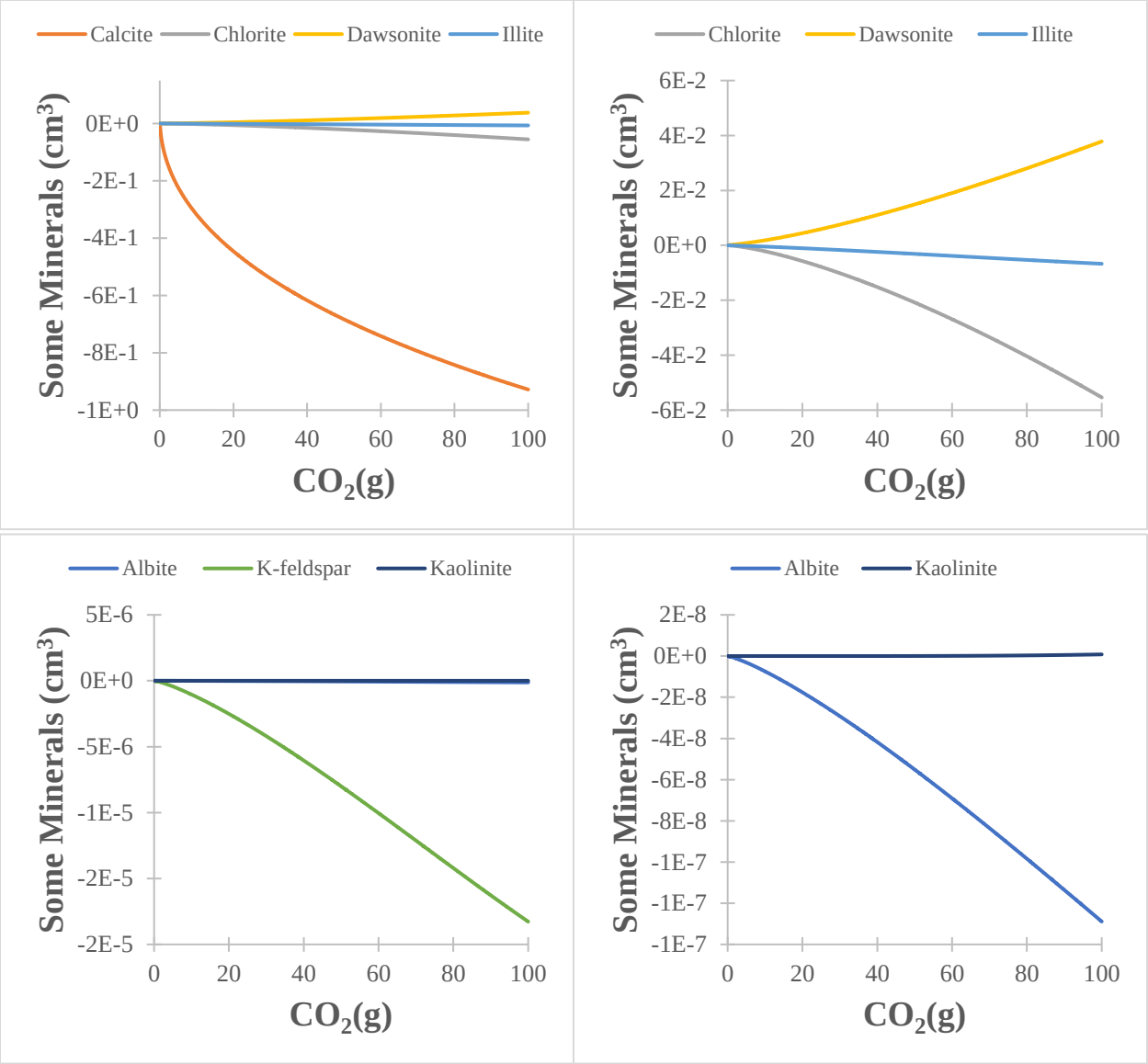

Figure 31 Overall mineral reactions vs CO_2(g). Positive values indicate precipitation and negative values indicate dissolution (1 vol% calcite).

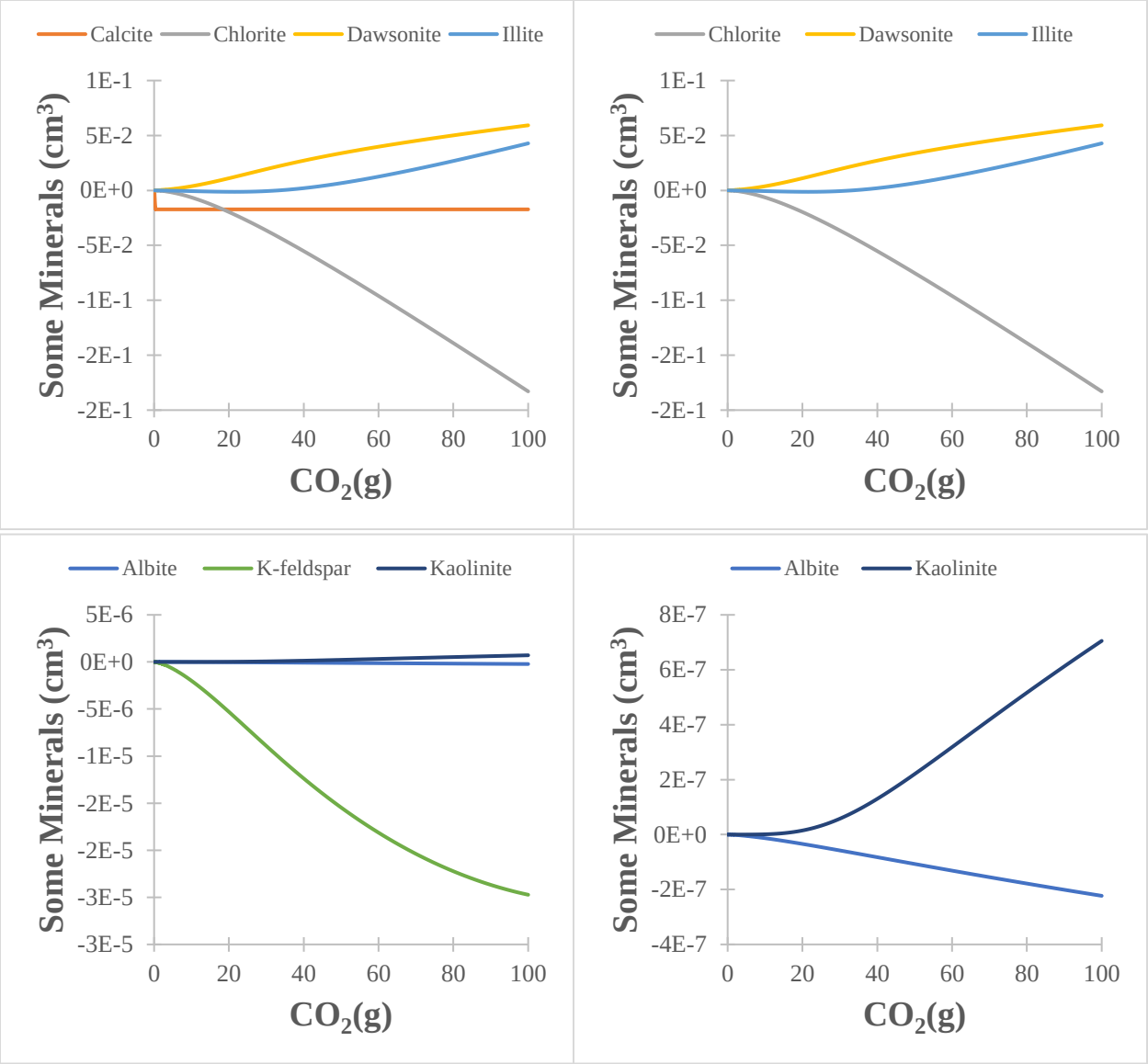

Figure 32 Overall mineral reactions vs CO_2(g). Positive values indicate precipitation and negative values indicate dissolution (0.0001 vol% calcite).

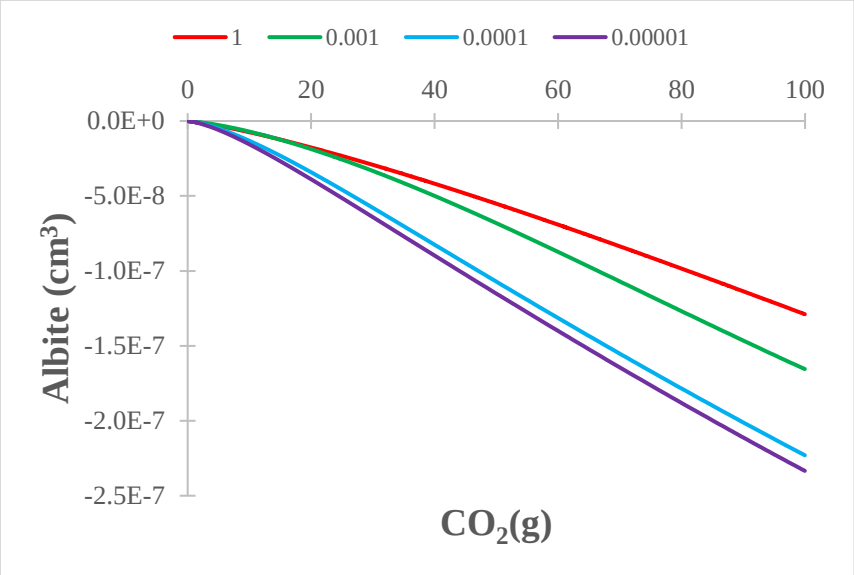

Figure 33 Change in albite volume (cm^3) vs CO_2 under different calcite content (red = 1 vol%, green = 0.001 vol%, blue = 0.0001 vol%, purple = 0.00001 vol%)

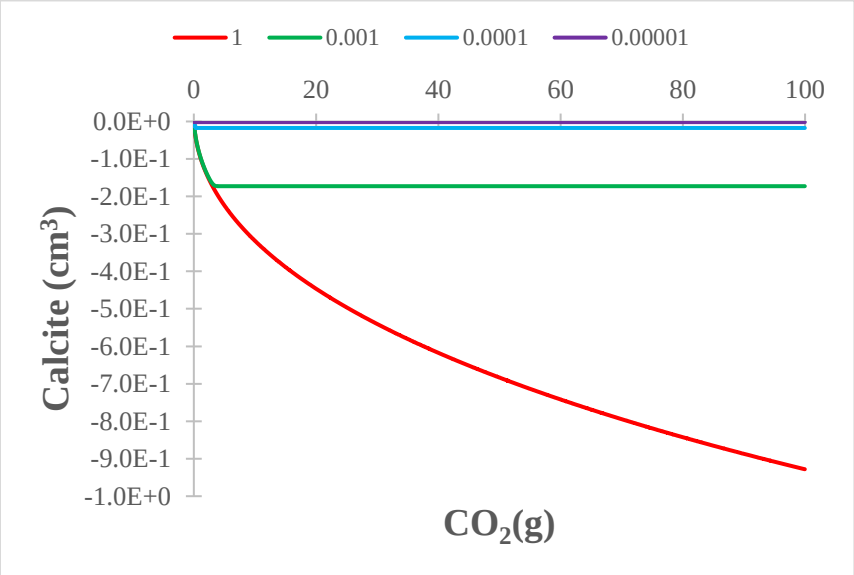

Figure 34 Change in calcite volume (cm^3) vs CO_2 under different calcite content (red = 1 vol%, green = 0.001 vol%, blue = 0.0001 vol%, purple = 0.00001 vol%)

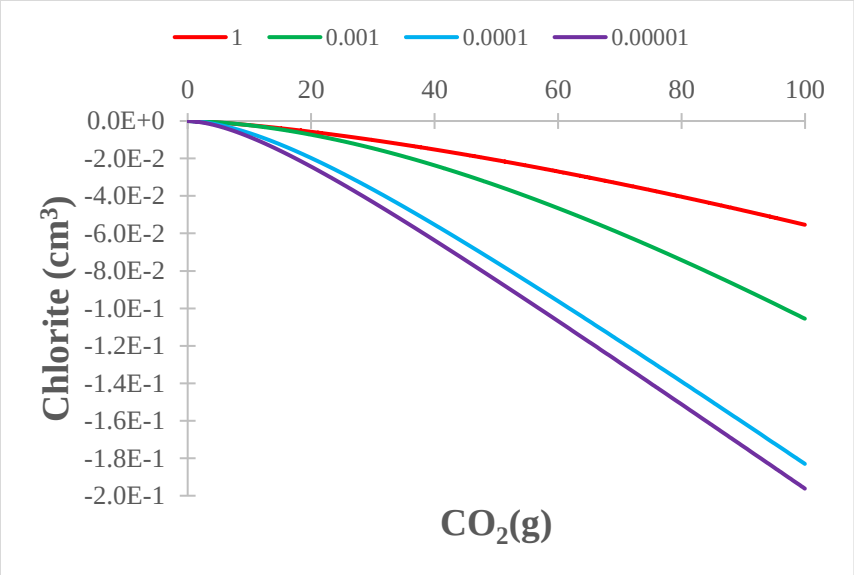

Figure 35 Change in chlorite volume (cm^3) vs CO_2 under different calcite content (red = 1 vol%, green = 0.001 vol%, blue = 0.0001 vol%, purple = 0.00001 vol%)

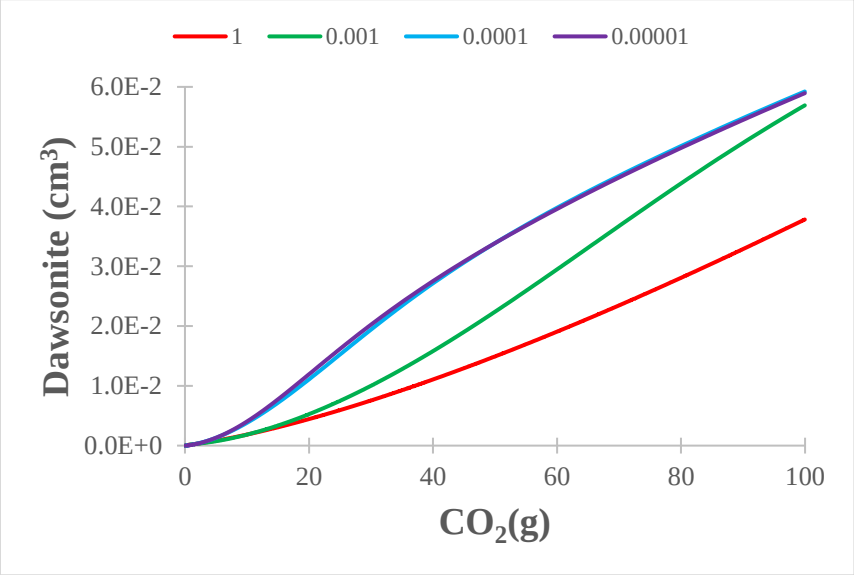

Figure 36 Change in dawsonite volume vs CO_2 under different calcite content (red = 1 vol%, green = 0.001 vol%, blue = 0.0001 vol%, purple = 0.00001 vol%)

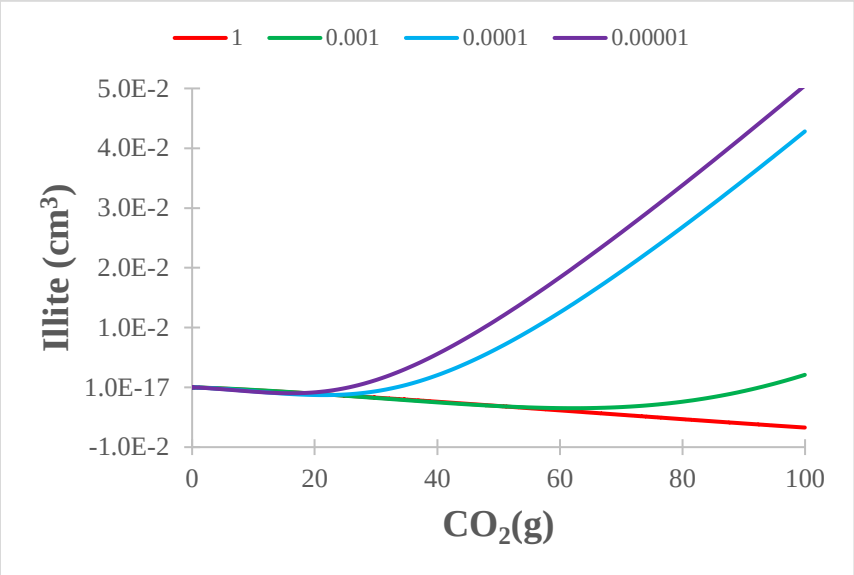

Figure 37 Change in illite volume vs CO_2 under different calcite content (red = 1 vol%, green = 0.001 vol%, blue = 0.0001 vol%, purple = 0.00001 vol%)

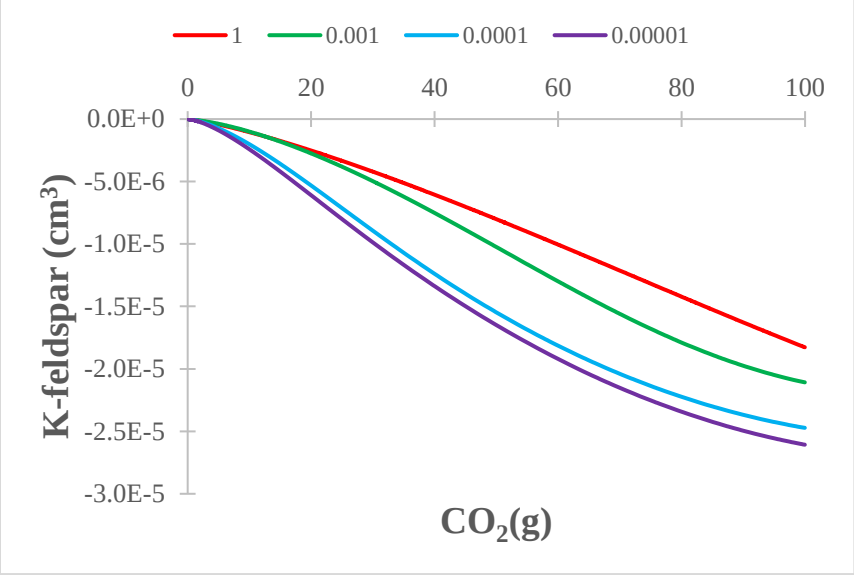

Figure 38 Change in K-feldspar volume vs CO_2 under different calcite content (red = 1 vol%, green = 0.001 vol%, blue = 0.0001 vol%, purple = 0.00001 vol%)

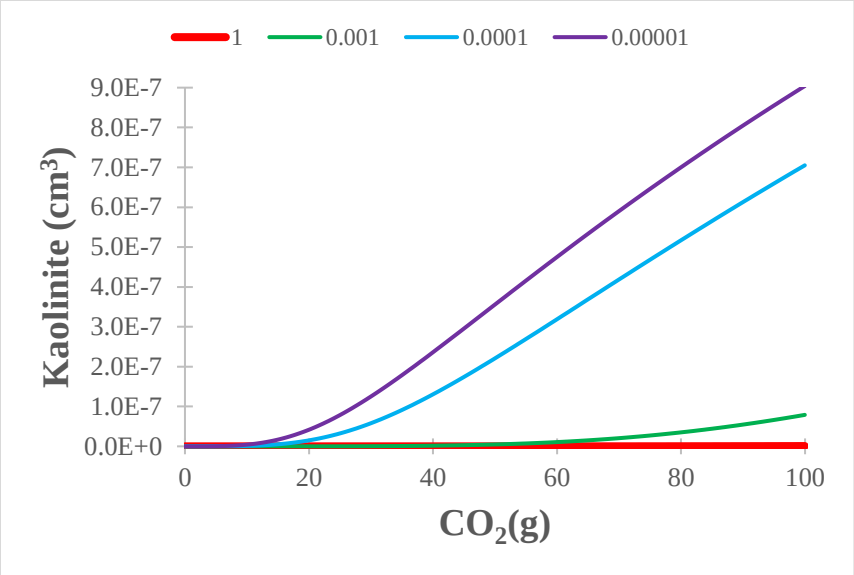

Figure 39 Change in kaolinite volume vs CO_2 under different calcite content (red = 1 vol%, green = 0.001 vol%, blue = 0.0001 vol%, purple = 0.00001 vol%)

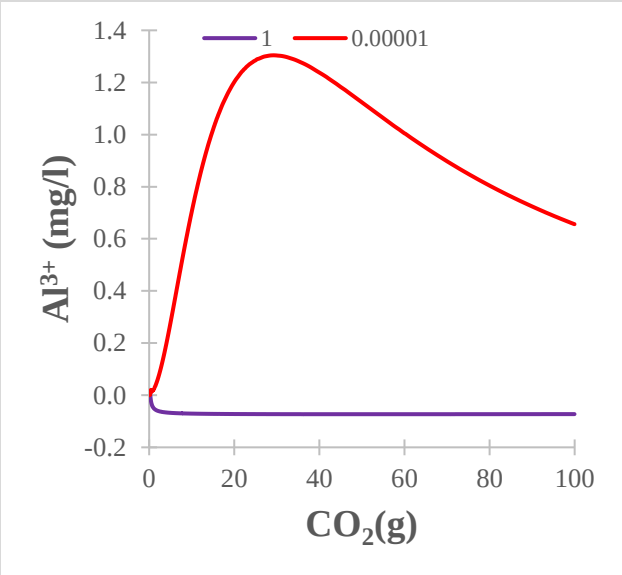

Figure 40 Change in Al^{3+} concentration vs CO_2 fugacity, red = 1 vol% calcite, purple = 0.00001 vol% calcite

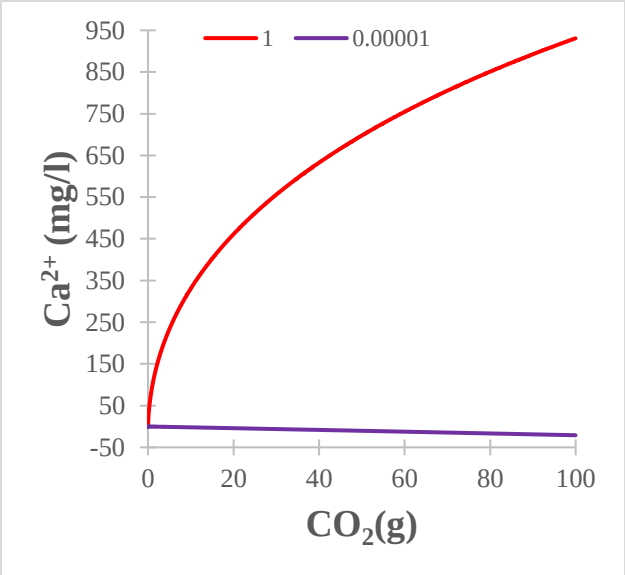

Figure 41 Change in Ca^{2+} concentration vs CO_2 fugacity, red = 1 vol% calcite, purple = 0.00001 vol% calcite

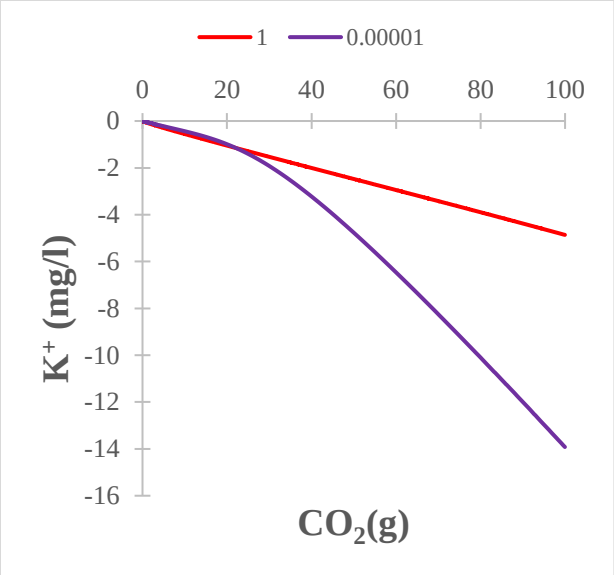

Figure 42 Change in K^+ concentration vs CO_2 fugacity, red = 1 vol% calcite, purple = 0.00001 vol% calcite

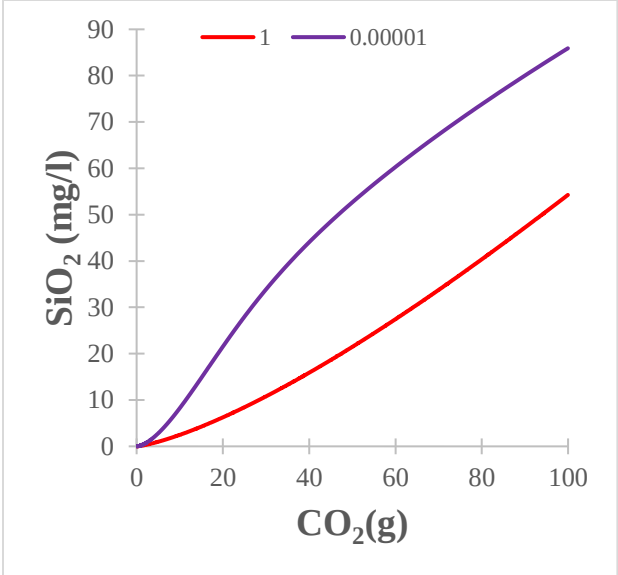

Figure 44 Change in SiO_2 concentration vs CO_2 fugacity, red = 1 vol% calcite, purple = 0.00001 vol% calcite

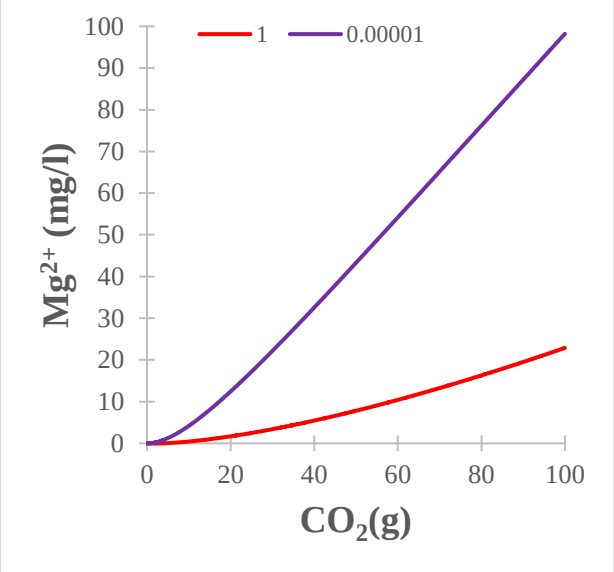

Figure 43 Change in Mg^{2+} concentration vs CO_2 fugacity, red = 1 vol% calcite, purple = 0.00001 vol% calcite

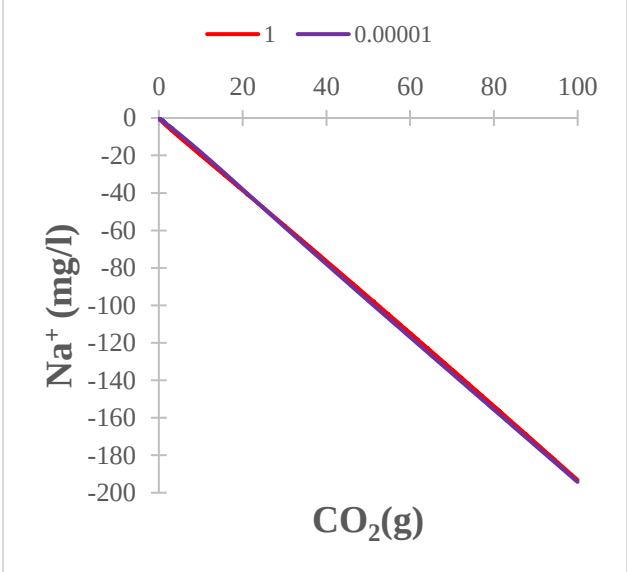

Figure 45 Change in Na^+ concentration vs CO_2 fugacity, red = 1 vol% calcite, purple = 0.00001 vol% calcite

Trace Element Mobilization

The mobilization of several trace elements from their host minerals was simulated to understand the governing mobilization mechanisms associated with shale–brine–CO_2 interaction. The simulations include the sorption of trace elements onto the surfaces of ferric oxide minerals and ion-exchange reactions with illite clay minerals. The surface complexation reactions and equilibrium constants used in the model are shown in Table 10 and Table 11, and fluid chemistry is shown in Table 13. Trace elements included in the model simulations are Co, Ni, Sr, and Zn.

Figure 46-Figure 49 show the changes in trace element concentration resulting from the desorption of trace elements from the surface of $Fe(OH)_3$. As shown in the figures, trace elements Zn^{2+}, $Ni^{2+,}$ and Co^{2+} increased and Sr^{2+} steadily decreased shortly after the CO_2 injection. Calcite-rich systems tend to have less mobilization of trace elements between 0 and 100 bar. There is no significant difference between the final concentration of trace elements at higher CO_2 fugacity.

Figure 51-Figure 54 show the change in trace element concentration resulting from the ion-exchange reactions. Unlike desorption from the surface of $Fe(OH)_3$, ion-exchange reactions were strongly affected by CO_2 fugacity and calcite content. More mobilization of trace elements occurs with increasing calcite dissolution and release of Ca^{2+}, which would compete with trace elements for ion exchange sites provided by clay minerals.

Table 22 shows the changes in trace element concentrations in fluid in $Fe(OH)_3$ sorption and ion-exchange models under various calcite contents. According to the table, the change in trace elements in $Fe(OH)_3$ sorption model was not affected by calcite content, whereas the change in trace elements in ion-exchange model was significantly affected by calcite content. The change in trace elements in $Fe(OH)_3$ sorption model was influenced by pH. Sr^{+2} behaves differently in two mobilization mechanisms. The increasing calcite content significantly affected Sr^{+2} concentration

in ion-exchange model. However, the increase in calcite content did not significantly affect the change in Sr^{+2} concentration in $Fe(OH)_3$ sorption model. The change in Co^{+2} concentration was stable regardless of calcite content in $Fe(OH)_3$ sorption model. On the other hand, the change in Co^{+2} concentration was insignificant when there was less calcite content in ion-exchange model. The change in Co^{+2} concentration in ion-exchange model exceeded (almost 2.6 times) the change in $Fe(OH)_3$ sorption model when the calcite content increased. Although similar increases were observed in the change in Ni^{+2} and Zn^{+2} concentrations in ion-exchange model, the change in Ni^{+2} and Zn^{+2} concentrations in $Fe(OH)_3$ sorption model remained higher. The change in Ni^{+2} concentration was highest and the change in Sr^{+2} concentration was lowest regardless of calcite concentration in $Fe(OH)_3$ sorption model. The change in Sr^{+2} concentration was highest and the change in Zn^{+2} concentration was lowest regardless of calcite content in ion-exchange model.

Table 22 The change in trace elements in fluid due to desorption and cation exchange reactions.

Calcite (vol%)	**Change in trace elements in fluid in $Fe(OH)_3$ sorption model (mg/l)**				**Change in trace elements in fluid in ion-exchange reaction model (mg/l)**			
	Co^{+2}	**Ni^{+2}**	**Sr^{+2}**	**Zn^{+2}**	**Co^{+2}**	**Ni^{+2}**	**Sr^{+2}**	**Zn^{+2}**
0.00001	0.395	2.829	-1.889	1.650	-0.004	-0.045	9.874	-0.108
0.0001	0.394	2.829	-1.889	1.650	0.003	-0.038	10.310	-0.105
0.001	0.394	2.824	-1.894	1.646	0.106	0.067	17.130	0.060
1	0.385	2.729	-1.965	1.622	1.011	1.000	82.500	0.356

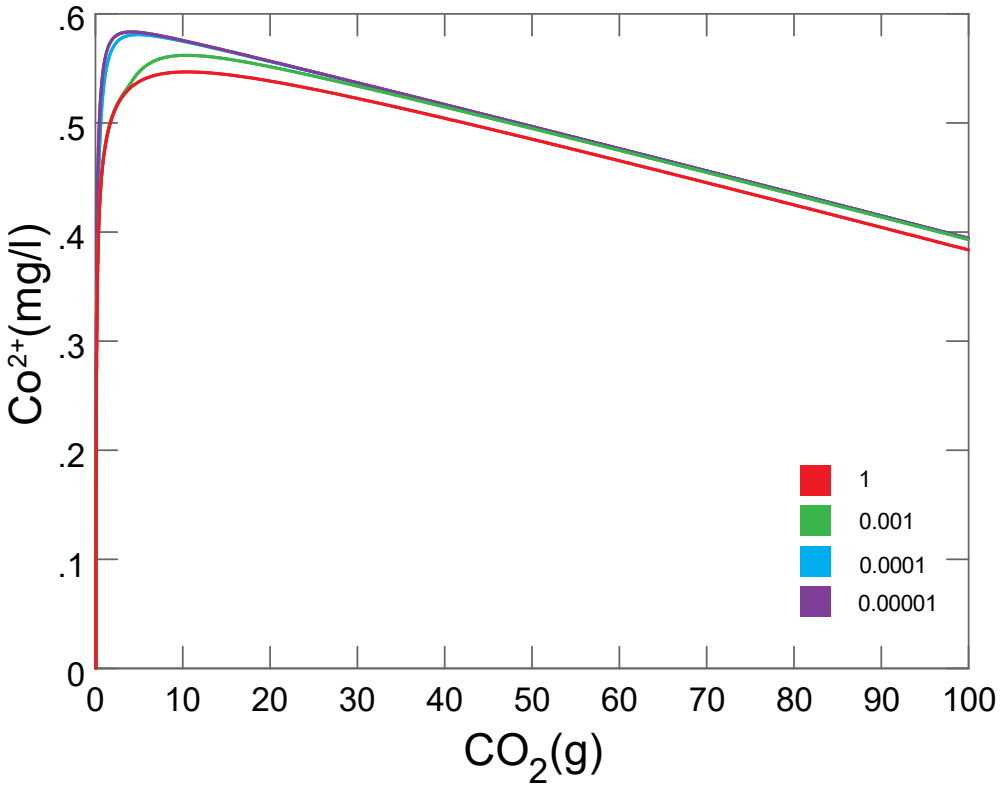

Figure 46 Change in Co^{2+} concentration vs CO_2 fugacity, under different calcite content (red = 1 vol%, green = 0.001 vol%, blue = 0.0001 vol%, purple = 0.00001 vol%), desorption from $Fe(OH)_3$

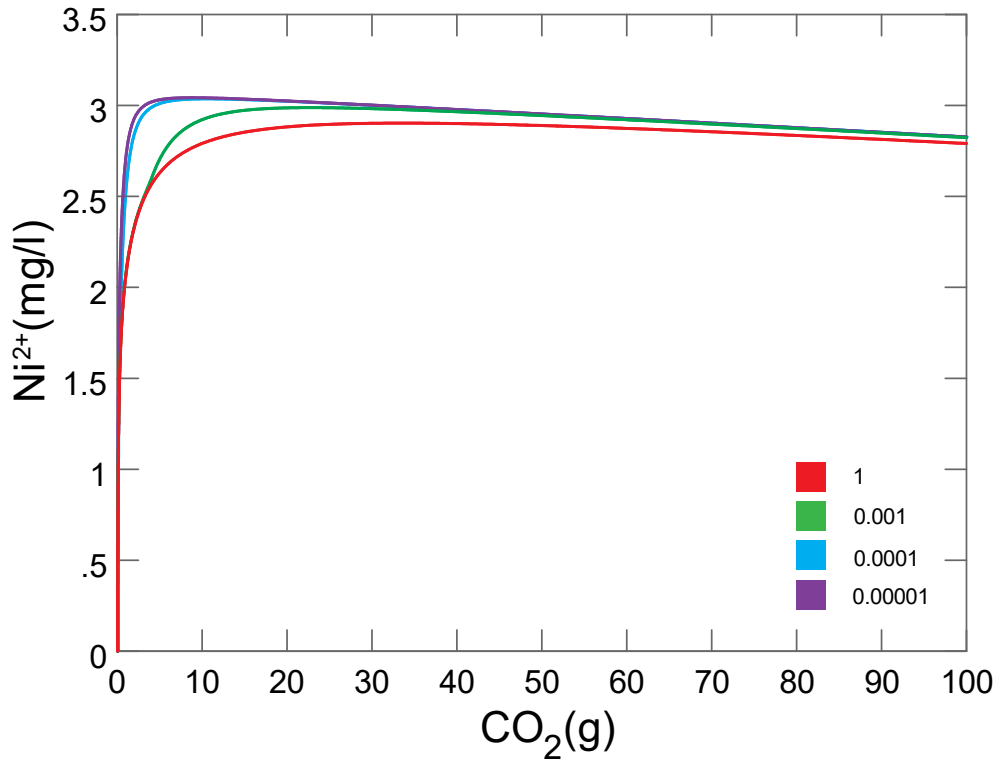

Figure 47 Change in Ni^{2+} concentration vs CO_2 fugacity, under different calcite content (red = 1 vol%, green = 0.001 vol%, blue = 0.0001 vol%, purple = 0.00001 vol%), desorption from $Fe(OH)_3$

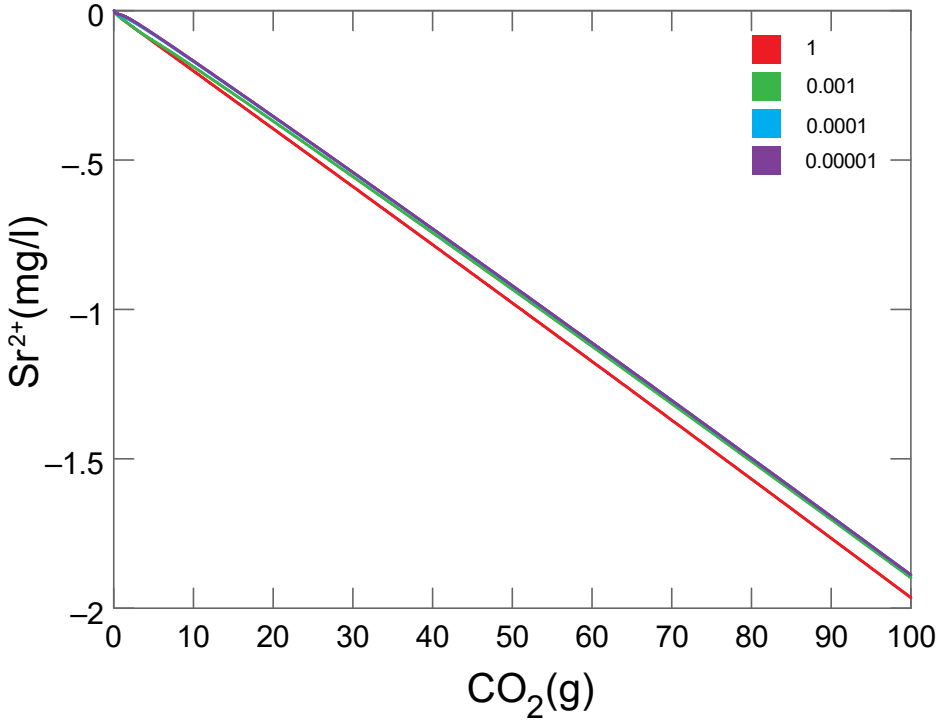

Figure 48 Change in Sr^{2+} concentration vs CO_2 fugacity, under different calcite content (red = 1 vol%, green = 0.001 vol%, blue = 0.0001 vol%, purple = 0.00001 vol%), desorption from $Fe(OH)_3$

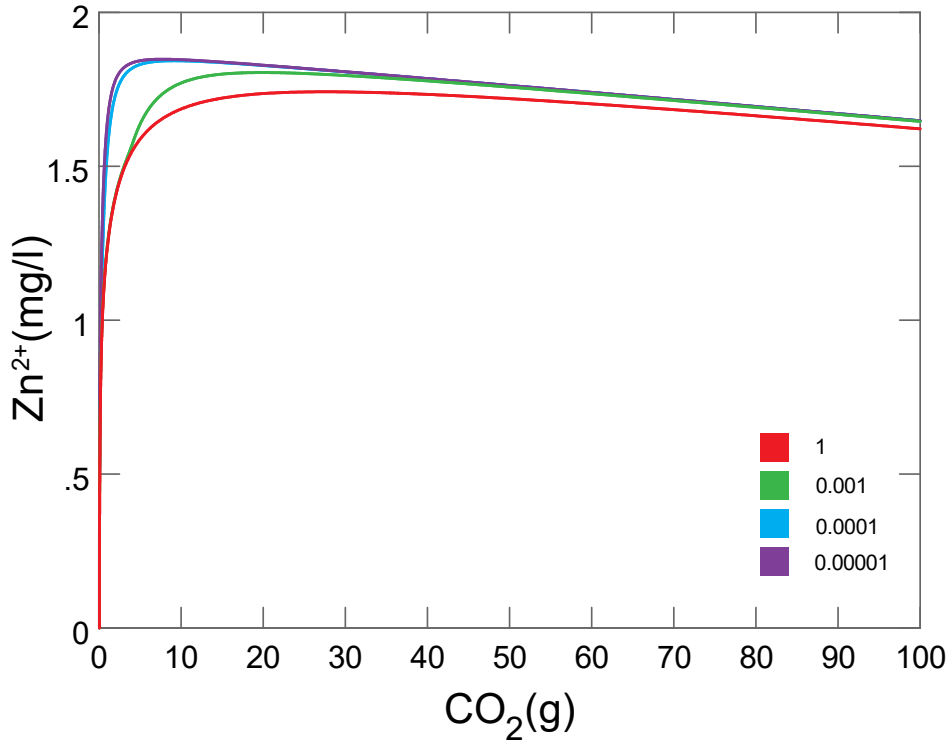

Figure 49 Change in Zn^{2+} concentration vs CO_2 fugacity, under different calcite content (red = 1 vol%, green = 0.001 vol%, blue = 0.0001 vol%, purple = 0.00001 vol%), desorption from $Fe(OH)_3$

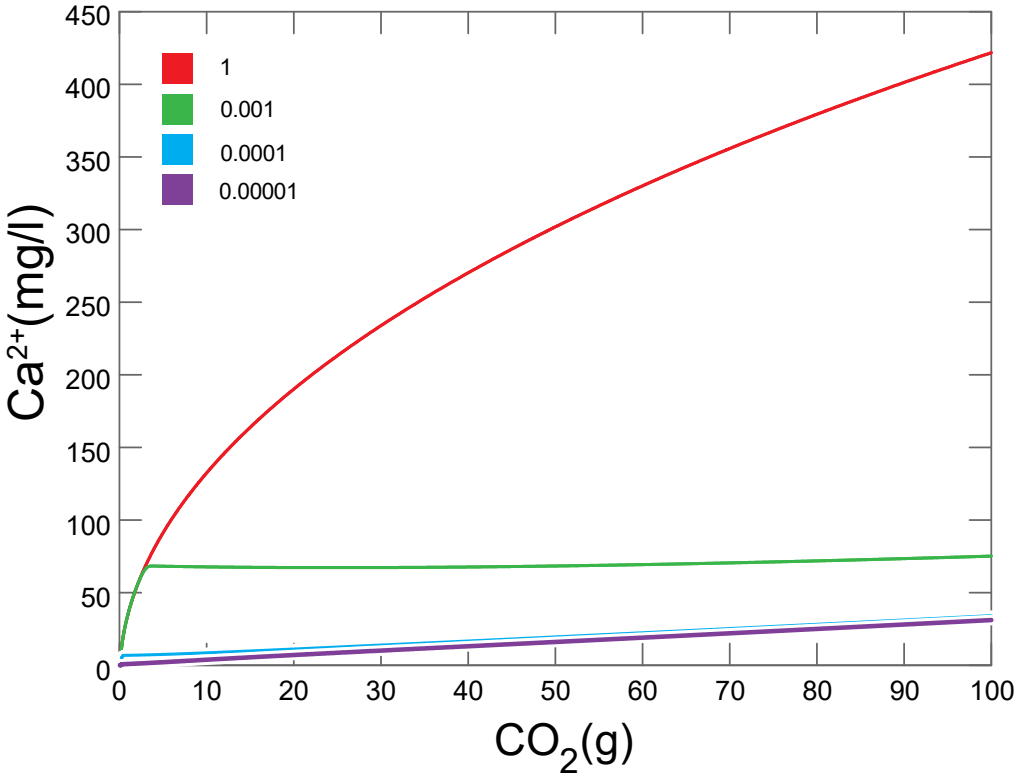

Figure 50 Change in Ca^{2+} concentration vs CO_2 fugacity, under different calcite content (red = 1 vol%, green = 0.001 vol%, blue = 0.0001 vol%, purple = 0.00001 vol%), ion exchange incorporated model

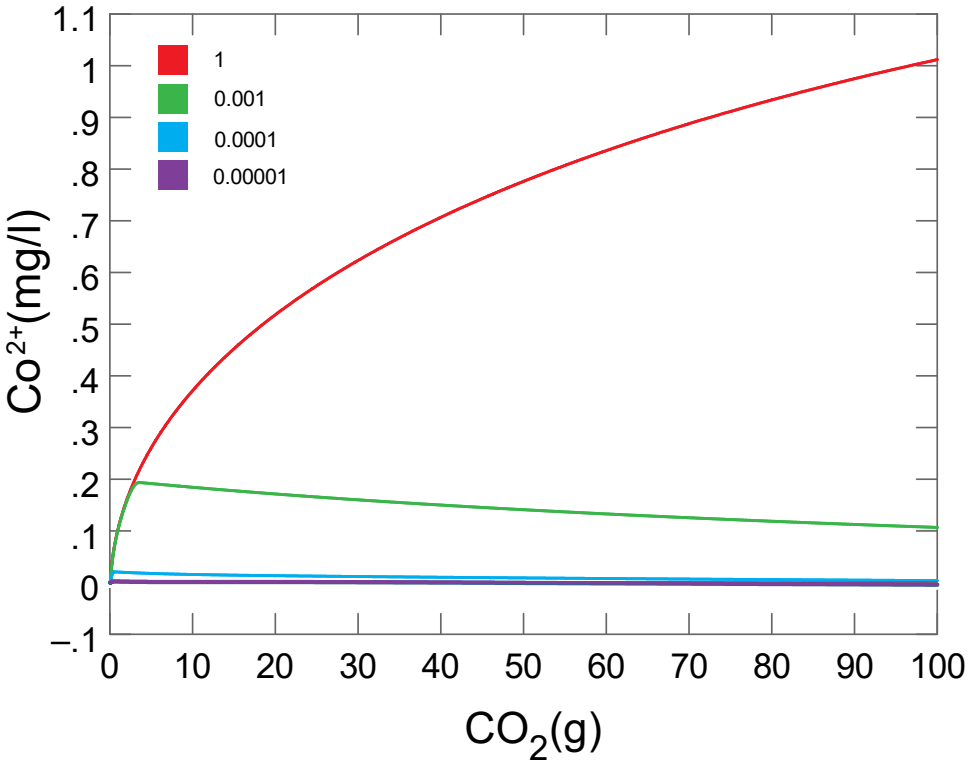

Figure 51 Change in Co^{2+} concentration vs CO_2 fugacity, under different calcite content (red = 1 vol%, green = 0.001 vol%, blue = 0.0001 vol%, purple = 0.00001 vol%), ion exchange incorporated model

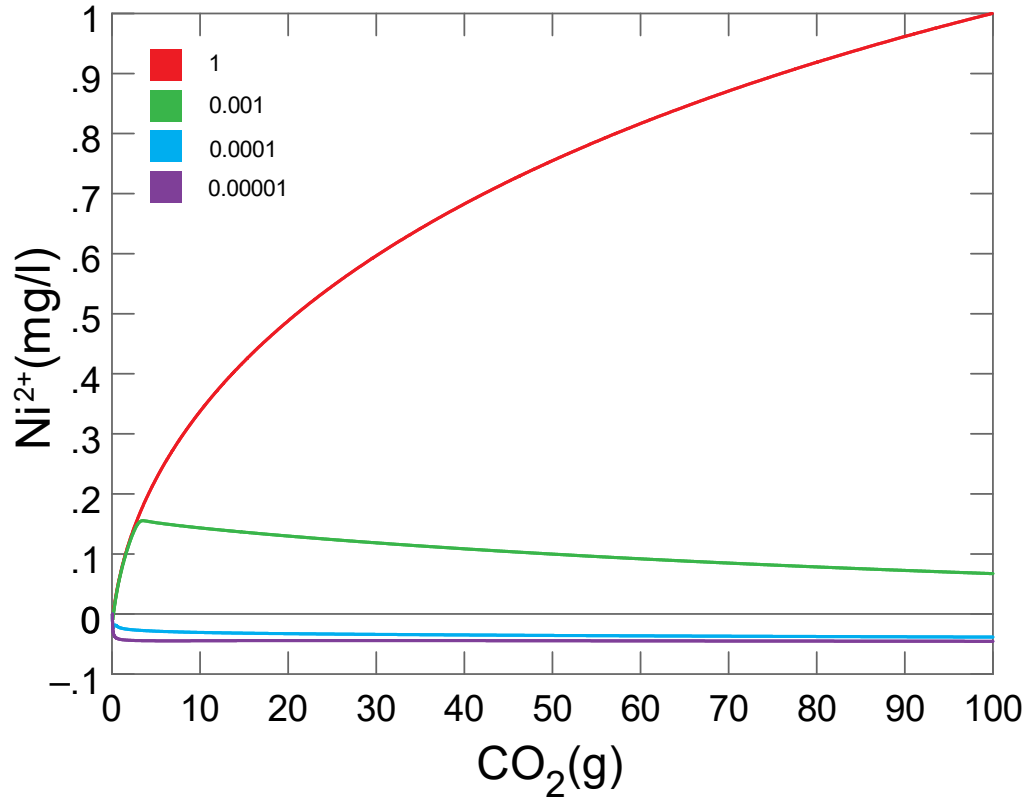

Figure 52 Change in Ni^{2+} concentration vs CO_2 fugacity, under different calcite content (red = 1 vol%, green = 0.001 vol%, blue = 0.0001 vol%, purple = 0.00001 vol%), ion exchange incorporated model

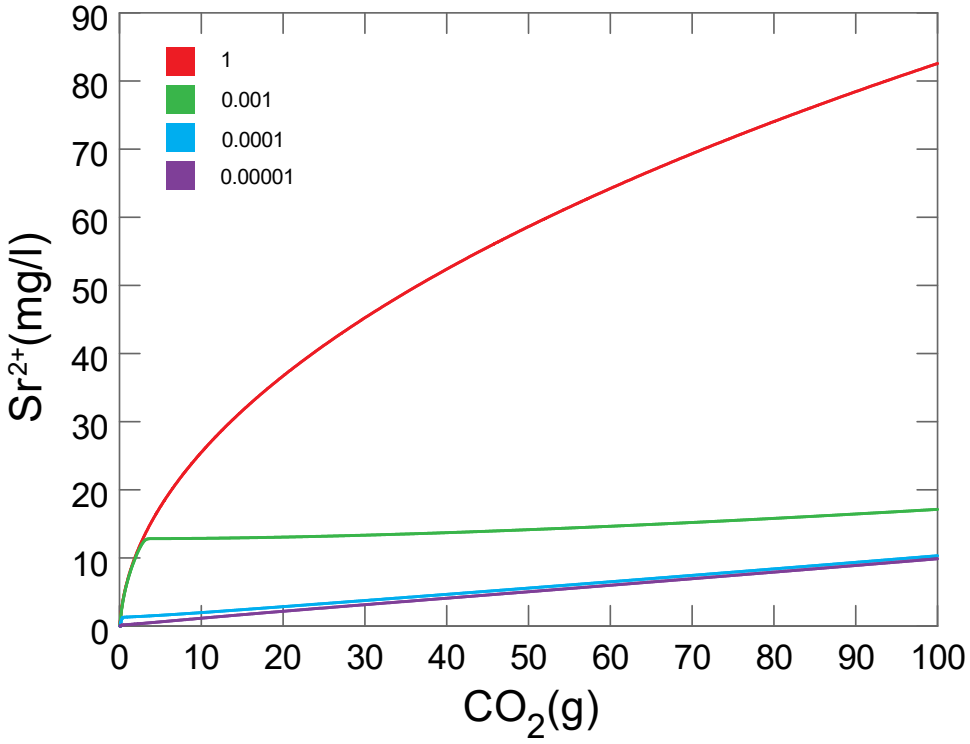

Figure 53 Change in Sr^{2+} concentration vs CO_2 fugacity, under different calcite content (red = 1 vol%, green = 0.001 vol%, blue = 0.0001 vol%, purple = 0.00001 vol%), ion exchange incorporated model

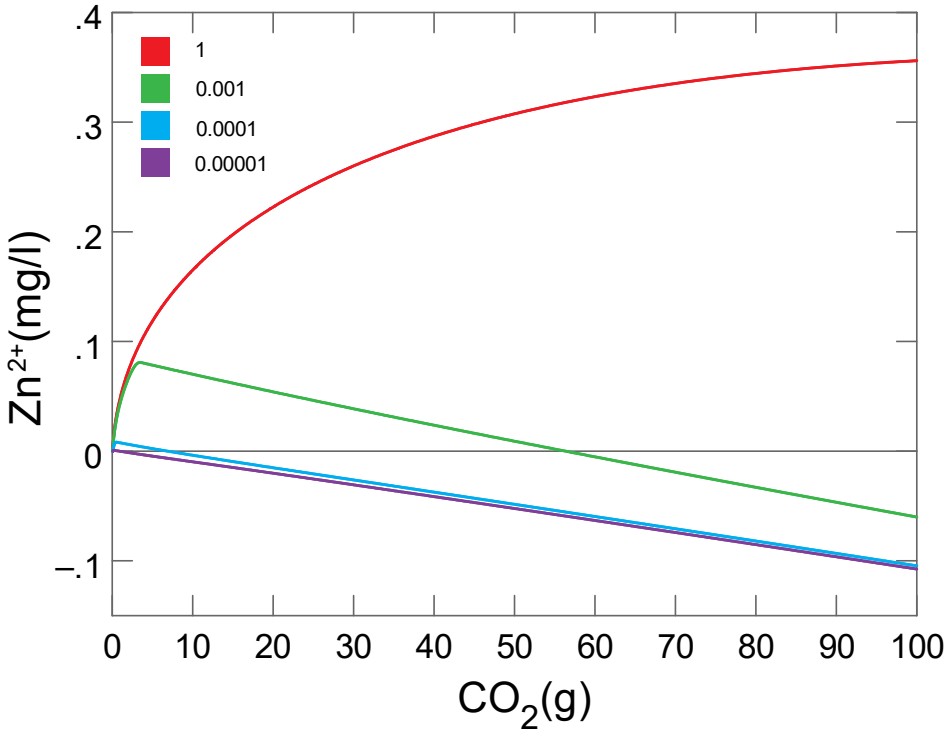

Figure 54 Change in Zn^{2+} concentration vs CO_2 fugacity, under different calcite content (red = 1 vol%, green = 0.001 vol%, blue = 0.0001 vol%, purple = 0.00001 vol%), ion exchange incorporated model

Discussions

Although shale caprocks represent a promising seal in the deep saline aquifer system for carbon sequestration, they contain a significant amount of trace elements that may be mobilized from desorption or ion exchange reactions from their hosts. The XRD results reveal different contents of carbonate (calcite and dolomite), silicate (albite, k-feldspar, kaolinite), clay (illite and chlorite), and sulfide minerals(pyrite) in shales analyzed in this study. XRF, EMP, and ICP-MS analyses confirm the XRD results, revealing the enrichment of Ca and Sr in calcite-bearing shales and relative abundance of Al, Si, K, Ni, Co, and Zn in shales dominated by silicate, clay, and sulfide minerals. The primary result of CO_2 injection is a pH drop as explained by the equation below:

$$CO_{2(aq)} + H_2O \rightarrow HCO_3^- + H^+ \quad (11)$$

The pH drop drives mineral dissolution and precipitation reactions as well as trace element mobilization. Rapid dissolution of calcite was observed with increasing CO_2 fugacity and decreasing pH according to the reaction below;

$$\text{Calcite } (CaCO_3) + H^+ \rightarrow Ca^{2+} + HCO_3^- \quad (12)$$

Calcite thus can buffer the decrease in pH as a result of the CO_2 injection. Higher calcite content resulted in a less drop in pH value, whereas lower calcite value resulted in a greater drop in pH value. Calcite also consumed a large amount of H^+ compared to silicate and clay minerals due to its higher kinetic rate. The dissolution of minerals such as albite, k-feldspar, and chlorite was significantly less when abundant calcite was present to buffer the pH. The precipitation of dawsonite, illite, and kaolinite tends to increase when more silicate and clay minerals dissolve in systems lacking calcite buffering. In the calcite lacking model, more k-feldspar, chlorite and albite dissolution would release more Al^{3+} and SiO_2 according to the following reaction:

$$\text{Chlorite } (Mg_5Al_2Si_3O_{10}(OH)_8) + 16H^+ \rightarrow 12H_2O + 5Mg^{2+} + 2Al^{3+} + 3SiO_{2(aq)} \quad (13)$$

$$\text{Albite } (NaAlSi_3O_8) + 4H^+ \rightarrow 2H_2O + Na^+ + Al^{3+} + 3SiO_{2(aq)} \quad (14)$$

$$\text{K-feldspar } (KAlSi_3O_8) + 4H^+ \rightarrow 2H_2O + K^+ + Al^{3+} + 3SiO_{2(aq)} \quad (15)$$

The geochemical modeling shows that the concentrations of Al^{3+}, K^+, SiO_2 significantly increased in calcite lacking geochemical systems. Silicate and clay minerals, with lower reaction kinetics, may serve as secondary pH buffer in the absence of calcite. The reactions related to the precipitation of dawsonite, kaolinite, and illite are shown below:

$$Na^+ + Al^{3+} + HCO_3^- + 2H_2O \rightarrow \text{Dawsonite } (NaAlCO_3(OH)_2) + 3H^+ \quad (16)$$

$$5H_2O + 2Al^{3+} + 2SiO_{2(aq)} \rightarrow \text{Kaolinite } (Al_2Si_2O_5(OH)_4) + 6H^+ \quad (17)$$

$$5H_2O + 0.6K^+ + 0.25Mg^{2+} + 2.3Al^{3+} + 3.5\ SiO_{2(aq)} \rightarrow \text{Illite } (K_{0.6}Mg_{0.25}Al_{2.3}Si_{3.5}O_{10}(OH)_2) + 8H^+ \quad (18)$$

Illite dissolves right after the CO_2 injection in every scenario, however, it may re-precipitate when there is less calcite in the system. Dawsonite is a carbonate that may precipitate due to increased HCO_3^- and Al^{3+} in the fluid. Although albite is a Na^+ supplier, dawsonite tends to precipitate more than albite dissolved because Na^+ is already abundant in the initial solution.

Mobilization of trace elements also is strongly influenced by the pH and changing ion concentration in the fluid. The $Fe(OH)_3$ sorption model shows a rapid trace element desorption right after the CO_2 injection. The pH drop resulted in the release of trace elements including Zn^{2+}, Ni^{2+}, and Co^{2+}. The final trace element concentration was not significantly affected by calcite content. It was only affected by the change in CO_2 fugacity and pH. Mobilization of trace elements is also significantly affected by ion-exchange reactions with clay minerals (illite) present in shales. The increasing calcite dissolution and Ca^{2+} concentration resulted in significantly more trace element mobilization due to ionic competition on exchanging sites, while lower calcite content and Ca^{2+} concentration resulted in less trace element mobilization.

The behaviors of trace elements under changing pH and ion concentrations are also significant for trace element mobilization. The $Fe(OH)_3$ sorption model shows that Sr^{+2} is not very responsive to the change in pH, whereas ion-exchange model shows that Sr^{+2} is the most responsive to the change in ion concentration. The second most responsive ion to change in ion concentration is Co^{+2}. The change in Co^{+2} concentration in ion-exchange model is less significant when there is less calcite in the model. However, the change in Co^{+2} concentration in ion-exchange model can be up to ~2.6 times the change in Co^{+2} concentration in $Fe(OH)_3$ sorption model when the calcite content is high. The change in Co^{+2} concentration in the $Fe(OH)_3$ model is stable regardless of the calcite content. Other ions such as Ni^{+2} and Zn^{+2} are not as responsive as Sr^{+2} and Co^{+2} to the change in ion concentration. The changes in Ni^{+2} and Zn^{+2} concentration are higher in the $Fe(OH)_3$ model. The change in Ni^{+2} and Zn^{+2} concentration in $Fe(OH)_3$ model is almost ~2.7 times and ~4.5 times in ion-exchange model respectively. The ion-exchange reactions stimulate Sr^{+2} and Co^{+2}, whereas the change in pH stimulates Ni^{+2} and Zn^{+2}.

Conclusions

The thesis represents a study of shale caprock characterization as well as geochemical modeling of shale–brine–CO_2 interaction. Various techniques such as XRD, XRF, EMP, and ICP-MS were used to characterize the mineralogy and bulk geochemistry of several potential shale caprocks in the Black Warrior Basin. A geochemical model was produced to explore mineralogical and elemental change in the fluid and shale caprock due to CO_2 injection.

- The XRD results show various amounts of carbonate, silicate, clay, and sulfide minerals in shale rocks. The XRF and ICP-MS results show that shales with significant silicate, clay, and sulfide minerals were enriched in Al, Si, K, Na, V, Cu, Pb, Ni, Cr, Se, Zn, As, Be, and Co while carbonate-bearing shales were enriched in Ca, Mg, and Sr.

- Geochemical modeling results indicate that carbonates such as calcite readily dissolve, whereas silicate and clay minerals are only of secondary importance in dissolution. Calcite dissolution is the dominant reaction at the beginning of CO_2 injection. The overall shale-brine-CO_2 interaction would result in an increase in shale porosity.

-Geochemical modeling results imply that calcite plays the most significant role in controlling trace element mobilization. A higher calcite content decreased the dissolution of albite, chlorite, k-feldspar, and illite, and the subsequent precipitation of dawsonite and kaolinite. A lower calcite content increased dissolution of albite, chlorite, k-feldspar and increased precipitation of dawsonite, illite, and kaolinite. A lower calcite content resulted in a lower pH at high CO_2 fugacity.

- Geochemical modeling results show that the pH drop results in the desorption of trace elements including Zn^{2+}, Ni^{2+}, and Co^{2+} from the surface of $Fe(OH)_3$. The change in pH was observed to be the main reason behind trace element mobilization. Most of the desorption process occurs at low CO_2 fugacity of 0-100 bar.

- Geochemical modeling shows that trace elements may be mobilized via ion-exchange reactions with clay minerals (illite) present in shales. The increasing calcite content and Ca^{2+} concentration resulted in significantly more trace element mobilization due to ionic competition on exchanging sites.

- Geochemical modeling shows the ion-exchange reactions mobilize Sr^{+2} and Co^{+2} more than Ni^{+2} and Zn^{+2} whereas the desorption reactions release Ni^{+2} and Zn^{+2} more than Sr^{+2} and Co^{+2}. The ion exchange reactions result in higher Sr^{+2} and Co^{+2} concentrations in the water while the change in pH results in higher Ni^{+2} and Zn^{+2} concentrations in water. Therefore, the trace elements considered in the model and their behaviors are significant for shale-brine-CO_2 interaction.

References

A. W. Cleaves, M. C. Broussard, 1980, Chester and Pottsville Depositional Systems, Outcrop and Subsurface, in Black Warrior Basin, Mississippi and Alabama: ABSTRACT: AAPG Bulletin, doi:10.1306/2f9195e9-16ce-11d7-8645000102c1865d.

Abanades, J.C., Rubin, E.S., Mazzotti, M., and Herzog, H.J., 2017, On the climate change mitigation potential of CO2 conversion to fuels: Energy and Environmental Science, doi:10.1039/c7ee02819a.

Abernethy, R., Ackerman, S.A., Adler, R., Albanil Encarnación, A., Aldeco, L.S., Alfaro, E.J., Aliaga-Nestares, V., Allan, R.P., Allan, R., and Alves, L.M., 2018, State of the climate in 2017: Bulletin of the American Meteorological Society, v. 99, p. Si-S310.

Alemu, B.L., Aagaard, P., Munz, I.A., and Skurtveit, E., 2011, Caprock interaction with CO2: A laboratory study of reactivity of shale with supercritical CO2 and brine: Applied Geochemistry, v. 26, p. 1975–1989, doi:10.1016/j.apgeochem.2011.06.028.

Aplin, A.C., Matenaar, I.F., McCarty, D.K., and van der Pluijm, B.A., 2006, Influence of mechanical compaction and clay mineral diagenesis on the microfabric and pore-scale properties of deep-water Gulf of Mexico mudstones: Clays and Clay Minerals, v. 54, p. 500–514, doi:10.1346/CCMN.2006.0540411.

Appelo, C.A.J., Van Der Weiden, M.J.J., Tournassat, C., and Charlet, L., 2002, Surface complexation of ferrous iron and carbonate on ferrihydrite and the mobilization of arsenic: Environmental Science and Technology, doi:10.1021/es010130n.

Apps, J.A., Zheng, L., Zhang, Y., Xu, T., and Birkholzer, J.T., 2010, Evaluation of potential changes in groundwater quality in response to CO2 leakage from deep geologic storage: Transport in Porous Media, v. 82, p. 215–246, doi:10.1007/s11242-009-9509-8.

Armitage, P.J., Faulkner, D.R., Worden, R.H., Aplin, A.C., Butcher, A.R., and Iliffe, J., 2011, Experimental measurement of, and controls on, permeability and permeability anisotropy of caprocks from the CO2 storage project at the Krechba Field, Algeria: Journal of Geophysical Research: Solid Earth, doi:10.1029/2011JB008385.

Assayag, N., Matter, J., Ader, M., Goldberg, D., and Agrinier, P., 2009, Water-rock interactions during a CO2 injection field-test: Implications on host rock dissolution and alteration effects: Chemical Geology, doi:10.1016/j.chemgeo.2009.02.007.

Bachu, S., 2000, Sequestration of CO2 in geological media: Criteria and approach for site selection in response to climate change: Energy Conversion and Management, doi:10.1016/S0196-8904(99)00149-1.

Bachu, S., and Adams, J.J., 2003, Sequestration of CO2 in geological media in response to climate change: Capacity of deep saline aquifers to sequester CO2 in solution: Energy Conversion and Management, v. 44, p. 3151–3175, doi:10.1016/S0196-8904(03)00101-8.

Benson, S.M., and Cole, D.R., 2008, CO2 sequestration in deep sedimentary formations: Elements, v. 4, p. 325–331, doi:10.2113/gselements.4.5.325.

Bethke, C.M., 2007, Geochemical and biogeochemical reaction modeling: Second edition:, doi:10.1017/CBO9780511619670.

Birkholzer, J.T., Zhou, Q., and Tsang, C.F., 2009, Large-scale impact of CO2 storage in deep saline aquifers: A sensitivity study on pressure response in stratified systems: International Journal of Greenhouse Gas Control, doi:10.1016/j.ijggc.2008.08.002.

Boden, T.A., Andres, R.J., and Marland, G., 2017, Global, Regional, and National Fossil-Fuel CO2 Emissions (1751 - 2014):, doi:doi:10.3334/CDIAC/00001_V2017.

Bradbury, M.H., and Baeyens, B., 2000, A generalised sorption model for the concentration dependent uptake of caesium by argillaceous rocks: Journal of Contaminant Hydrology, v. 42, p. 141–163, doi:10.1016/S0169-7722(99)00094-7.

Bradbury, M.H., and Baeyens, B., 2005, Experimental and Modelling Investigations on Na-Illite: Acid-Base Behaviour and the Sorption of Strontium, Nickel, Europium and Uranyl: NAGRA Technical Report, v. 04–02,

http://www.nagra.ch/data/documents/database/dokumente/$default/Default Folder/Publikationen/NTBs 2001-2010/e_ntb04-02.pdf.

Brandt, F., Bosbach, D., Krawczyk-Barsch, E., Arnold, T., and Bernhard, G., 2003, Chlorite dissolution in the acid ph-range: A combined microscopic and macroscopic approach: Geochimica et Cosmochimica Acta, doi:10.1016/S0016-7037(02)01293-0.

Brendler, V., Vahle, A., Arnold, T., Bernhard, G., and Fanghänel, T., 2003, RES3T-Rossendorf expert system for surface and sorption thermodynamics: Journal of contaminant hydrology, v. 61, p. 281–291.

Bui, M. et al., 2018, Carbon capture and storage (CCS): The way forward: Energy and Environmental Science, doi:10.1039/c7ee02342a.

Cahill, A.G., and Jakobsen, R., 2013, Hydro-geochemical impact of CO2 leakage from geological storage on shallow potable aquifers: A field scale pilot experiment: International Journal of Greenhouse Gas Control, v. 19, p. 678–688, doi:10.1016/j.ijggc.2013.03.015.

Cahill, A.G., Marker, P., and Jakobsen, R., 2014, Hydrogeochemical and mineralogical effects of sustained CO2 contamination in a shallow sandy aquifer: A field-scale controlled release experiment: Water Resources Research, doi:10.1002/2013WR014294.

Carroll, R.E., Pashin, J.C., and Kugler, R.L., 1995, Burial History and Source Rock Characteristics of Upper Devonian Through Pennsylvanian Strata, Black Warrior Basin, Alabama: Geolocial Survey of Alabama Circular, p. 30.

Clark, P.E., Pashin, J., Carlson, E., Goodliffe, A., Mcintyre-redden, M., Mann, S.D., Thompson, M., Energy, N., Kluger, K., and Date, R.I., 2013, Site Characterization for CO 2 Storage from Coal-fired Power Facilities in the Black Warrior Basin of Alabama:

Credoz, A., Bildstein, O., Jullien, M., Raynal, J., Pétronin, J.C., Lillo, M., Pozo, C., and Geniaut, G., 2009, Experimental and modeling study of geochemical reactivity between clayey caprocks and CO2 in geological storage conditions: Energy Procedia, v. 1, p. 3445–3452, doi:10.1016/j.egypro.2009.02.135.

Cui, G., Zhang, L., Tan, C., Ren, S., Zhuang, Y., and Enechukwu, C., 2017, Injection of supercritical CO2 for geothermal exploitation from sandstone and carbonate reservoirs: CO2-water-rock interactions and their effects: Journal of CO2 Utilization, doi:10.1016/j.jcou.2017.05.006.

Drever, J.I., 1988, The geochemistry of natural waters: prentice Hall Englewood Cliffs, v. 437.

Duguid, A., and Scherer, G.W., 2010, Degradation of oilwell cement due to exposure to carbonated brine: International Journal of Greenhouse Gas Control, doi:10.1016/j.ijggc.2009.11.001.

Dzombak, D.A., and Morel, F.M.M., 1990, Surface complexation modeling: hydrous ferric oxide: John Wiley & Sons.

EIA, 2017, International Energy Outlook 2017 Overview: U.S. Energy Information Administration,.

EPA, Edition, T., U.S. Environmental Protection Agency, EPA, and Edition, T., 2014, Climate Change Indicators in the United States.:

Espinoza, D.N., and Santamarina, J.C., 2012, Clay interaction with liquid and supercritical CO 2: The relevance of electrical and capillary forces: International Journal of Greenhouse Gas Control, doi:10.1016/j.ijggc.2012.06.020.

Frye, E., Bao, C., Li, L., and Blumsack, S., 2012, Environmental controls of cadmium desorption during CO 2 leakage: Environmental Science and Technology, doi:10.1021/es3005199.

Gilbert, M., and Laudelout, H., 1965, Exchange properties of hydrogen ions in clays: Soil Science, v. 100, p. 157–162.

Guyant, E., Han, W.S., Kim, K.Y., Park, E., and Yun, S.T., 2016, Leakage and pressurization risk assessment of CO2 reservoirs: A metamodeling modeling approach: International Journal of Greenhouse Gas Control, doi:10.1016/j.ijggc.2016.10.004.

Harvey, O.R., Qafoku, N.P., Cantrell, K.J., Lee, G., Amonette, J.E., and Brown, C.F., 2013, Geochemical implications of gas leakage associated with geologic CO 2 storage - A qualitative review: Environmental Science and Technology, v. 47, p. 23–36, doi:10.1021/es3029457.

Hatch, J.R., and Pawlewicz, M.J., 2007, Introduction to the Assessment of Undiscovered Oil and Gas Resources of

the Black Warrior Basin Province of Alabama and Mississippi: Geologic Assessment of Undiscovered Oil and Gas Resources of the Black Warrior Basin Province of Alabama and Mississippi, p. 9 p.

Haynes, C.D., Malone, P.G., and Camp, B.S., 2010, Exploration of the shallow Chattanooga Shale in north central Alabama: Tuscaloosa, *in* Alabama. University of Alabama, college of Continuing Studies, 2010 International coalbed and Gas-shale Symposium proceedings, paper, v. 1015, p. 1–16.

Hellevang, H., Pham, V.T.H., and Aagaard, P., 2013, Kinetic modelling of CO2-water-rock interactions: International Journal of Greenhouse Gas Control, v. 15, p. 3–15, doi:10.1016/j.ijggc.2013.01.027.

Hem, J.D., 1985, Study and interpretation of the chemical characteristics of natural water: Department of the Interior, US Geological Survey, v. 2254.

Heuberger, C.F., Staffell, I., Shah, N., and Mac Dowell, N., 2016, Quantifying the value of CCS for the future electricity system: Energy and Environmental Science, doi:10.1039/c6ee01120a.

Humez, P. et al., 2014, CO2-water-mineral reactions during CO2 leakage: Geochemical and isotopic monitoring of a CO2 injection field test: Chemical Geology, doi:10.1016/j.chemgeo.2014.01.001.

IPCC, 2014, Climate Change 2014 Mitigation of Climate Change:, doi:10.1017/cbo9781107415416.

IPCC, 2005, IPCC special report on carbon dioxide capture and storage. Prepared by working group III of the Intergovernmental Panel on Climate Change, *in* IPCC Special Report on Carbon Dioxide Capture and Storage, doi:10.1002/anie.201000431.

Jean-Baptiste, P., and Ducroux, R., 2003, Energy policy and climate change: Energy policy, v. 31, p. 155–166.

Jones, D.G., Beaubien, S.E., Blackford, J.C., Foekema, E.M., Lions, J., De Vittor, C., West, J.M., Widdicombe, S., Hauton, C., and Queirós, A.M., 2015, Developments since 2005 in understanding potential environmental impacts of CO2 leakage from geological storage: International Journal of Greenhouse Gas Control, doi:10.1016/j.ijggc.2015.05.032.

Jung, H.B., Um, W., and Cantrell, K.J., 2013, Effect of oxygen co-injected with carbon dioxide on Gothic shale caprock-CO2-brine interaction during geologic carbon sequestration: Chemical Geology, v. 354, p. 1–14, doi:10.1016/j.chemgeo.2013.06.019.

Kaszuba, J.P., Janecky, D.R., and Snow, M.G., 2005, Experimental evaluation of mixed fluid reactions between supercritical carbon dioxide and NaCl brine: Relevance to the integrity of a geologic carbon repository: Chemical Geology, v. 217, p. 277–293, doi:10.1016/j.chemgeo.2004.12.014.

Keating, E.H., Fessenden, J., Kanjorski, N., Koning, D.J., and Pawar, R., 2010, The impact of CO2 on shallow groundwater chemistry: Observations at a natural analog site and implications for carbon sequestration: Environmental Earth Sciences, v. 60, p. 521–536, doi:10.1007/s12665-009-0192-4.

Kharaka, Y.K. et al., 2010, Changes in the chemistry of shallow groundwater related to the 2008 injection of CO2 at the ZERT field site, Bozeman, Montana: Environmental Earth Sciences, v. 60, p. 273–284, doi:10.1007/s12665-009-0401-1.

Kidd, J.T., 1975, Pre-Mississippian Subsurface Stratigraphy of Warrior Basin, Alabama: ABSTRACT: AAPG Bulletin, doi:10.1306/83d920a0-16c7-11d7-8645000102c1865d.

Kohler, E., Parra, T., and Vidal, O., 2009, Clayey cap-rock behavior in H2O-CO2 media at low pressure and temperature conditions: An experimental approach: Clays and Clay Minerals, v. 57, p. 616–637, doi:10.1346/CCMN.2009.0570509.

Koide, H., Takahashi, M., Tsukamoto, H., and Shindo, Y., 1995, Self-trapping mechanisms of carbon dioxide in the aquifer disposal: Energy Conversion and Management, v. 36, p. 505–508.

Koide, H., Tazaki, Y., Noguchi, Y., Iijima, M., Ito, K., and Shindo, Y., 1993, Underground storage of carbon dioxide in depleted natural gas reservoirs and in useless aquifers: Engineering Geology, v. 34, p. 175–179, doi:10.1016/0013-7952(93)90086-R.

Lackner, K.S., 2003, A guide to CO2 sequestration: Science, doi:10.1126/science.1079033.

Lee, H., Jang, Y., Jung, W., and Sung, W., 2016, CO2 plume migration with gravitational, viscous, and capillary forces in saline aquifers, *in* International Conference on Offshore Mechanics and Arctic Engineering, American Society of Mechanical Engineers, v. 49996, p. V008T11A001.

Lee, M.K., and Saunders, J.A., 2003, Effects of pH on metals precipitation and sorption: Field bioremediation and geochemical modeling approaches: Vadose Zone Journal, v. 2, p. 177–185, doi:10.2113/2.2.177.

Lemieux, J.M., 2011, Review: The potential impact of underground geological storage of carbon dioxide in deep saline aquifers on shallow groundwater resources: Hydrogeology Journal, doi:10.1007/s10040-011-0715-4.

Little, M.G., and Jackson, R.B., 2010, Potential impacts of leakage from deep CO2 geosequestration on overlying freshwater aquifers: Environmental Science and Technology, doi:10.1021/es102235w.

Little, M.G., and Jackson, R.B., 2011, Response to comment on "potential impacts of leakage from deep CO 2 geosequestration on overlying freshwater aquifers": Environmental Science and Technology, v. 45, p. 3175–3176, doi:10.1021/es200421f.

Lu, J., Partin, J.W., Hovorka, S.D., and Wong, C., 2010, Potential risks to freshwater resources as a result of leakage from CO2 geological storage: A batch-reaction experiment: Environmental Earth Sciences, v. 60, p. 335–348, doi:10.1007/s12665-009-0382-0.

Marcon, V., and Kaszuba, J.P., 2015, Carbon dioxide-brine-rock interactions in a carbonate reservoir capped by shale: Experimental insights regarding the evolution of trace metals: Geochimica et Cosmochimica Acta, v. 168, p. 22–42, doi:10.1016/j.gca.2015.06.037.

Michael, K., Golab, A., Shulakova, V., Ennis-King, J., Allinson, G., Sharma, S., and Aiken, T., 2010, Geological storage of CO2 in saline aquifers-A review of the experience from existing storage operations: International Journal of Greenhouse Gas Control, doi:10.1016/j.ijggc.2009.12.011.

Mickler, P.J., Yang, C., Scanlon, B.R., Reedy, R., and Lu, J., 2013, Potential impacts of CO2 leakage on groundwater chemistry from laboratory batch experiments and field push-pull tests: Environmental Science and Technology, doi:10.1021/es401455j.

Montes-Hernandez, G., Renard, F., and Lafay, R., 2013, Experimental assessment of CO2-mineral-toxic ion interactions in a simplified freshwater aquifer: Implications for CO2 leakage from deep geological storage: Environmental Science and Technology, doi:10.1021/es3053448.

Montoya, V., Baeyens, B., Glaus, M.A., Kupcik, T., Marques Fernandes, M., Van Laer, L., Bruggeman, C., Maes, N., and Schäfer, T., 2018, Sorption of Sr, Co and Zn on illite: Batch experiments and modelling including Co in-diffusion measurements on compacted samples: Geochimica et Cosmochimica Acta, doi:10.1016/j.gca.2017.11.027.

Niu, B., Al-Menhali, A., and Krevor, S., 2014, A study of residual carbon dioxide trapping in sandstone, *in* Energy Procedia, doi:10.1016/j.egypro.2014.11.585.

Office of Ground Water and Drinking Water, 2009, National Primary Drinking Water Guidelines: v. 1, p. 7, https://www.epa.gov/sites/production/files/2016-06/documents/npwdr_complete_table.pdf.

Orr, F.M., 2009, Onshore geologic storage of CO2: Science, doi:10.1126/science.1175677.

Palandri, J.L., and Kharaka, Y.K., 2004, A compilation of rate parameters of water-mineral interaction kinetics for application to geochemical modeling: USGS Open File Report, v. 2004–1068, p. 71, doi:10.1098/rspb.2004.2754.

Pashin, J.C., 1994, Cycles and stacking patterns in Carboniferous rocks of the Black Warrior foreland basin:

Pashin, J.C., 2004, Cyclothems of the Black Warrior basin in Alabama: Eustatic snapshots of foreland basin tectonism: American Association of Petroleum Geologists Studies in Geology 51:

Pashin, J.C., 2008, Gas shale potential of Alabama, *in* Univ Alabama, 2008 Int Coalbed Shale Gas Symposium Proc, Paper, v. 808.

Pashin, J.C., 2009, Shale gas plays of the southern Appalachian thrust belt, *in* International Coalbed Shale Gas Symposium, v. 9, p. 1–14.

Pashin, J.C., 1993, Tectonics, paleoceanography, and paleoclimate of the Kaskaskia sequence in the Black Warrior basin of Alabama:

Pashin, J.C., Grace, R.L.B., and Kopaska-Merkel, D.C., 2010, Devonian Shale Plays in the Black Warrior Basin and Appalachian Thrust Belt of Alabama: Coalbed and Shale Gas Symposium,.

Pashin, J.C., Kopaska-Merkel, D.C., Arnold, A.C., McIntyre, M.R., and Thomas, W.A., 2012, Gigantic, gaseous mushwads in Cambrian shale: Conasauga Formation, southern Appalachians, USA: International Journal of Coal Geology, v. 103, p. 70–91, doi:10.1016/j.coal.2012.05.010.

Patil, V. V., 2016, Self-sealing of faults in geological carbon sequestration:

Perkins, E.H., Gunter, W.D., Nesbtt, H.W., and St-Arnaud, L.C., 1997, Critical review of classes of geochemical computer models adaptable for prediction of acidic drainage from mine waste rock: Fourth International Conference on Acid Rock Drainage, p. 587–601, doi:Report 1.42.1.

Peter, A. et al., 2012, Investigation of the geochemical impact of CO2 on shallow groundwater: Design and implementation of a CO2 injection test in Northeast Germany: Environmental Earth Sciences, doi:10.1007/s12665-012-1700-5.

Qafoku, N.P., Lawter, A.R., Bacon, D.H., Zheng, L., Kyle, J., and Brown, C.F., 2017, Review of the impacts of leaking CO2 gas and brine on groundwater quality: Earth-Science Reviews, v. 169, p. 69–84, doi:10.1016/j.earscirev.2017.04.010.

Reed, S.J.B., 2005, Electron microprobe analysis and scanning electron microscopy in geology:, doi:10.1017/CBO9780511610561.

Rempel, K.U., Liebscher, A., Heinrich, W., and Schettler, G., 2011, An experimental investigation of trace element dissolution in carbon dioxide: Applications to the geological storage of CO2: Chemical Geology, v. 289, p. 224–234, doi:10.1016/j.chemgeo.2011.08.003.

Rillard, J., Gombert, P., Toulhoat, P., and Zuddas, P., 2014, Geochemical assessment of CO2 perturbation in a shallow aquifer evaluated by a push-pull field experiment: International Journal of Greenhouse Gas Control, doi:10.1016/j.ijggc.2013.11.019.

Shao, H., Freiburg, J.T., Berger, P.M., Taylor, A.H., Cohen, H.F., and Locke, R.A., 2020, Mobilization of trace metals from caprock and formation rocks at the Illinois Basin – Decatur Project demonstration site under geological carbon dioxide sequestration conditions: Chemical Geology, doi:10.1016/j.chemgeo.2020.119758.

Shao, H., Kukkadapu, R.K., Krogstad, E.J., Newburn, M.K., and Cantrell, K.J., 2014, Mobilization of metals from Eau Claire siltstone and the impact of oxygen under geological carbon dioxide sequestration conditions: Geochimica et Cosmochimica Acta, v. 141, p. 62–82, doi:10.1016/j.gca.2014.06.011.

Sharifzadeh, M., Triulzi, G., and Magee, C.L., 2019, Quantification of technological progress in greenhouse gas (GHG) capture and mitigation using patent data: Energy and Environmental Science, doi:10.1039/c9ee01526d.

Sharma, S.S., 2011, Determinants of carbon dioxide emissions: Empirical evidence from 69 countries: Applied Energy, doi:10.1016/j.apenergy.2010.07.022.

Shukla, R., Ranjith, P., Haque, A., and Choi, X., 2010, Review article A review of studies on CO 2 sequestration and caprock integrity: Fuel, v. 89, p. 2651–2664, doi:10.1016/j.fuel.2010.05.012.

Song, J., and Zhang, D., 2013, Comprehensive Review of Caprock-Sealing Mechanisms for Geologic Carbon Sequestration:, doi:10.1021/es301610p.

Strandli, C.W., and Benson, S.M., 2013, Identifying diagnostics for reservoir structure and CO2 plume migration from multilevel pressure measurements: Water Resources Research, doi:10.1002/wrcr.20285.

Stumm, W., 1992, Chemistry of the solid-water interface: processes at the mineral- water and particle-water interface in natural systems: Chemistry of the solid-water interface: processes at the mineral- water and particle-water interface in natural systems, doi:10.1016/0016-7037(93)90027-t.

Tang, Y., Lv, C., Wang, R., and Cui, M., 2016, Mineral dissolution and mobilization during CO2 injection into the water-flooded layer of the Pucheng Oilfield, China: Journal of Natural Gas Science and Engineering, v. 33, p. 1364–1373, doi:10.1016/j.jngse.2016.06.073.

Thomas, W.A., 1974, Converging clastic wedges in the Mississippian of Alabama: Special Paper of the Geological Society of America, doi:10.1130/SPE148-p187.

Thomas, W.A., 1972, Mississippian stratigraphy of Alabama: Geological Survey of Alabama,.

Thomas, W.A., 2001, Mushwad: Ductile duplex in the appalachian thrust belt in Alabama: AAPG Bulletin,.

Thomas, W.A., and Bayona, G., 2005, The Appalachian thrust belt in Alabama and Georgia: thrust-belt structure, basement structure, and palinspastic reconstruction: Alabama Geological Society.

Trautz, R.C. et al., 2013, Effect of dissolved CO2 on a shallow groundwater system: A controlled release field experiment: Environmental Science and Technology, v. 47, p. 298–305, doi:10.1021/es301280t.

Uddin, A., Hames, W.E., Peavy, T., and Pashin, J.C., 2016, Detrital History of the Lower Pennsylvanian Pottsville Formation In the Cahaba Synclinorium of Alabama, U.S.A.: Journal of Sedimentary Research, doi:10.2110/jsr.2016.76.

US Geological Survey, 2015, US Brine Wells:, https://edx.netl.doe.gov/dataset/us-brine-wells-.

Varadharajan, C., Tinnacher, R.M., Pugh, J.D., Trautz, R.C., Zheng, L., Spycher, N.F., Birkholzer, J.T., Castillo-Michel, H., Esposito, R.A., and Nico, P.S., 2013, A laboratory study of the initial effects of dissolved carbon dioxide (CO2) on metal release from shallow sediments: International Journal of Greenhouse Gas Control, doi:10.1016/j.ijggc.2013.08.017.

De Viguerie, L., Sole, V.A., and Walter, P., 2009, Multilayers quantitative X-ray fluorescence analysis applied to easel paintings: Analytical and Bioanalytical Chemistry, v. 395, p. 2015–2020, doi:10.1007/s00216-009-2997-0.

Wang, S., and Jaffe, P.R., 2004, Dissolution of a mineral phase in potable aquifers due to CO2 releases from deep formations; Effect of dissolution kinetics: Energy Conversion and Management, doi:10.1016/j.enconman.2004.01.002.

Wedepohl, K.H., 1995, The composition of the continental crust: Geochimica et cosmochimica Acta, v. 59, p. 1217–1232.

WHO, 2008, Guidelines for Drinking-water Quality: World Health Organization,.

Wilson, G. V, 1982, Characteristics of Tar Sands of Alabama, *in* National Tar Sands (Heavy Oil) Symposium, sponsored by Kentucky Geological Survey and University of Kentucky, Lexington, Kentucky, p. 10–11.

Xiao, T., Dai, Z., McPherson, B., Viswanathan, H., and Jia, W., 2017, Reactive transport modeling of arsenic mobilization in shallow groundwater: impacts of CO 2 and brine leakage: Geomechanics and Geophysics for Geo-Energy and Geo-Resources, v. 3, p. 339–350, doi:10.1007/s40948-017-0058-2.

Xiao, T., McPherson, B., Pan, F., Esser, R., Jia, W., Bordelon, A., and Bacon, D., 2016, Potential chemical impacts of CO2 leakage on underground source of drinking water assessed by quantitative risk analysis: International Journal of Greenhouse Gas Control, doi:10.1016/j.ijggc.2016.04.009.

Xu, T., Kharaka, Y.K., Doughty, C., Freifeld, B.M., and Daley, T.M., 2010, Reactive transport modeling to study changes in water chemistry induced by CO2 injection at the Frio-I Brine Pilot: Chemical Geology, v. 271, p. 153–164, doi:10.1016/j.chemgeo.2010.01.006.

Yamasaki, A., 2003, An overview of CO2 mitigation options for global warming - Emphasizing CO2 sequestration options: Journal of Chemical Engineering of Japan, doi:10.1252/jcej.36.361.

Yang, C., Mickler, P.J., Reedy, R., Scanlon, B.R., Romanak, K.D., Nicot, J.P., Hovorka, S.D., Trevino, R.H., and Larson, T., 2013, Single-well push-pull test for assessing potential impacts of CO2 leakage on groundwater quality in a shallow Gulf Coast aquifer in Cranfield, Mississippi: International Journal of Greenhouse Gas Control, doi:10.1016/j.ijggc.2012.12.030.

Yang, Z., Xu, T., Wang, F., Yang, Y., Li, X., and Zhao, N., 2018, Impact of inner reservoir faults on migration and storage of injected CO2: International Journal of Greenhouse Gas Control, doi:10.1016/j.ijggc.2018.03.006.

Zheng, L., Apps, J.A., Zhang, Y., Xu, T., and Birkholzer, J.T., 2009, On mobilization of lead and arsenic in groundwater in response to CO2 leakage from deep geological storage: Chemical Geology, v. 268, p. 281–297, doi:10.1016/j.chemgeo.2009.09.007.

Zheng, L., Qafoku, N.P., Lawter, A., Wang, G., Shao, H., and Brown, C.F., 2016a, Evaluating impacts of CO 2 intrusion into an unconsolidated aquifer: II. Modeling results: International Journal of Greenhouse Gas Control, v. 44, p. 300–309, doi:10.1016/j.ijggc.2015.07.001.

Zheng, L., and Spycher, N., 2018, Modeling the potential impacts of CO2 sequestration on shallow groundwater: The fate of trace metals and organic compounds before and after leakage stops: Greenhouse Gases: Science and

Technology, v. 8, p. 161–184, doi:10.1002/ghg.1728.

Zheng, L., Spycher, N., Bianchi, M., Pugh, J.D., Varadharajan, C., Tinnacher, R.M., Birkholzer, J.T., Nico, P., and Trautz, R.C., 2016b, Impacts of elevated dissolved CO2 on a shallow groundwater system: Reactive transport modeling of a controlled-release field test: Chemical Geology, doi:10.1016/j.chemgeo.2016.10.027.

Zheng, L., Spycher, N., Birkholzer, J., Xu, T., Apps, J., and Kharaka, Y., 2013, On modeling the potential impacts of CO2 sequestration on shallow groundwater: Transport of organics and co-injected H2S by supercritical CO2 to shallow aquifers: International Journal of Greenhouse Gas Control, v. 14, p. 113–127, doi:10.1016/j.ijggc.2013.01.014.

Zhou, W., Wang, T., Yu, Y., Chen, D., and Zhu, B., 2016, Scenario analysis of CO2 emissions from China's civil aviation industry through 2030: Applied Energy, doi:10.1016/j.apenergy.2016.05.004.